ORGANIC BULK HETEROJUNCTION SOLAR CELLS WITH IMPROVED EFFICIENCY

YANFEI DING

Organic bulk heterojunction solar cells with improved efficiency

by

© Yanfei Ding

A thesis submitted in partial fulfillment of

the requirements for the degree of

Master of Science

Department of Physics and Physical Oceanography

Memorial University of Newfoundland

November, 2009

St. John's Newfoundland

Abstract

Organic solar cells have attracted considerable attention in recent years for their unique advantages, such as solution processing, flexibilities, and low cost for mass production. The highest power conversion efficiency reported so far is 6.5%. However, it is widely believed that the efficiency barrier of 10% has to be exceeded before polymer solar cells can be commercialized. Our study focuses on developing universal techniques for the improvement of the efficiency of organic solar cells and flexible polymer solar cells on two types of bulk heterojunction devices, i.e. poly(3-hexylthiophene) (P3HT) and [6,6]-phenyl-C61-butyric acid methyl ester (PCBM), and (poly[2-methoxy,5-(2-ethylhexoxy)-1,4-phenylene vinylene]) (MEH-PPV) and PCBM. The universal techniques we propose and demonstrate to achieve efficiency improvement include treatment of anode electrode by chemical and optical techniques, optimization of buffer layer, and device processing with additives. All reported organic solar cells of high efficiencies have been achieved under inert environment, among which some devices are either encapsulated devices or tandem devices. The polymer solar cells studied in this thesis are unencapsulated single cells tested at ambient environment. The efficiency of the P3HT:PCBM device with ITO substrate irradiated by UV light has been enhanced to 3.65%, as compared with the efficiency of 2.01% from the device fabricated on untreated ITO substrate. To improve the efficiency of organic solar cell, we reveal an approach to effectively adjust the properties of the buffer layer, Poly(ethylene-dioxythiopene):poly(styrenesulfonate) (PEDOT:PSS), achieving an improvement in the efficiency from 2.08% to 2.92%.

The properties of MEH-PPV:PCBM devices processed with either of the two additives, dimethyl sulfoxide (DMSO) or 1,8-octanedithiol (ODT) demonstrate significant increases in the efficiency, i.e., from 2.5% to 2.8% after doped 2 vol% of ODT, and from 2.5% to 3.15% by doping 5 vol% of DMSO, surpassing the highest efficiency of MEH-PPV:PCBM solar cells reported so far.

We demonstrate the operation of flexible solar cells, which are fabricated on polyethylene terephthalate (PET) substrates. Size effect on the performance of flexible solar cells indicates that the efficiency of the solar cell increase in the device size. The relationship between the efficiency and the bending angle of the flexible solar cells as well as the mechanisms of the degradation in efficiency are evaluated for the finite time. .

List of Abbreviations

Abbreviations or symbols	Full description
AM	Air mass
BHJ	Bulk heterojunction
CB	Chlorobenzene
CuPc	Copper phthalocyanine
CV	Cyclic voltammetry
D/A	Donor/Acceptor
DCB	Dichlorobenzene
DIM	Di-iodomethane
DMSO	Dimethyl sulfoxide
EBL	Exciton blocking layer
EQE	External quantum efficiency
FF	Fill factor
HOMO	Highest occupied molecular orbital
ITO	Indium tin oxide
FTO	Fluorine tin oxide
LUMO	Lowest unoccupied molecular orbital
MDMO-PPV	poly[2-methoxy-5-(3',7'-dimethyloctyloxy)-1,4-phenylenevinylene
MEH-PPV	Poly[2-methoxy, 5-(2'ethy-hexyloxy)-p-phenylenevinylene]
NP	Nanoparticles
OC_1C_{10}-PPV	Poly[2-methoxy-5-(3',7'-dimethyloctyloxy)-p-phenylenevinylene]
ODT	1,8-octanedithiol

P3HT	Poly(3-hexylthiophene)
P3OT	Poly(3-octylthiophene)
PCBM	Phenyl C_{61}-butyric acid methylester
$PC_{71}BM$	Phenyl C_{71}-butyric acid methylester
PCE	Power conversion efficiency
PCPDTBT	Poly[2,6-(4,4-bis-(2-ethyhexyl)-4H-cyclopenta[2,1-b;3,4-b']-dithiophene)-alt-4,7-(2,1,3-benzothiadiazole)]
PDDTT	Poly[5,7-bis(4-decanyl-2-thienyl)thieno[3,4-b]diathiazole-thiophene-2,5]
PDOCPDT	Poly[2,5-(7,7-dioctyl)-cyclopentadithiophene]
PEDOT:PSS	Poly(ethylene-dioxythiopene):poly(styrene sulfonate)
PTAA	Poly(triarylamine)
PV	Photovoltaic
SWNT	Single walled nanotubes
TMBZ	Trimethylbenzene
ZnPc	Zinc phthalocyanine
J_{sc}	Short circuit current density
I_{mpp}	Maximum power point current
I_o	Intensity of the incident light
I_t	Intensity of the light after passing through a film
k	Extinction coefficient
P_{in}	Incident light power density
V_{oc}	Open circuit voltage
V_{onset}	Voltage when the sample starts to reduction
V_{mpp}	Maximum power point voltage
α	Absorption coefficient
Ω/□	Ohm per square

Acknowledgements

I would like to thank my supervisors Dr. Qiying Chen and Dr. Ivan Saika-Voivod for my M.Sc. program. I thank Dr. Chen for all his patient guidance and encouragement throughout this project. I am fortunate to have worked with him to learn many things about experimental physics. I also thank to Dr. Saika-Voivod for his patience when writing program to me and pointing out which of my molecule system could be running. I would also like to thank Dr. Liqiu Men for SEM and Raman spectroscopic measurements and helpful discussions on experiments. I would also like to thank Dr. Maynard Clouter for permission to use his thermal deposition system and kindness rendered to me on experiments. I thank Dr. Yuming Zhao and Guang Chen for teaching me how to operate the cyclic voltammetry and supplying me with dichlorobenzene. Courtesy of ZnO samples from Dr. Kris Poduska's research group for possible application is in any solar cells is greatly appreciated. The assistance from Julie Collins on using the Cary spectrophotometer is also greatly appreciated.

Last but not least, I would like to thank my family for their continuous generous financial support.

Lists of Figures

Lists of Tables

Contents

harvests a specific fraction of sunlight and thus achieves a PCE value above 30% [4]. However, the manufacture of silicon photovoltaic (PV) cells (silicon and silicon-based components) requires millions of gallons of water and temperature as high as 300-500 ^{o}C during fabrication as well as a large amount of solvents including highly toxic ones. In contrast, organic photovoltaic materials show great promise in various low-cost, large-area applications. For instance, after applying the metal and organic multilayers as thin as 10 nanometers to a flexible plastic substrate at a cost approaching 1 cent per square centimeter (compared to a dollar or so to produce a square centimeter of silicon substrate), an organic photovoltaic cell could weight 100 times less than a cell of silicon substrate [5]. Compared with the inorganic counterparts, organic photovoltaic materials with the merits of flexibility, light weight, and low cost will lead to new markets for solar energy, potentially powering everything from watches and calculators to laptop computers. However, the highest PCE value of an organic photovoltaic cell reported so far is only 6.5% under the standard Air Mass (AM) 1.5G one Sun test condition (100 mW/cm^2) [6].

The photovoltaic effect is the fascinating phenomenon that generates direct electrical power measured in watts (W) or kilowatts (kW) from functional materials when they are illuminated by photons. This property is essential for solar cells to realize power conversion from light to electrical energy. Recently, organic photovoltaic materials have attracted significant attention. After Weiss *et al.* first reported high conductivity in iodine-doped oxidized polypyrrole in 1963 [7], much effort has been devoted to the electronic properties of semiconducting organic materials in the recent decades. H. Shirakawa, A. J. Heeger, and A, G, MacDiarmid received the Noble prize in Chemistry in 2000 for the discovery and development of conductive polymers [8]. Polymeric solar cells based on conjugated polymer/fullerene to form a donor/acceptor (D/A)

bulk heterojunction blend system was first reported in 1995 [9]. Previous work has worked on various D/A systems with examples such as (3-hexylthiophene) (P3HT), poly[2-methoxy, 5 ethyl(2' hexyloxy) paraphenylenevinylene] (MEH-PPV), and [6,6]-phenyl-C_{61}-butyric acid methyl ester (PCBM) [10,11,12,13,14,15]. Compared with other organic donor materials, P3HT possesses some unique characters, such as high degree of crystallinity, high hole mobility in regioregular state (10^{-4} to 10^{-2} cm^2/V s), extended absorption in the red spectra region (to 650 nm), and environmental stability [16]. As a donor material, MEH-PPV has similar properties to P3HT, for example, high hole mobility (10^{-5} cm^2/V s) [17], high absorption in the red spectrum region (to 500 nm), and good environmental stability. PCBM is a common acceptor material for photovoltaic cells. It possesses favourable characteristics, such as solubility and absorption profiles. The major difference in the functionalities of a donor and an acceptor is that the acceptor molecules stabilize free electrons. PCBM is a derivative of fullerene (C_{60}), which possesses a high electron affinity. However, since the solubility of C_{60} is low, it is necessary to improve its solubility, which can be realized by attaching a long chain on the C_{60} molecules to form a PCBM molecule. Both pure C_{60} and its simple derivatives absorb at wavelengths shorter than 400 nm [18], and in visible to infrared regions as well.

1.3 Device structures and operation principles

The early polymer solar cells consisted of a heterojunction bilayer, in which the donor and acceptor phases were deposited sequentially on the top of the other layer with a single common interface (Fig. 1.1a). Since the majority of the excitons were generated at a distance

more than L_{ex} away from the heterojunction interface, very low PCE values were achieved, where L_{ex} was the distance that an exciton can travel within its lifetime. This problem can be solved by using a bulk heterojunction (BHJ) with a planar-layered structure, where the organic light absorbing layer is sandwiched between the two different electrodes (Fig. 1.1b). In bilayered and BHJ solar cells, one of the electrodes must be transparent, for which an indium-tin-oxide (ITO) film is a common selection, though FTO (Fluorine tin oxide) can also be used. The other electrode is usually aluminum, while calcium, silver, gold or other metals may also be used.

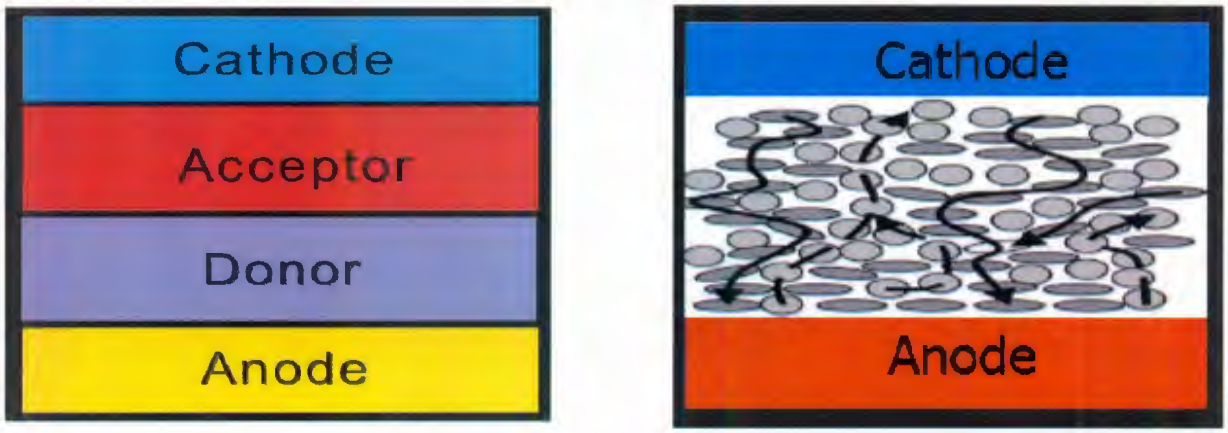

(a) (b)

Figure 1.1: Schematic illustration of an organic PV cell: (a), an organic bilayered solar cell; and (b), an organic bulk-heterojunction solar cell.

1.3.1 Bilayer PV cells

In bilayer PV cells, organic donor and acceptor materials contact together through two thin film layers. Each donor or acceptor material has a characteristic HOMO (highest occupied molecular orbital) and LUMO (lowest unoccupied molecular orbital) energies, with the HOMO

and LUMO of the donor being higher in energy than those of the acceptor, respectively. The gap between the HOMOs and LUMOs is referred to as the optical band gap (Fig. 1.2a). This determines the minimum wavelength of the light required for excitation in each material. Due to the fact that the optical band gap is smaller than the energy required to create a free electron hole pair, when photons hit either donor or acceptor materials to excite an electron from the HOMO to the LUMO, it will generate only a couple of electron-hole pairs called excitons, not free electron-hole pairs. In order to generate a free electron-hole pair, the exciton must travel to the interface between the donor and acceptor molecules. At the interface between these two layers, an electrical field results from the initial movement of electrons from the acceptor to donor, and the movement of holes in the reverse direction. This process quickly reaches equilibrium and forms a barrier to further charge transport. When light hits the cell, free electron-hole pairs are created, and migrate to the p-n interface where they separate due to the inherent electrical potential-energy difference in the cell. In this process, electrons, which have been excited to the LUMO of the donor molecule, can jump into the LUMO of the acceptor (Fig. 1.2b), driven by the LUMO level offset between the donor and the acceptor, or holes in the HOMO of an acceptor can jump into the HOMO of the donor (Fig. 1.2b), driven by the HOMO level offset between the donor and the acceptor, thus the exciton becomes a free electron and a free hole [19]. This dissociation can occur only if the difference in energy between the HOMOs or LUMOs is greater than the binding energy of the exciton. The separated free electrons and holes from the excitons then migrate to their respective electrodes; and an external current should be measured.

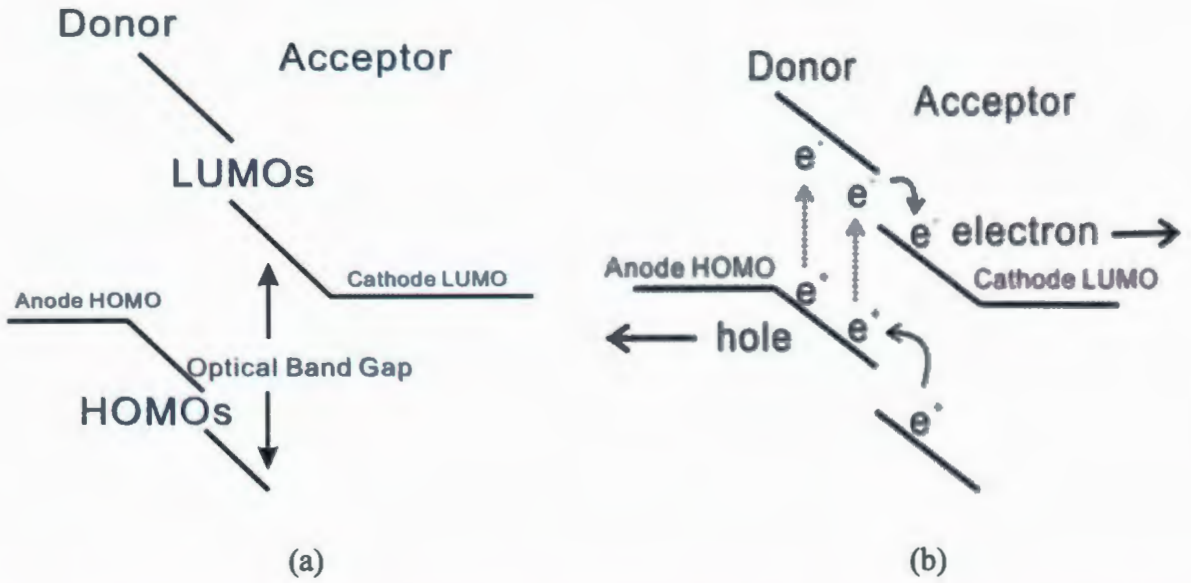

Figure 1.2: Schematic representation of (a) energy-band diagram and (b) migration of electrons and holes in the bilayer PV cells.

1.3.2 Bulk-heterojunction (BHJ) PV cells

The idea of a heterojunction is to prepare a junction by using two materials of different electron affinities and ionization potentials, in order to favour exciton dissociation. In this case, electrons will be accepted by the material with the larger electron affinity and holes by the material with the lower ionization potential. The simplest BHJ structure is a layer where an electron-accepting and an electron-donating material are blended together, sandwiched between two different conducting contacts, typically a material of high work function (e.g. ITO) and a metal of low work function (e.g. Al, Ca or Ag). The difference in the work function provides an electrical field that drives holes flow to the high work function metal (anode) and electrons to the low work function metal (cathode) from the blended organic layer. This electrical field allows for the differences in the potential energies that are larger than the exciton binding energy, to

break up the photon generated excitons. These excitons may be broken up to supply the electrons and holes. Furthermore, the blended layer thickness is usually similar to the exciton diffusion length, and then wherever an exciton is photogenerated in either metal, it can easily diffuse to an interface and break up. If continuous processes exist in each material from the interface to the respective electrodes, then the separated charge carriers may travel to the contacts (Fig. 1.2) and deliver current to the external circuit. This effect has been reported independently by several groups for a blend of two conjugated polymers [20,21,22].

Compared with the bilayer organic PV cell, the bulk-heterojunction overcomes the limitation of charge generation at a two-dimensional interface (bilayer) by distributing the acceptor more or less homogeneously into the donor matrix, thereby generating a three dimensional network of photoinduced charge interfaces. Recently, BHJ type PV cells composed of mixtures of conjugate polymer/fullerene derivatives have exhibited conversion efficiency as high as 6.1% under solar simulator [23].

1.3.3 Fullerene-Based solar cells

PCBM is the most widely utilized electron conducting acceptor type-polymers in organic solar cells due to its solubility. Important representatives of hole conducting donor-type semiconducting polymers on the other side are (i) derivatives of phenylene-vinylenes, for example, MEMO-PPV and MEH-PPV, (ii) derivatives of thiophene chains such as P3AT, P3OT, and P3HT, and (iii) derivatives of phthalocyanine, such as copper phthalocyanine (CuPc), zinc phthalocyanine (ZnPc), and magnesium phthalocyanine (MgPc).

a) PPV-PCBM solar cells

Shaheen *et al.* showed that a power efficiency of 2.5% under AM 1.5 conditions can be obtained by using chlorobenzene as a solvent for spin-casting in the weight ratio of 1:4 for MDMO-PPV:PCBM[24]. since PPV possesses a larger E_{HOMO} value, for example, E_{HOMO} of MEH-PPV is 5.3 eV, High V_{oc} is the characteristics of the PPV-PCBM solar cells, for example, 0.8 V V_{oc} can be obtained from MDMO-PPV:PCBM solar cells, and V_{oc} of MEH-PPV:PCBM solar cells is 0.85 V in this thesis (Chapter 4).

b) P3HT-PCBM solar cells

Thiophenes are conjugated polymers with good environmental stability, solubility and processability. Regioregular poly(3-alkylthiophenes)(P3AT), poly(3-hexylthiophene)(P3HT), and poly(3-octylthiophene) are used as electron donors in polymer:fullerene bulk heterojunction solar cells with record power conversion efficiencies up to 5%[12]. P3HT is the most widely used donor conducting donor type-polymers in thiophene:fullerene solar cells, using P3HT as donor and PCBM as acceptor, bulk heterojunction solar cells have been realized with power conversion efficiencies up to 5%[12,25]. The high efficiency of these devices is proposed to be due to a microcrystalline lamellar stacking in the solid state packing [26], and P3HT exhibits a hole mobility up to 0.1 $cm^2/V \cdot s$ [27,28].

c) CuPc-PCBM solar cells

Since 1986, Tang use a copper phthalocyanine (CuPc)/3,4,9,10-perylenetetra-carboxylic -bis-benzimidazole heterojunction to improve the power conversion efficiency from almost zero to 0.95%[29]. Phthalocyanine (Pc) have attracted great interest recently for the possibility to build a high PCE solar cell. The most common phthalocyanine used in organic solar cell are copper phthalocyanine[30,31], zinc phthalocyanine[32], tin (II) phthalocyanine[33], and even copper hexadecafluorophthalocyanine[34]. These studies have shown Pcs can be used to build a bilayer structure OSC by thermal evaporation. However, the PCE of the Pc solar cells is still low compared to poly(3-hexylthiophene) (P3HT):([6,6]-phenyl-C61 butyric acid methyl ester) PCBM bulk heterojunction solar cells. The reason for that is the bulk heterojunction concept has heavily increased (orders of magnitude) the interfacial area between the donor and acceptor phases compared to bilayer structure[35]. On the other hand, in a conjugated polymer blend, both components exhibit a high optical absorption coefficient and cover complementary parts of the solar spectrum[36]. Bilayer-structured solar cells are usually prepared by thermal evaporation while the bulk heterojunction can be achieved by the co-deposition of donor and acceptor pigments or solution casting of polymer/polymer, polymer/molecule, or molecule/molecule,

donor/acceptor blends[36]. The cost of thermal evaporation is high for industrial production, and the deposition process is complicated as compared with spin coating.

d) Tandem solar cells

Tandem solar cells, which is two solar cells with different absorption characteristics are linked in order to take advantage of a wider range of the solar spectrum, is the tendency of the development of the organic solar cell. Using P3HT:$PC_{70}BM$ as the front cell and PCPDTBT:PCBM as the back cell, tandem solar cells have been realized with open circuit voltage up to 1.24 V and power conversion efficiency up to 6%[6]. The high efficiency of this device is proposed to be due to the wide solar spectrum and two open circuit voltage of the front cell and back cell in series, for example, open circuit voltages of P3HT:$PC_{70}BM$ and PCPDTBT:PCBM solar cells are 0.63 and 0.66 V, respectively.

1.4 Characterization of organic solar cells

1.4.1 Solar radiation

The Air Mass is a measure of the extent of the absorption in the atmosphere which affects the spectral content and intensity of the solar radiation reaching the earth's surface. A widely used standard for comparing solar cell performance is the AM 1.5 spectrum normalized to a total power density of 1 kW/m^2 (100 mW/cm^2). Figure 1.3 shows the solar energy distribution at AM 1.5 as a function of wavelength, in which the peak energy occurs at ~580 nm. In order to increase

the absorption of solar energy, the peak absorbance of the film used in the polymer solar cell should occur around 580 nm.

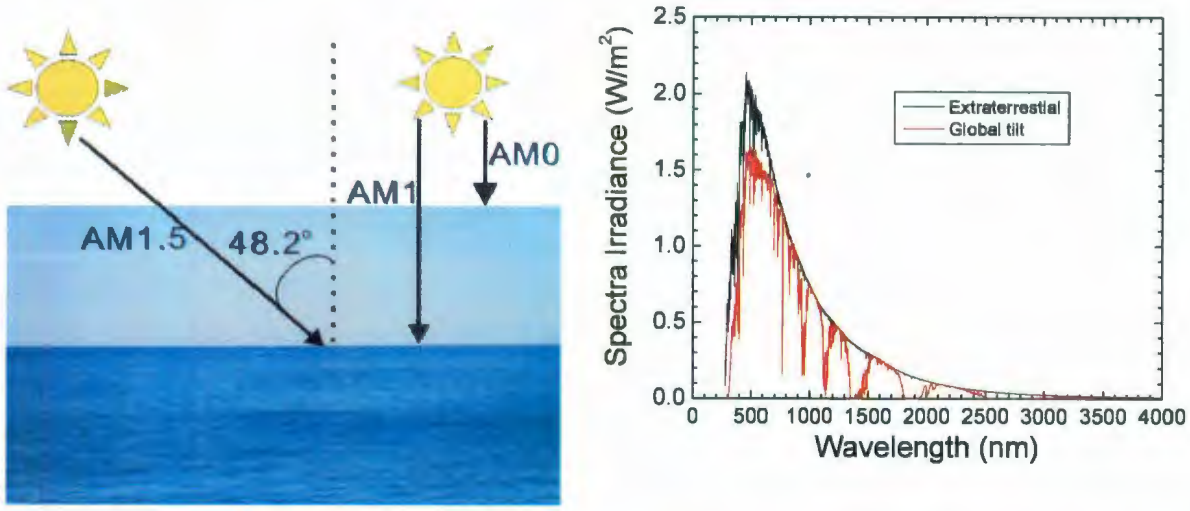

Figure 1.3: Schematic illustration of different Air Mass (AM) solar irradiation spectra as received on earth and spectral irradiance for AM 1.5G reference spectrum (Global tilt).

1.4.2 Electrical properties of PV cells

The performance of a PV cell is measured under the standard irradiation condition. The standard reporting conditions for rating organic solar cells are: 1000 Wm^{-2} (100 mW/cm^2) irradiance, AM (air mass) 1.5 globe reference spectrum, and 25°C cell temperature. The power conversion efficiency (PCE) of a PV cell is the power output divided by the incident light power, which equals to:

$$\eta = \frac{V_{oc} \times I_{sc} \times FF}{P_{in}} \tag{1.1}$$

Each term in the Eqn. (1.1) is explained in the following paragraphs: open circuit voltage (V_{oc}) is the potential difference between the work functions of the two metal contacts [36]. However, in a

p-n junction, the maximal available voltage is determined by the difference of the quasi Fermi levels of the two charge carriers, that is, *n*-doped semiconductor energy level and *p*-doped semiconductor energy level, respectively. In organic solar cells, V_{oc} is found to be linearly dependent on the HOMO level of the electron donor and the LUMO level of the electron acceptor [37,38].

I_{sc} is the short circuit current, which is determined by the product of the photoinduced charge carrier density and the charge carrier mobility within the organic semiconductors:

$$I_{sc} = ne\mu E \tag{1.2}$$

where n is the density of the charge carriers, e is the elementary charge, μ is the mobility, and E is the electric field [36].

P_{in} is the incident light power density, which is identified at 1000 W/m^2 with a spectral intensity distribution matching that of the sun on the earth's surface at an incident angle of 48.2°, called the AM 1.5 spectrum [39]. It should be pointed out that mobility is not a material parameter but a device parameter; it is also sensitive to the nanoscale morphology of the organic semiconductor films[40,41,42]. Mobility can also be defined as:

$$\mu = \frac{|V_H|}{R_s IB} \tag{1.3}$$

where V_H is the Hall voltage, R_s is the sheet resistance, I is the current, and B is the magnetic field, and R_s is determined by the following formula:

$$R_s = \frac{\rho}{t} \tag{1.4}$$

where t is the thickness of the film, ρ is the sheet resistivity, which is equal to the inverse of the conductivity, i.e.

$$\rho = \frac{1}{\sigma} \tag{1.5}$$

where σ is the conductivity.

Fill factor (FF) is defined as the ratio of the maximum power divided by the short circuit current and the open circuit voltage in the current density-voltage (*J-V*) characteristics of the solar cell:

$$FF = \frac{I_{mpp} \times V_{mpp}}{I_{sc} \times V_{oc}} \tag{1.6}$$

where I_{mpp} and V_{mpp} are the current and voltage at the maximum power point (maximum area of *J-V* curve as indicated in Fig. 1.4, respectively.

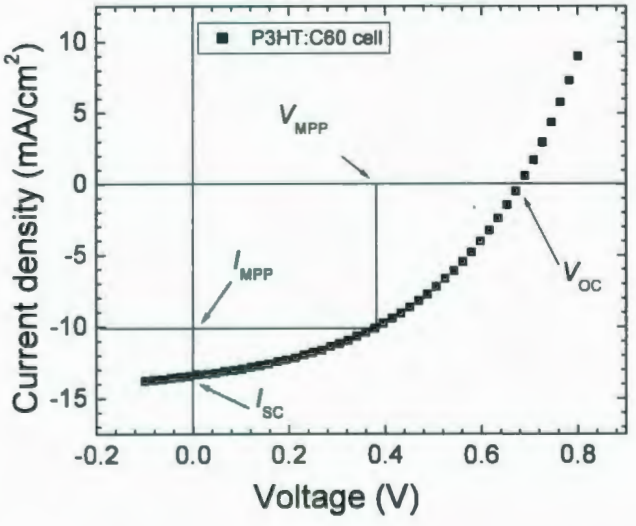

Figure 1.4: Current-voltage (*J-V*) curve of an organic solar cell.

In view of the role that each term plays in Eqn. (1.1), it is obvious that large values of the three parameters (I_{sc}, V_{oc}, and FF) generate a higher PCE value.

1.4.3 Optical properties of PV cells

Optical properties of PV cells include absorption coefficient and refractive index. Absorption coefficient α is a material property which defines the extent to which a material absorbs light energy,

$$\alpha = \frac{-\ln(\frac{I_o}{I_t})}{t} \tag{1.4}$$

where I_o is the intensity of the incident light, I_t is the intensity of the light after passing through the film, and t is the thickness of the film. The extinction coefficient k for a particular substance is a measure of the amount of absorption loss when the electromagnetic wave propagates through the material. Equation (1.5) shows the dependence of the absorption coefficient on the extinction coefficient and wavelength.

$$\alpha = \frac{4\pi k}{\lambda} \tag{1.5}$$

where λ is the wavelength in vacuum. The parameter used to describe the interaction of electromagnetic radiation with matter is the complex index of refraction, N, which consists of a real part (n) and an imaginary part (extinction coefficient k).

$$N = n - ik \tag{1.6}$$

where, n is the refractive index indicating the phase velocity ($n = c/v$), and k represents the damping of an electromagnetic wave inside the film. Both of n and k can be determined by ellipsometry.

1.5 Material selection

For a bulk-heterojunction photovoltaic cell, the active blend layer consists of an acceptor and a donor. It has been recognized that the most efficient exciton dissociation in organic materials occurs at the D/A interface. At this interface, the donor molecules must satisfy several conditions in order to function efficiently: (1) absorption of visible or IR light is important for the conversion of photons into excitons; (2) donor molecules must have the space which allows the movement of the exciton to a donor-acceptor interface; (3) donor molecules must have energy differences in HOMO to acceptor's HOMO and LUMO to acceptor's LUMO which allow for exciton dissociation; (4) once exciton dissociates, the hole should be transferred to the anode [5]. Organic donor materials (Fig. 1.5) reported so far include PCPDTBT [43,6], pentacene [44], MEH-PPV [14,15], phthalocyanine [45,46,47], and P3HT [10,11,13]. On the other hand, in order to function efficiently, an acceptor is required to possess: (1) photon absorption property; (2) allowable space for the exciton movement; and (3) proper HOMO and LUMO difference. In addition to the three factors just mentioned, acceptor molecules are also expected to stabilize free electrons. PCBM is an acceptor material which has a high electron affinity. Reported acceptor materials used in the organic PV cells include PTCBI and F8BT. There are many combinations from these materials. Performance of some reported organic PV cells is reviewed in Table 1.1. PCDTBT-PCBM PV cell shows a high efficiency, due to the use of the polymer absorbing over a wide range of the solar spectrum. It can be found from Table 1.1 that P3HT-PCBM PV cells possess relatively high PCE values. The data from Table 1.1 also indicate that $PC_{71}BM$ gives comparable or better performance as compared with the PCBM in fullerene - P3HT PV cells. The highest PCE reported so far is 6.5% by A. J. Heeger and

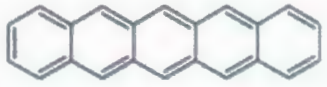

Pentacene

Phthalocyanine

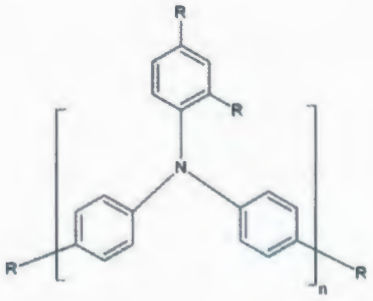

PTAA

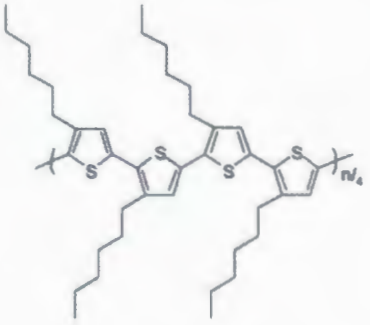

P3HT

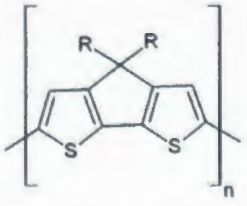

PDOCPDT

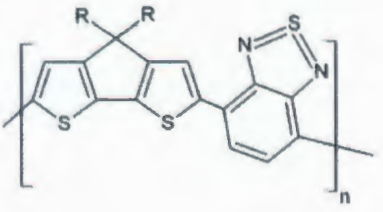

PCPDTBT

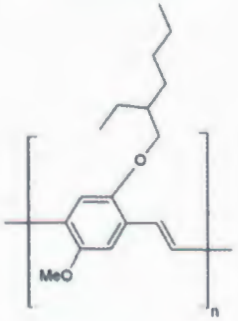

MEH-PPV

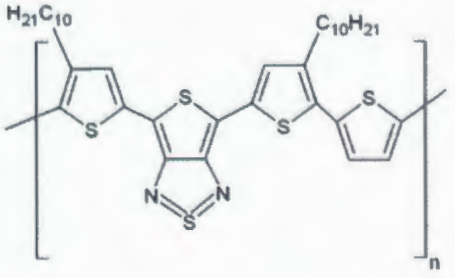

PDDTT

Figure 1.5: Molecular structures of selected semiconducting polymers used in PV cells

his coworkers[6]. A new structure, tandem cell architecture, is used in their cells to achieve this high efficiency. The principle of tandem cell architecture is two solar cells in series, with different absorption characteristics to cover a wider range of the solar spectrum, are fabricated with each layer processed from solution with the use of bulk heterojunction materials comprising semiconducting polymers and fullerene derivatives. The device structure of the polymer tandem solar cell is Glass/ITO/PEDOT/PCPDTBT:PCBM/TiO_x/PEDOT/ P3HT:$PC_{71}BM$/TiO_x/Al. The highest PCE of the single BHJ PV cell reported to date is from $PC_{70}BM$-PCDTBT by A.J. Heeger's group [23]. The high PCE is attributed to a combination of the use of a polymer which absorbs over a wide range of the solar spectrum and 1,8-alkanediothiol additive that improves the morphology of these films.

It can be found from Table 1. 1 that P3HT-PCBM PV cells generally reaches high PCE values. The highest PCE reported for these PV devices to date is 5.0%. Molecular structures of selected polymers used in PV cells are shown in Fig. 1.5. These materials are *p*-type, hole conducting material that works as electron donor. It is obvious from Table 1.1 that MEH-PPV possesses a larger E_{HOMO} value and P3HT has a relatively higher mobility (Table 1.2). Therefore, P3HT and MEH-PPV are selected as the donors of the PV cells in this study. Among these D/A systems (Table. 1.1), P3HT:PCBM shows a high PCE, i.e, 4.4-5.0%, due to some unique properties of P3HT and MEH-PPV over other polymers [17,48]. Figure 1.5 shows the molecular structures of MEH-PPV and P3HT. It is found that both of them have long alkyl chains, to render P3HT and MEH-PPV high solubility in most common solvents, including chloroform, chlorobenzene, and dichlorobenzene.

Table 1.1: Performance of reported organic solar cells with their full names given in the list of abbreviations.

Donor	Acceptor	Solvent	Thickness (nm)	P (mW/cm^2)	PCE (%)	Ref.
PCDTBT	$PC_{71}BM$	DCB		100	6.1	[23]
PCPDTBT	$PC_{71}BM$	CB	110	100	5.5	[43]
P3HT	PCBM	CB	100	90	5.0	[25]
P3HT	PCBM	CB		80	4.9	[12]
P3HT	PCBM	DCB	220	100	4.4	[10]
P3HT	PCBM	CB	175	85	4.4	[11]
P3HT	$PC_{71}BM$	CB	100	85	4.1	[49]
P3HT	PCBM	CB	100	85	3.8	[49]
P3HT	PCBM	DCB	225	100	3.7	[50]
P3HT	PCBM	DCB	200	100	3.6	[50]
CuPc	PCBM			150	3.6	[51]
P3HT	PCBM	DCB	290	100	3.5	[50]
P3HT	PCBM	DCB	250	100	3.5	[50]
P3HT	PCBM	DCB	330	100	3.5	[50]
P3HT	PCBM	$CHCl_3$	150	100	3.4	[52]
PCPDTBT	$PC_{71}BM$	DCB	200	100	3.2	[53]
P3HT	PCBM	Xylene	100	100	3.0	[54]
MEH-PPV	PCBM			20	2.9	[9]
MDMOPPV	PCBM				2.5	[24]
P3HT	PCBM	DCB	200	85	2.4	[11]
P3HT	PCBM	DCB	140	100	2.1	[50]
ZnPc	PCBM			100	1.9	[55]
P3HT	PCBM	CB	200	85	1.8	[11]
P3HT	PCBM	DCB	72	100	1.8	[50]
P3HT	PCBM			96	1.7	[56]
P3HT	PCBM	TMBZ	125	100	1.5	[57]
MEH-PPV	PCBM	DCB	170	130	1.5	[15]
CuPc	PTCBI			100	1.4	[47]
P3OT	PCBM	TMBZ	125	100	1.1	[57]
PEBT	PCBM	CB	90	100	1.1	[58]
PTV	PCBM	CB		100	0.6	[59]
P3HT	PCBM	Xylene	100	100	0.25	[54]
P3OT	SWNT	$CHCl_3$	100	100	0.22	[60]

Table 1.2. Comparison of PV cells with different semiconducting polymers [27].

Polymer	E_{LUMO} (eV)	E_{HOMO} (eV)	E_g (eV)	Hole mobility (cm^2/Vs)
PTAA	-2.00	-5.00	3.00	10^{-4} -10^{-3}
MEH-PPV	-2.90	-5.30	2.40	10^{-4} -10^{-3}
P3HT	-3.00	-5.10	2.10	10^{-4} -10^{-1}
PTV	-3.10	-4.90	1.80	10^{-5} -10^{-3}
PDOCPDT	-3.35	-5.15	1.80	10^{-4} -10^{-3}
PCPDTBT	-3.57	-5.30	1.73	10^{-2}
PBTTT	-3.60	-5.10	1.50	0.2-0.6
PDDTT	-3.60	-4.70	1.10	

Table.1.1 shows that PCBM is a common material which has been used as an acceptor in photovoltaic cells. C_{60} and its derivatives show an *n*-type, electron conducting behavior and serve as electron-acceptor material. With the molecular structure in Fig. 1.6a, C_{60} has a high electron affinity, with an efficient capture of the free electrons. However, the solubility of pristine C_{60} is quite low. As a soluble C_{60} derivative, PCBM was first synthesized by Wuld *et al.* [61] and has been widely used in polymer/fullerene solar cells with the molecular structure illustrated in Fig.1.6.

There are some constraints limiting the efficiency of a conjugated polymer-based PV device, which include short exciton diffusion length (exciton generation), low mobility of the charge carriers (carrier collection), and photon collection (light absorption). It has been reported that exciton generation and carrier collection has close relationships with the morphology of the film [62]. Increasing the roughness of the morphology of the film will result in an increased contact area between the polymer film and the metal cathode [16]. Therefore, when the exciton diffusion length is increased, more exciton will be generated. Due to the fact that a rough surface

of the film improves the film crystallinity, the hole mobility in the film will also be increased as the film surface increases.

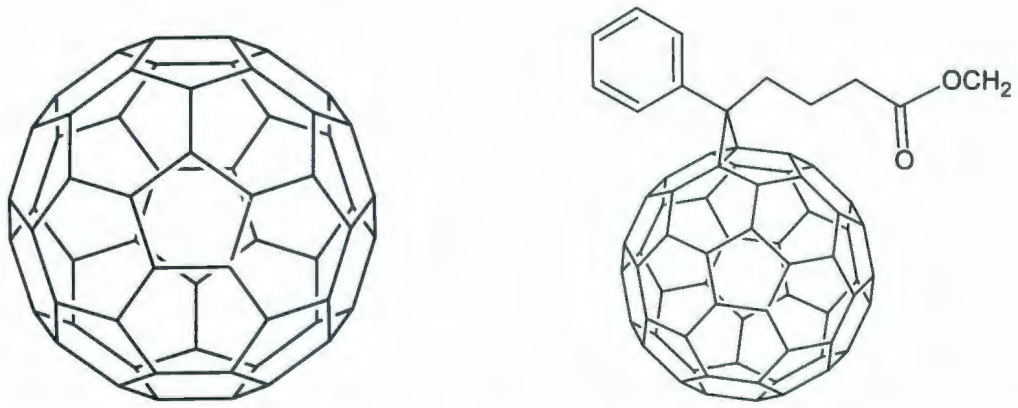

Figure 1.6: Molecular structures of (left) C_{60} and (right) [6, 6]-phenyl C_{61} butyric acid methyl ester (PCBM).

To achieve an efficient photo-induced charge transfer, it is very important to understand the following aspects: (1) Selection of the solvent is very important for obtaining good morphology of the films as well as the efficiency and stability of the PV devices. These solvents may include xylene, toluene, chloroform, chlorobenzene and 1, 2-dichlorobenzene. (2) The morphology of the films should be sufficiently good, which should be free from pinholes, kinks, and overlapping of chains. The composition of donor/acceptor thus plays an important role to achieve good device performance. If the concentration of the acceptor is too high, the films will have kinks, overlapping chains, and the photo-induced charge transfer rate will be low[62]. On the other hand, if the concentration of an acceptor is too low, the interface of the organic layer and the electrode will become smooth, and the exciton will not have enough space to diffuse, resulting in a low exciton generation efficiency [62]. (3) Thermal annealing was found to be a possible approach to enhance the photon absorbance, improve the short circuit current, fill factor,

and therefore the efficiency of the device. To achieve a higher efficiency, the optimal annealing conditions of P3HT/PCBM and MEH-PPV/PCBM films must be determined. My previous research work studied these aspects in order to discover optimal parameters for sample preparation as well as optical constants of thin films for multilayer design and performance improvement [63]. The optimal solvent, composition ratio, and thermal annealing conditions have been discovered through the characterization of the optical properties of thin films, aided by the morphology observation with atomic force microscopy (AFM). The refractive index of the film blended with two materials is a complex number, with a real part and an imaginary part (extinction coefficient, k), which can be determined by an ellipsometry. The absorption coefficient can be derived from the relationship between the absorption coefficient and the extinction coefficient.

1.6 Outline

The majority of research on device fabrication and characterization of organic solar cells has been carried out in vacuum or inert atmosphere in order to prevent the rapid degradation of the films and device. Efficiency and stability of the devices are two major limitations to be overcome before organic solar cells find practical applications. In this study, we aim at developing universal techniques to improve the efficiency of organic solar cells. Except vacuum deposition of aluminum film as the cathode, all other steps of device fabrication and characterization have been carried out in ambient environment.

Our research here starts from the preliminary study reported in my Honour thesis [63]. In Chapter 2, we study efficiency improvement in OSCs by using a modified ITO anode, in which the influence of chemical and UV treatments of ITO on the performance of organic solar cell is investigated. A high conductivity approach for efficiency improvement is discussed in Chapter 3, aided by experiments with atomic force microscopy (AFM), and spectrophotometer. The optical calculation verifies the effectiveness of this approach, indicating that light harvested in the active layer is improved in this approach. Therefore, the efficiency of OSCs based on this approach is improved. In Chapter 4, the properties of devices processed with either of two additives, dimethyl sulfoxide (DMSO) or 1,8-octanedithiol (ODT), are studied by AFM, scanning electron microscopy (SEM) and spectrophotometer. After doping with a small amount of ODT or DMSO, efficiencies of the devices are significantly enhanced. Moreover, the efficiency achieved by processing with DMSO is the highest efficiency reported so far for the MEH-PPV:PCBM solar cells. We demonstrate successful operation of flexible solar cells in Chapter 5. In addition, we reveal the relationship between the efficiency and the bended OSC. SEM studies show that the bended PH510 film (anode) and the aluminum film have a rough, cracked, and inconsistent morphology. The degradation in the performance of OSC as a function of bending angle is experimentally measured.

Chapter 2

Surface treatments of indium-tin-oxide substrates for efficiency improvement

Abstract

In this chapter, the influence of different surface treatments of indium tin oxide (ITO) on the performance of organic solar cells is investigated, which includes chemical treatments by processing ITO substrates in either HCl or NaOH solutions, ultraviolet (UV) ozone treatments with two UV light sources of different emission spectra and intensities referred as UV1 and UV2 herein, and different combinations of these methods. Heterojunction solar cells

(ITO/PEDOT:PSS/P3HT:PCBM/Al) with different ITO treatments have been tested. After characterizing the changes in the surface properties of ITO anode with techniques such as Hall measurement, Seebeck coefficient measurements, absorption spectroscopy, surface sheet resistance measurement, atomic force microscope (AFM), and cyclic voltammetry, it has been found that the surface treatments change the properties of the ITO thin film (sheet resistance, carrier concentration, surface roughness, transmittance, work function and contact angle). As a consequence, the device performance has been significantly altered. The PCE of the device at AM 1.5 with ITO treatment by higher intensity UV2 light illumination exhibits a pronounced increase to 3.65%, as compared with 2.01% from the untreated ITO substrate.

2.1 Introduction

Organic solar cells have been the focus of research in terms of efficiency and stability for their advantages of low cost and great potential in the photovoltaic market [9,12,10]. Due to the high transmittance in the visible region, relatively low sheet resistivity and suitable work function, indium tin oxide (ITO)-coated glass substrates are commonly used as the anode in the organic solar cells [11,30,64]. The efficiency of organic solar cells with as-deposited ITO, however, is limited by many factors, such as short circuit, unstable *J-V* characteristics and low fill factor (FF). To mitigate these problems, various surface treatments using chemical solvent [65,66,67,68], UV ozone [30,64,69,70], and gas plasma [71,72] have been studied to optimize ITO properties, mostly in the study of organic light emitting diodes (OLEDs) with a few reports on organic solar cells [30,73]. Properties of the ITO films, for example, surface morphology and

sheet resistivity, are closely related with the performance of the organic solar cells. The effects of several surface treatments on the ITO parameters such as work function, surface roughness, sheet resistance, and carrier mobility have been extensively studied in the applications of OLEDs [64,69,70,71,72]. Kim *et al.* studied the effect of the oxygen plasma, aquaregia, and combinations of these two treatments on ITO surface properties, in which the best OLED performance was obtained with oxygen plasma treatment [64,65,66,68,67]. On the other hand, Nuesch *et al.* [74,75,76,77] also studied the chemical surface treatments and plasma treatments, and found that the OLED device with ITO acid treatment possesses a higher efficiency compared with the plasma treatment alone or its combination with acid treatment. It was also demonstrated that the optimal ITO surface treatment condition depends on the initial properties of ITO, material used, deposition method and annealing condition [65,78]. Djurišić *et al.* have performed a comprehensive study on the performance of copper phthalocyanine (CuPc)/C_{60} solar cells with ITO surface treatments (acid treatment with HCl solution, UV ozone treatment, mechanical treatment, and their combinations) [30]. The lowest sheet resistance in their work was obtained with UV ozone treatment as determined by Hall measurements, whereas the mechanical treatment followed by UV ozone and HCl solution gave the lowest resistance from four point probe (4pp) technique. UV ozone followed by HCl solution treatment resulted in the highest surface roughness. On the other hand, the largest value of the Seebeck coefficient was obtained from the untreated ITO while surface treatment slightly decreased the Seebeck coefficient. After characterizing ITO substrates with different surface treatments, it was found that the relationship between the ITO parameters and the performance of the solar cells was very complicated. It was observed that the HCl treatment, whether alone or in combination with UV ozone, increased the

short circuit current. UV ozone treatment alone also increased the short circuit current for a small amount, while the open circuit voltage was increased. The conclusion drawn by Djurišić *et al.* also indicated that the PCE of the CuPc/C60 cell (~0.1%) with the optimal surface treatment (mechanical + UV + HCl) was one order of magnitude larger than the PCE of the solar cell fabricated on an untreated ITO substrate (~0.01%), However, recent research has been mostly focused on the blends of regioregular poly(3-hexylthiophene) (P3HT) and a soluble fullerene derivative ([6,6]-phenyl C_{61}-butyric acid methyl ester, PCBM), the material combination that has led to high PCE values until now (4 % - 5 %) [10,13]. In this chapter, the relationship between the ITO surface properties and the performance of the organic solar cell will be investigated to address the fact that different approaches for ITO treatment are required for different photovoltaic active materials and different initial properties of ITO films. In order to understand the influence of ITO surface treatment on the performance of P3HT:PCBM solar cells and to identify optimal parameters for ITO surface treatment, a series of ITO surface treatments have been performed in this study to optimize the efficiency of the P3HT:PCBM solar cells, including hydrochloric acid (HCl) treatment, sodium hydroxide (NaOH) treatment, low-intensity UV ozone treatment (UV1), high-intensity UV treatment (UV2), and different combinations of these approaches. The properties of the ITO films with different treatments will be characterized by sheet resistivity, surface roughness, Seebeck coefficient and AFM morphology.

2.2 Experimental details

2.2.1 Device fabrication

(a) Treatment of ITO surface

Seven different approaches for ITO treatment have been used to modify the surface of ITO substrates, before spin-coating the PEDOT:PSS and the polymer films. These approaches are:

(1) Ultrasonic cleaning: The ITO substrate is successively washed in an ultrasonic bath of acetone and alcohol for 15 min each, then rinsed in deionized (DI) water for 1 min, and dried on a hot plate at ~50°C for 20 min.

(2) Acid treatment: Acid treatment is performed by dipping the substrate into a 10% aqueous acid solution for 10 min at room temperature first followed by ultrasonic cleaning (1). The acid solution used in this study is HCl, which was reported to achieve the best results for OLEDs [79].

(3) Sodium hydroxide (NaOH) solution treatment: The substrate is dipped in a 7% NaOH solution at room temperature for 10 min, followed by ultrasonic cleaning (1).

(4) UV1 ozone: UV ozone treatment is carried out with the irradiation of an ITO substrate by an UV lamp (UVS54, Mineralight) at a distance of 5 cm between the lamp and the sample for 30 min [69], the intensity of the UV light is ~1 mW/cm^2 measured by the power meter, and then followed by the ultrasonic cleaning (1).

(5) UV2 ozone: UV2 ozone treatment is performed with a 75 W UV light source for 15 min, with a distance of 5 cm between the lamp and the sample and an intensity of ~23 mW/cm^2 followed by the ultrasonic cleaning (1).

(6) HCl + UV: HCl treatment is carried out first on the ITO substrate followed by the UV1 and cleaning.

(7) HCl + UV2: HCl treatment is performed first on the ITO substrate followed by the UV2 and cleaning

The ITO coated glass substrates with surface sheet resistance of 10 ± 5 Ω/square (CB-50IN-0111) have been purchased from Delta Technologies, Ltd. All ITO substrates are first etched by ~20% HCl solution for ~30 min to the designed pattern followed by rinsing in DI water and dried on the hot plate at ~50°C for 20 min. Then, the ITO substrates will be treated in different ways.

(b) Fabrication of organic solar cells

For the organic solar cells fabricated using P3HT as the electron donor and PCBM as the electron acceptor, each device has an active area of ~12 mm^2 with a structure of ITO/PEDOT:PSS/P3HT:PCBM/Al. Regioregular P3HT and PCBM have been purchased from American Dye Source Inc. and Nano-C Inc., respectively, and used as received. A PEDOT:PSS layer between the ITO and the active layer is adopted in the device to improve the hole collection, and an Al electrode is used for electron collection. Organic solar cells have been fabricated according to the following steps: The treated ITO substrate is first ultrasonicated sequentially in acetone, alcohol and DI water for 15 min each, and then dried on a hot plate at ~50 °C for 20 min. PEDOT:PSS (Clevios P VP Al 4083) aqueous solution is filtered by a 0.45 μm filter, followed by spin-cast at 4000 r.p.m. for 120 s. The substrate is then dried on the hot plate for 10 min at 70 °C. The device with the best performance has been observed when the mixed solution had a P3HT:PCBM ratio of 1:0.8, i.e., with a concentration of P3HT (10 mg/ml) and PCBM (8 mg/ml)

in 1,2-dichlorobenzene [13]. A blended solution with a P3HT:PCBM ratio of 1:0.8 is stirred at 40°C for 24 h. After that, the 1,2-dichlorobenzene solution comprising P3HT (10 mg/ml) and PCBM (8 mg/ml) is spun cast at 700 r.p.m. for 40 s on the top of the PEDOT:PSS layer. Finally, an Al film is thermally deposited on the top of the active layer as a cathode. The device is then thermally annealed at ~150°C for 30 min and cooled to the room temperature inside a petri dish before the measurements. The complete structure of a P3HT:PCBM solar cell is shown in Fig. 2.1. The characterization of the PCE of the PV cell has been described in the previous chapter.

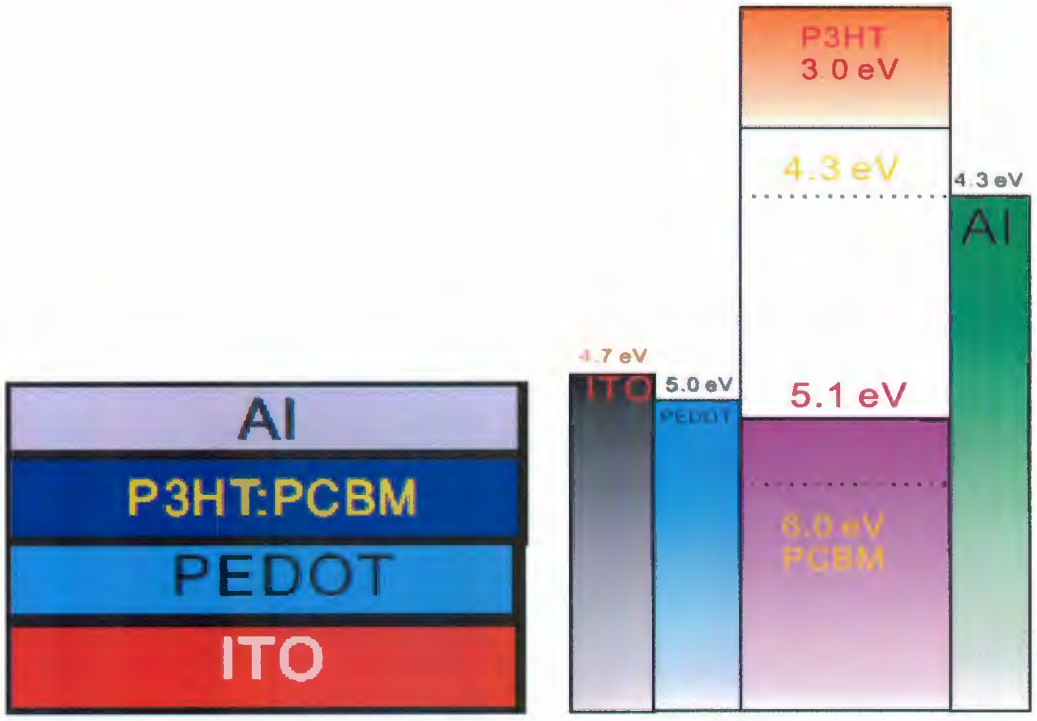

Figure 2.1: Schematic illustration and energy level diagram of a bulk heterojunction P3HT:PCBM solar cell.

2.2.2 ITO characterization and device measurement

Surface sheet resistance is determined from four point probe measurement (Fig. 2.2). The four point probe (4pp) setup used in our experiment consists of four equally spaced piano wire tips with a small radius (~125 μm) and each tip is flexible in order to minimize sample damage during probing. A high impedance current source is used to supply current through the outer two probes while a voltmeter measures the voltage cross the inner two probes to determine the sample resistivity. Typical probe spacing (s ~1 mm) is adopted [80]. For a very thin layer (t << s), the sheet resistivity can be expressed as [80]:

$$R_s = 4.53(\frac{V}{I}) \tag{2.1}$$

In our study, Keithley 2420 source meter is used to provide the impedance current as well as to measure the inner probe voltage simultaneously.

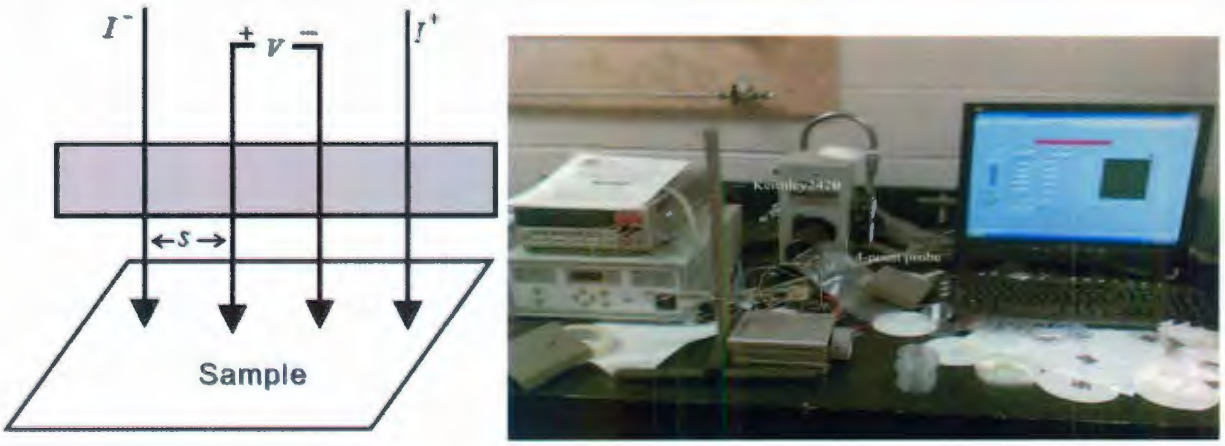

Figure 2.2: Schematic illustration of 4-point probe measurement.

Seebeck coefficient measurement is performed using a home-built setup consisting of a digitally controlled hot plate (TP294, Sigma Systems) and a metal plate. Since the specific heat capacity of glass is large, it is possible to generate a temperature difference (~8 °C) between the

two sides of an ITO substrate. The procedures for the measurement are to heat the metal plate to a temperature T_1 first, set the temperature of the hot plate to be $T_1 + 8$, put one side of ITO on the hot plate and the other side on the metal plate, then use Keithley 2420 to measure the voltage between these two sides. The spacing between the two electrodes is 2 cm. The Seebeck coefficient can be expressed as [81]

$$S(T) = \lim_{\Delta T \to 0} \frac{V_S(T, \Delta T)}{\Delta T} = \frac{k}{e}\left(\frac{\Delta E}{kT} + A\right) \tag{2.2}$$

where k is the Boltzmann constant, T is the temperature in Kelvin, ΔE is the energy difference between the top of the valence band and the Fermi level. The parameter A can be considered as a constant of the organic material. In a degenerate semiconductor, Seebeck coefficient is defined as [82]

$$S = \frac{\pi^2}{3}\frac{k}{e}\left(\frac{r + 3/2}{\eta^*}\right) \tag{2.3}$$

where r is the scattering parameter, and η^* is the reduced Fermi energy, i.e. E_F/kT,

After characterizing ITO substrates with different surface treatments, bulk hetero-junction solar cells are fabricated and their *J-V* curves are measured with a Keithley 2420 SourceMeter under simulated AM 1.5G irradiation (100 mW cm^{-2}) from a xenon-lamp-based solar simulator (Newport Oriel 96000 150W solar simulator) with filters.

2.3 Results and discussion

Figure 2.3 shows the AFM images of pristine ITO substrate and ITO substrates after separate treatment with NaOH solution, or UV light irradiation (UV1 or UV2), or HCl solution,

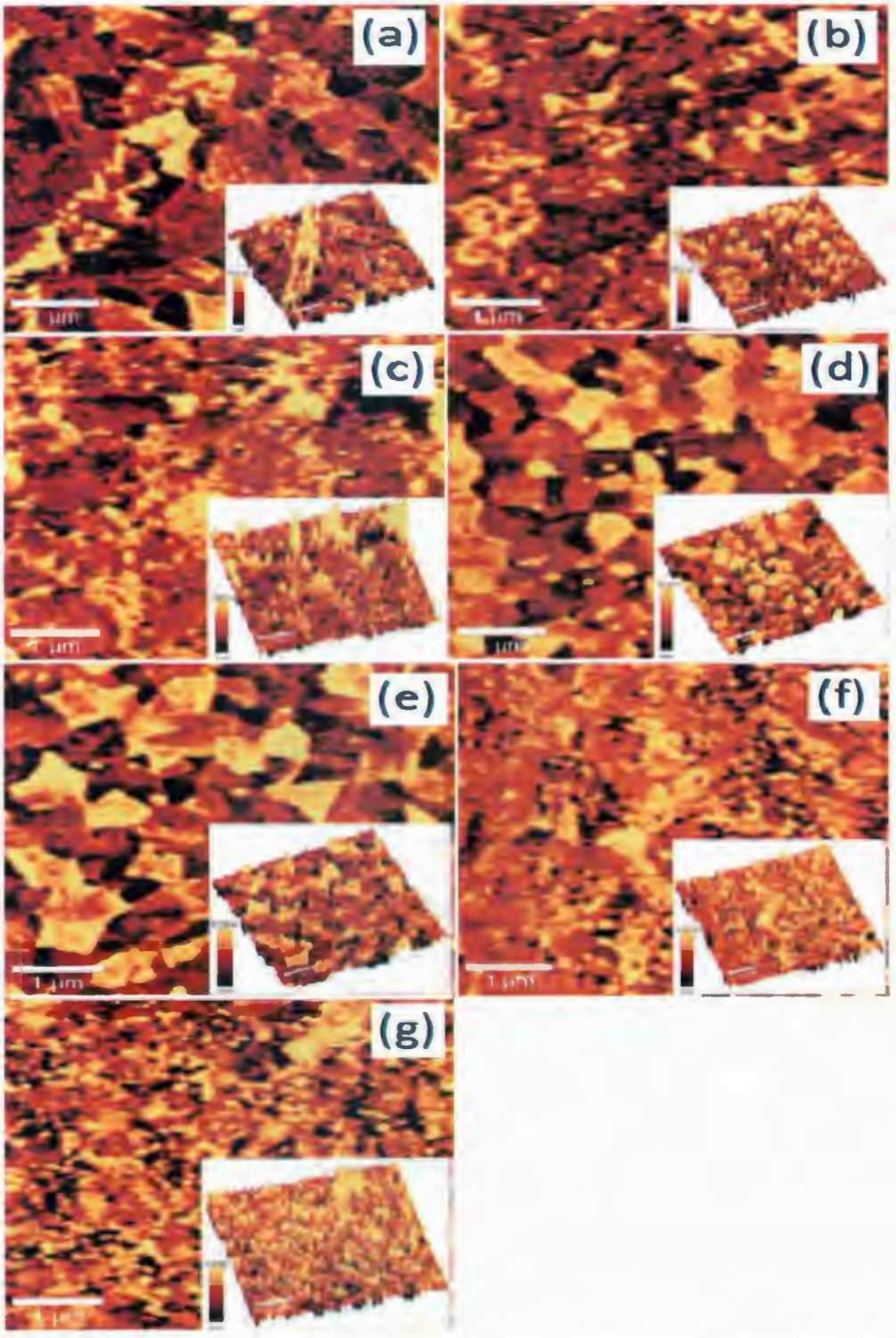

Figure 2.3: AFM images of (a) an untreated ITO substrate, and ITO substrates processed with (b) HCl, (c) NaOH, (d) UV1, (e) UV2, (f) HCl + UV1, and (g) HCl + UV2 treatments.

or HCl solution treatment combined with UV light treatments. Different treatments result in different surface morphology and roughness, are listed in Table 2.1. Untreated ITO substrate possesses a relatively rough surface with a high rms value (σ) of 65.7 nm. NaOH and HCl treatments result in a similar rms value of ~54.6 and 53.4 nm, respectively. HCl solution treatment followed by UV ozone produces a smooth surface with an rms value of 50.2 nm. The UV ozone treatments slightly decrease the surface roughness to 51.4 nm, and an rms value of ~28.9 nm is found when the UV light intensity is increased to UV2. The experimental results indicate that the UV light treatment results in a reduction of surface roughness.

Table.2.1: Changes in the rms roughnesses of the ITO films after different surface treatments.

ITO treatment	rms roughness (nm)
Untreated	65.7
HCl	53.4
NaOH	54.6
UV1	51.2
UV2	28.9
HCl+UV1	50.2
HCl+UV2	46.4

All treatments employed in this work yield rms roughnesses between 28.4 and 66.3 nm, which are higher than the values reported by Djurišić *et al.* from their ITO treatments [30]. The reason for this is that, in our experiment, the ITO substrates have been first etched by 36.6% concentrated HCl solution for 30 min in order to acquire patterns of organic solar cells, followed by ITO treatments with different approaches. These untreated and treated ITO substrates were stick by the PVC tape during the etching procedure, however, they immersed in a strong acid environment. Since the ITO surface rms roughness increases as a function of the etching time [65] and the roughness of the ITO depends on their initial condition (ITO used in Djurišić experiment

purchased from China Southern Glass Holding Co. Ltd), it is not surprising to find the difference between our results and those in Ref. [30]

Table 2.2: Changes in the sheet resistances of the ITO films after different surface treatments.

Treatment	Initial resistance (Ω/□)	Resistance after treatment (Ω/□)	Resistance difference (Ω/□)
Untreated	10.48	—	—
HCl	10.96	14.58	3.62
NaOH	11.59	11.19	-0.4
UV1	12.27	11.76	-0.51
UV2	9.21	8.38	-0.83
HCl + UV1	9.65	13.11	3.46
HCl + UV2	10.05	13.47	3.42

It should be noted that the obtained results are strongly dependent on the initial ITO used [30,65,69]. Even though the sheet resistance of the ITO glass substrates used in this study has been specified as 10 ± 5 Ω/□(sheet resistance unit) by the manufacture, the initial resistance of the ITO film was measured before each treatment in order to obtain accurate change in the sheet resistance. After treated by different methods, the sheet resistances were measured again and the results are summarized in Table 2.2. After HCl solution treatment, the sheet resistance of the ITO film increases significantly, however, after NaOH solution or UV light treatment (UV1 or UV2), the sheet resistance of the ITO film decreases. These results are in agreement with the results reported by Li *et al.* [69] and You *et al.* [70]. When a UV light of higher intensity (UV2) is adopted, the sheet resistance of the ITO film indicates a larger resistance difference of -0.83 Ω/□, as compared with -0.51 Ω/□ for the UV1 light treatment. This conclusion is also confirmed by HCl solution treatment followed by UV2 light treatment, the magnitude of the difference in the sheet resistance of ITO by this treatment (3.42 Ω/□) is lower than that for the HCl solution treatment followed by UV1 light treatment (3.46 Ω/□). UV2 light treatment in this experiment exhibits the lowest sheet resistance, which indicates a promising high performance of the devices.

The finding here is in agreement with the observation by Djurišić *et al.* that the lowest sheet resistance of ITO shows the highest device performance for CuPc/PCBM solar cells [30].

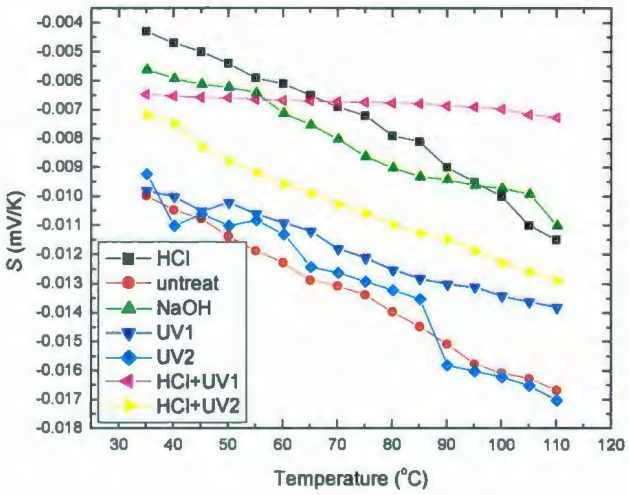

Figure 2.4: Seebeck coefficient versus temperature for the ITO films after different surface treatments.

Previous study on ITO surface treatments didn't reveal any simple relationships among the work function, sheet resistance, and the chemical composition of ITO [65]. The shifts in the work function and the changes in the carrier concentration after ITO treatments are still not well understood [30]. In order to study the carrier concentration, the dependence of the Seebeck coefficient on the temperature is shown in Fig. 2.4. The Seebeck coefficients measured in this study are in good agreement with a previous study on the Seebeck coefficient of pyrolytic ITO (16 μV/K) [30,83], which exhibits a nonlinear temperature dependence. The smallest Seebeck coefficient is obtained on the untreated ITO, while surface treatment results in an increased Seebeck coefficient, which is also in agreement with the results of Djurišić *et al.* [30]. According to Eq. (2.2), the Seebeck coefficient is proportional to the separation between the Fermi level and the conducting band, which indicates that surface treatments increase the separation between the

Fermi level and the conduction band. The largest separation obtained in this study is from HCl solution treatment.

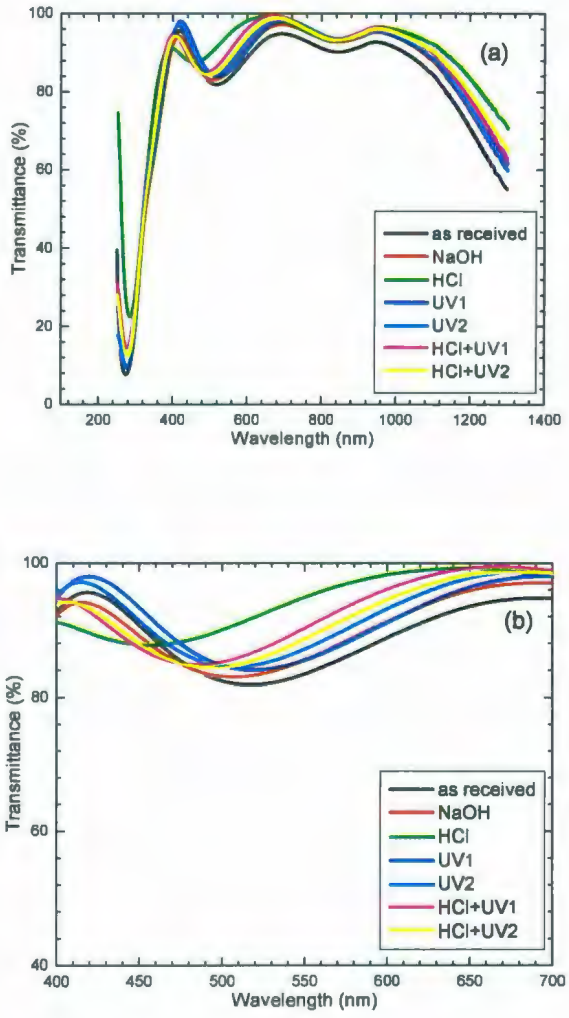

Figure 2.5: Transmittance spectra of the ITO films after different surface treatments in the wavelength range of 200 – 1300 nm (a) and 400 – 700 nm (b).

The transmittance spectra of the ITO before and after different surface treatments are examined in the UV-vis spectra (200-1300 nm), which is shown in Fig. 2.5. The relationship between these spectra is complicated, indicating that it is hard to identify which treatment will

result in a greater transmittance of ITO from 200 to 1300 nm. In order to match with the solar spectra (AM1.5G) of peaks mainly in the range of 400 – 700 nm, ITO treated with HCl exhibits the highest transmittance, followed by HCl+UV1, HCl+UV2, UV2, UV1, NaOH, and untreated ITO with the lowest transmittance from 530 to 680 nm. Lower transmittance means fewer photons can arrive at the active layer, which may result in a lower efficiency of the OSC.

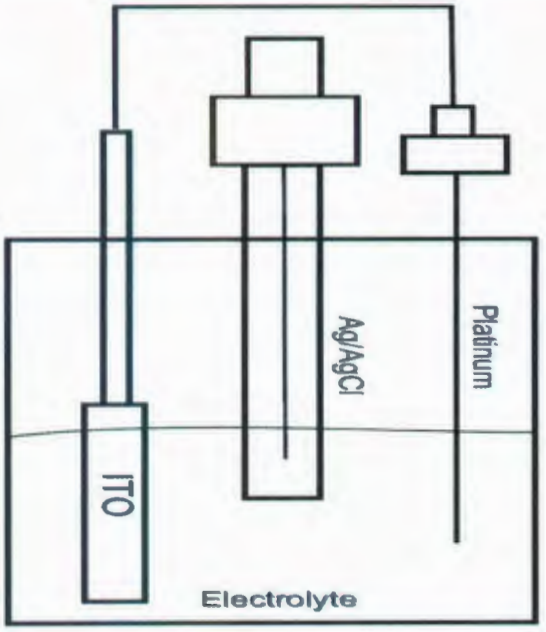

Figure 2.6: Schematic illustration of cyclic voltammetry measurement.

The work functions of ITO films with different treatments have been measured by cyclic voltammetric method (Epsilon-C3, Bioanalytical Systems, Inc.) in 0.1 M tetrabutylammonium tetrafluoroborate (TBATFB) acetonitrile solution, where the cyclic voltammetric system has been constructed using a three-electrode electrochemical cell consisted of an ITO and organic thin film sample as the working electrode, a platinum wire as the counter electrode, and Ag/Ag^{+} as the reference electrode (Fig. 2.6). The area of the ITO exposed to the electrolyte is about 0.5 cm^2 and the current densities are calculated with respect to this area. All presented potentials are

plotted against the saturated calomel electrode (SCE). The energy levels have been calculated using the ferrocence (FOC) value of -4.8 eV with respect to the vacuum level which is defined as zero [84]. Thus, the work function of ITO should be ($4.8 + V_{onset}$) eV [85]. Fig. 2.7 shows cyclic voltammetry of ITO before and after various treatments. Table 2.3 summarizes the work function of ITO before and after various treatments.

Table 2.3: Work functions of ITO films after different treatments

ITO	Work function (eV) ± 0.05	
	Initial	Treated
HCl	4.42	4.62
NaOH	4.59	4.52
UV1	4.23	4.56
UV2	4.21	4.61
HCl+UV1	4.24	4.64
HCl+UV2	4.35	4.49

It has been found that, after the acid (HCl) or UV treatment, the work function of ITO generally increases; however, the treatment with base (NaOH) decreases the work function. Therefore, the work function shifts due to the ITO surface acid-basicity. Acidic sites such as positively charged surface metal atoms can easily bind a hydroxyl group, while basic sites such as negatively charged surface oxygen atoms can easily bind a proton. Therefore, a mineral acid will protonate the surface and the anions accumulate on the top of the adsorbed protons, giving rise to a surface dipole (Fig. 2.8a). Similarly, the base will dissociate and form a surface bound hydroxyl layer on the ITO, and then protons are likely to assemble on the top of the hydroxyl layer (Fig. 2.8b). Thus, acid and base treatments generate opposite work function shifts [76]. In this experiment, UV treatments also improve the work function of ITO; it can be attributed to carbon removal from the ITO surface [86,87]. Oxidative treatments such as UV and oxygen plasma can decrease the atomic concentration of carbon [87].

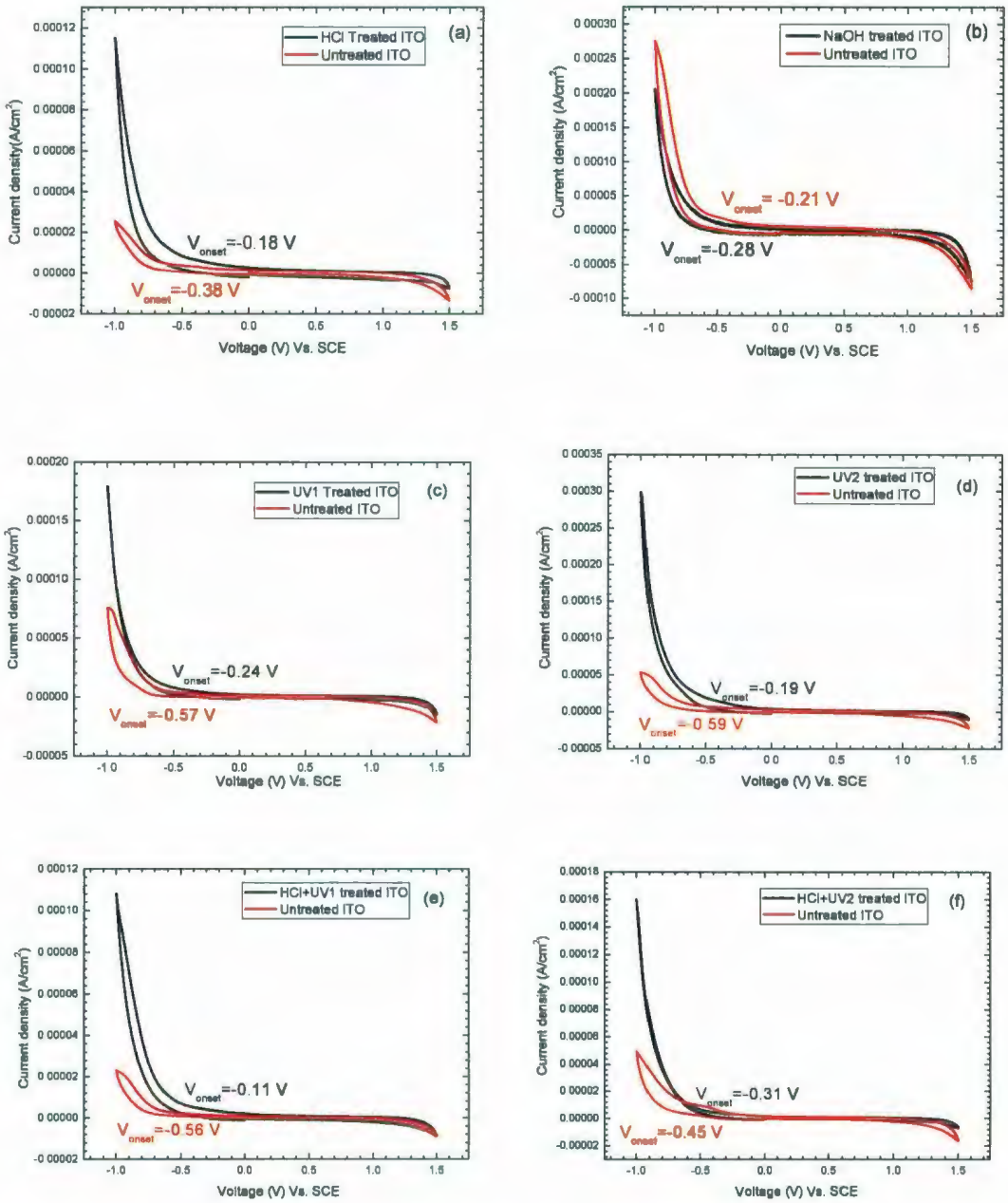

Figure 2.7: Cyclic voltammogram of ITO substrates for the measurement of work function: (a) HCl treatment, (b) NaOH treatment, (c) UV1 light treatment, (d) UV2 light treatment, (e) HCl treatment followed by the UV1 treatment, and (f) HCl treatment followed by the UV2 treatment.

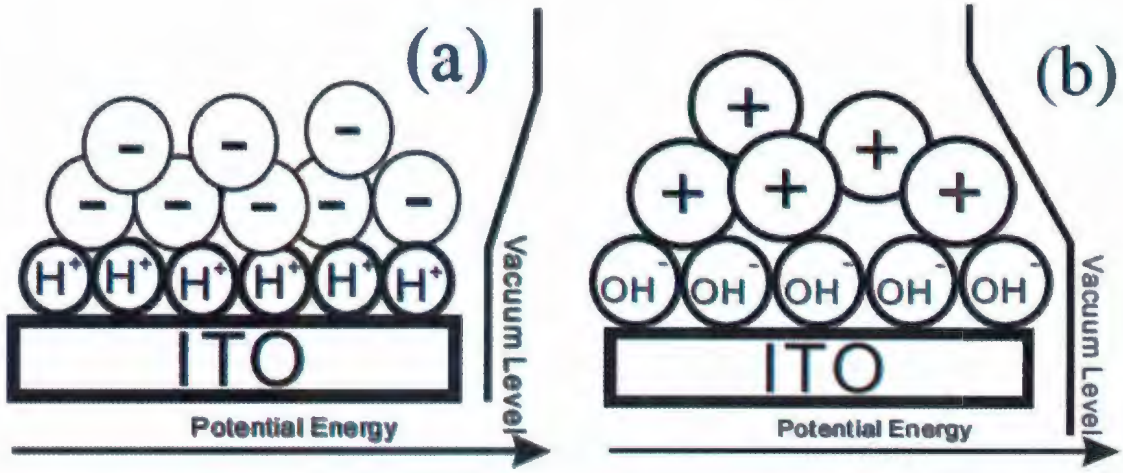

Figure 2.8: Illustration of the adsorption of acids (a) and bases (b) onto an ITO substrate.

Figure 2.9: Set-up of contact angle measurement.

The contact angle is the angle at which a liquid/vapour interface meets the solid surface, and their measurements have been performed using a FUJIFilm FINEPIXZ300 digital camera. The digital camera is mounted on a tripod to adjust its relative height and level for edge-on views of water or di-iodomethane (DIM) droplets. The ITO sample is placed on a lab jack covered by a black cloth, a portable lamp is mounted on the right of the ITO sample (Fig. 2.9), and a micro-

syringe is used to deposit a liquid drop of 3-4 μL on the surface of the substrate[88]. The steady-state contact angle was recorded within 30 s after the formation of the drop, and an average is obtained from the five readings. Distilled water and DIM (Aldrich, reagent plus grade) were chosen as test liquids with their surface energy parameters are listed in Table 2.4.

Table 2.4: Surface energy parameters of the test liquids (mJ/m^2)

Test liquid	γ_l^p	γ_l^d	γ_l
Distilled water	51.0	21.8	72.8
Di-iodomethane (DIM)	2.3	48.5	50.8

The surface energies of the ITO with different treatments have been calculated using the following equation applied to the two test liquids [89]:

$$(1+\cos\theta)\gamma_l = 2(\sqrt{\gamma_s^p \gamma_l^p} + \sqrt{\gamma_s^d \gamma_l^d}) \quad (2.4)$$

where θ is the contact angle, γ_l and γ_s are the surface energies of the test liquids and ITO substrate, respectively. γ^p and γ^d corresponds to the polar and the dispersive components of the total surface energy, respectively. After calculating γ_s^p and γ_s^d, the total surface energy γ_s and polarity χ_p can be obtained by the equations: $\gamma_s = \gamma_s^p + \gamma_s^d$ and $\chi_p = \gamma_s^p / \gamma_s$, respectively.

Figures 2.10 and 2.11 show the droplets of the distilled water and DIM on the untreated and treated ITO substrates, respectively. Software ImageJ [90] with a contact angle plug-in [91] was utilized to measure the contact angles from the captured images. Table 2.5 lists the measured contact angles of distilled water and DIM on the untreated and treated ITO substrates. The calculated surface energy and polarities of all ITO substrates is listed in Table 2.5, which shows that the surface energy and polarity are strongly dependent on the surface treatments. The water contact angles of the substrates decrease in the order of UV2, as-received, UV1, HCl, HCl+UV2,

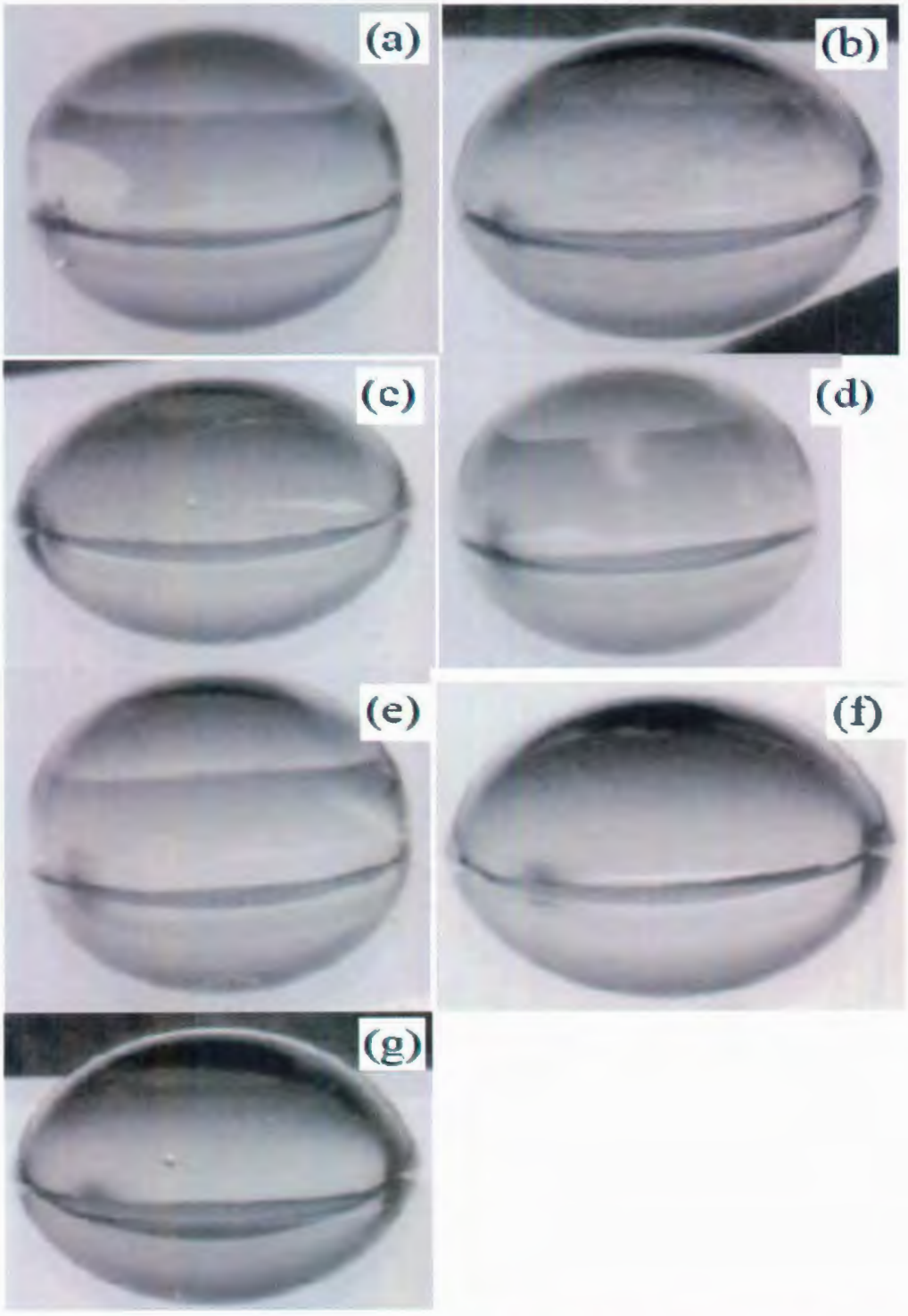

Figure 2.10: Representative images of distilled water droplets in contact with (a) untreated, (b) HCl, (c) NaOH, (d) UV1, (e) UV2, (f) HCl + UV1, and (g) HCl + UV2 treated ITO substrates.

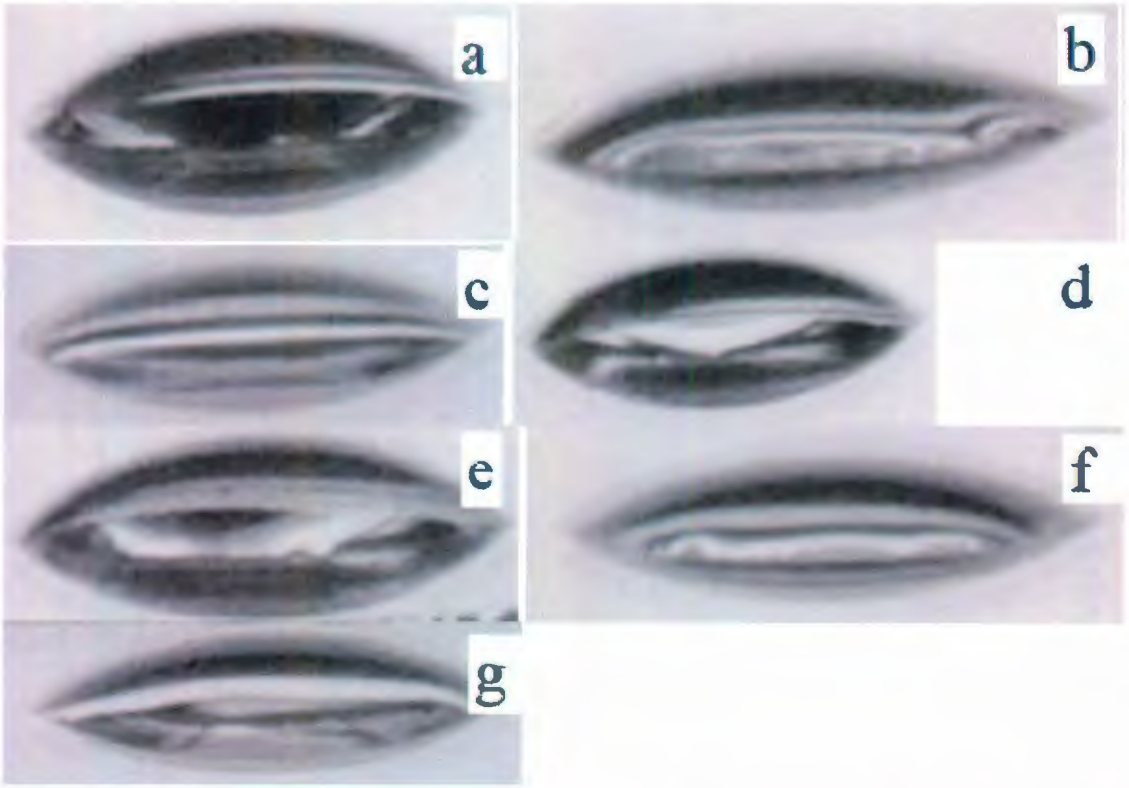

Figure 2.11: Representative images of DIM droplets in contact with (a) untreated, (b) HCl, (c) NaOH, (d) UV1, (e) UV2, (f) HCl + UV1, and (g) HCl + UV2 treated ITO substrates.

HCl+UV1, and NaOH treated ITO. NaOH treatment results in the largest decrease in the contact angle as compared with untreated ITO substrate, from 90.02° to 75.32°, which indicates that NaOH treated ITO substrate is highly polar [89]. The observation that the NaOH treated ITO substrate exhibits the minimum DIM contact angle (35.21°) is agreeable to the high polarity found on the NaOH treated ITO substrate. The increases in the surface energy and polarity can be attributed to the removal of hydrocarbon, which turns the surface more hydrophilic and raises the surface energy due to the fact that hydrocarbon possesses relatively low surface energy.

Table 2.5 Contact angles, surface energies, and polarities of untreated and treated ITO substrates.

Treatment	Contact angle (°)		Surface energy (mJ/m^2)	Polarity
	Distilled water	Di-iodomethane		
As-received	90.02	41.76	5.24	0.59
HCl	80.76	35.52	47.29	0.64
NaOH	75.32	35.21	73.41	0.59
UV1	85.19	42.20	15.65	0.68
UV2	92.42	43.41	55.73	0.42
HCl+UV1	78.23	38.85	8.78	0.24
HCl+UV2	80.63	37.86	53.94	0.21

After studying ITO properties with different surface treatments, bulk-heterojunction ITO/PEDOT:PSS/P3HT:PCBM/Al devices have been fabricated on ITO substrates after different ITO treatments. In Fig. 2.12, the *J-V* characteristics of seven devices with different ITO treatments are compared under AM 1.5 illumination with an intensity of 100 mW cm^{-2}. The device without ITO treatment shows a low performance with V_{oc} = 0.6 V, I_{sc} = 9.77 mA cm^{-2}, FF = 34.3%, and a resultant PCE value of η_e = 2.01%. UV treatments improve the short circuit current to 10.8 mA cm^{-2}, and for UV2 treatment, the short circuit current is further increased to 15.3 mA cm^{-2}. The results indicate that the short circuit current increases with the increase in the intensity of UV light, since UV2 intensity (~23 mW/cm^2) is much higher than UV1 intensity (~1 mW/cm^2). This improvement in the device performance with the UV treatments is also proved by the devices with HCl solution treatment combined with different UV light irradiation. HCl solution treatment, whether alone or in combination with either UV1 or UV2 ozone, raises the short circuit current to 11.9, 11.3, and 12.9 mA cm^{-2}, respectively. For the HCl solution treatment, the fill factor slightly decreases from 34.3% to 33.7%, whereas after being combined with UV1 or UV2 treatments, fill factor increases to 42.1% and 36.5% respectively. Thus it can be

concluded that UV light of appropriate intensity can effectively improve the fill factor, however, excess UV intensity decreases the fill factor. Figure 2.12 clearly indicates that UV1 and UV2 treatments are powerful in enhancing the short circuit current and fill factor, which are 10.8 mA cm^{-2} and 43.2%, and 15.3 mA cm^{-2} and 39.8%, respectively. The summary of the device performance for different devices with different ITO treatments is listed in Table 2.6.

The comparison of the device performance, evident from Table 2.7, signifies the importance of the surface roughness and morphology of the ITO. The surface of UV2 treated ITO film exhibits the smallest roughness, indicating that the performance of the device has a close relationship with the nanoscale morphology of the organic solar cells.

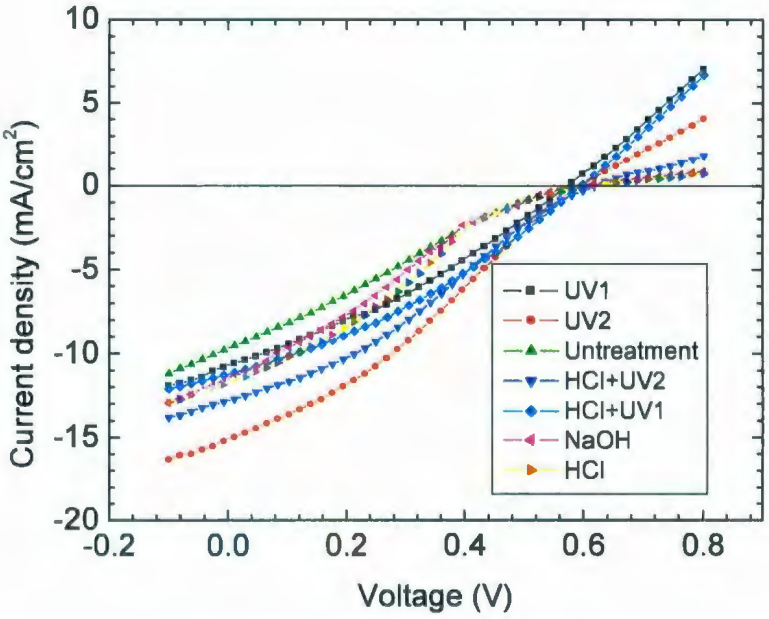

Figure 2.12: Current density - voltage (*J-V*) characteristics of P3HT:PCBM heterojunction cells with different ITO treatments under AM 1.5G illumination.

Table 2.6: Summary of the device performance of the P3HT:PCBM heterojunction cells prepared on ITO substrates after different treatments.

ITO treatment	J_{sc} (mA cm^{-2})	V_{oc} (V)	FF (%)	PCE (%)
Untreated	9.77	0.60	34.3	2.01
NaOH	11.7	0.60	34.4	2.41
HCl	11.9	0.62	33.7	2.49
UV1	10.8	0.58	43.2	2.70
UV2	15.3	0.60	39.8	3.65
HCl + UV1	11.3	0.60	42.1	2.86
HCl + UV2	12.9	0.62	36.5	2.92

which is also in agreement with the results of Djurišić *et. al.* [30]. Thus, it can be concluded that the surface roughness and the ITO morphology play a significant role in the performance of an organic solar cell. ITO roughness and morphology influence the fabricated devices and hence the exciton dissociation, which will depend on the substrate used. In addition, ITO interface will also play a role in the carrier collection. The highest efficiency of the device is obtained by UV2 treated ITO, which possesses the lowest sheet resistance (Rs) and the highest work function.

Table 2.7 Comparison of the performance of the ITO/PEDOT:PSS/P3HT:PCBM/Al devices and ITO properties after different treatments.

ITO treatment	PCE (%)	Roughness (nm)	ΔRs (Ω/□)	Δ (work function) (eV)	Surface energy (mJ/m^2)	Polarity
As-received	2.01	65.7	N/A	N/A	5.246	0.592
HCl	2.41	53.4	3.62	0.2	47.293	0.648
NaOH	2.49	54.6	-0.4	-0.1	73.413	0.599
UV1	2.70	51.2	-0.51	0.3	15.651	0.689
UV2	3.65	28.9	-0.83	0.4	55.732	0.425
HCl+UV1	2.86	50.2	3.46	0.4	8.783	0.241
HCl+UV2	2.92	46.4	3.42	0.1	53.947	0.217

2.4 Conclusions

In summary, effects of different surface treatments (NaOH, HCl, UV1, UV2, HCl + UV1, HCl + UV2) on the ITO properties (sheet resistance, surface roughness, morphology, Seebeck coefficient, transmittance, work function, and contact angle) have been studied on the performance of organic solar cells. All of these treatments improve the roughness of the ITO surface. Four point probe measurement shows that HCl solution treatment increases the sheet resistance, while UV and NaOH solution treatments yield a lower sheet resistance. HCl solution treatment also generates the largest separation between the Fermi level and the conducting band as well as the lowest Seebeck coefficient. Furthermore, the influences of the surface treatments of the ITO substrates on the characteristics of organic solar cells have been studied by the photovoltaic properties of the devices. Experimental results indicate that UV2 treatment on the ITO substrate increases the short circuit current and the fill factor, and consequently, improves the device performance.

Chapter 3

High efficient organic solar cells with a modified buffer layer

Abstract

In this study, the effect of two different kinds of PEDOT in the PEDOT:PSS layer is investigated, i.e., Clevios PVP Al4083 (Al4083) and Clevios PH510 (PH510). The composition of the PEDOT component in the PEDOT:PSS layer is varied from pristine Al4083 to pristine PH510 with the following volume percentages of PH510 in Al4083: 0, 25, 29, 33, 40, 50, 67, and 100. The relationship between the conductivity of the PEDOT:PSS layer, light transmission, and the performance of the organic solar cells has been systematically investigated. Specifically, addition of PH510 into Al4083 solution increases the conductivity of the spin coated PEDOT buffer layer, but remarkably reduces the transmission of the buffer layer. In order to achieve the

highest power conversion efficiency (PCE), an optimized ratio of PH510 and Al4083 at 1:2.5 (29 wt% of PH510) is identified as a buffer layer in the organic solar cells, for which a short circuit current (I_{sc}) of 12.06 mA/cm^2, open-circuit voltage (V_{oc}) of 0.6 V, and PCE of 2.92% under AM 1.5G (100 mW/cm^2) condition are achieved under ambient atmosphere. In addition, optical modeling of organic PV devices with different buffer layers is used to compare the optical electric field distributions in the case of pristine Al4083. It is found that the field distribution is slightly more advantageous for the optimized mixture.

3.1 Introduction

Poly(3,4-ethylenedioxythiophene) (PEDOT) doped with poly(styrenesulfonate) (PSS) has been applied in polymer optoelectronic devices, such as light emitting diodes [92,93], thin-film transistors [94,95], and organic solar cells [10] owing to the prospect of relatively high conductivity [96,97,98], high transmission [96], and solution-based manufacturing via spin coating. In organic solar cells, PEDOT:PSS is usually used to match the photoanode Femi Level to the energy of the polymer HOMO and also acts as a hole transporting layer [27]. From Eqs. 1.3-1.5, mobility is inversely proportional to the sheet resistivity, and proportional to the conductivity. Clevios PVP Al 4083 is the most commonly used PEDOT:PSS material in organic solar cells [10,49,15,99]. Recently, a new type of PEDOT:PSS with high conductivity, i.e. Clevios PH510, has been available as a polymer anode in OLEDs [100] or OSCs [96,101,102,103]. For an ideal PV device, a low series resistance is required, which includes the resistance of the active layer, metal-organic contact, the electrodes, and the buffer layer

[104,105,46]. A mismatched PEDOT:PSS layer will reduce the I_{sc} and FF owing to the increased series resistance [106]. In this study, the effects of the conductivity of the buffer layer on P3HT:PCBM PV devices are investigated, by using several different buffer layer systems based on PH510, Al4083 and combinations of them. Different conductivities are obtained by doping Al4083 with 25, 29, 33, 40, 50, and 67 vol% of PH510.

With regard to another limitation of light absorption in the active layer, the transfer matrix formalism (TMF) is used in this study in order to evaluate the photon absorption in the PV devices and the internal optical electrical field distribution $|E|^2$ inside the devices. This approach has already been explained elsewhere [107,108], and applied several times to OSCs [109,110,111]. However, it is used here to examine P3HT:PCBM PV systems that make use of PH510, Al4083 and mixtures thereof as the buffer layers. Moreover, it is seen that $|E|^2$ is strongly influenced by the interference effects, and a maximum of 89% in the absorption of the incident photons is revealed to occur at 500 nm.

3.2 Experimental details and optical modeling

3.2.1 Device fabrication

A composite solution with 10 mg/ml P3HT (American Dye Source, Inc.) and PCBM (Nano-C, Inc.) in 1:0.8 wt ratio is prepared using 1,2-dichlorobenzene solvent. The polymer PV devices are fabricated with a typical sandwiched structure of ITO/PEDOT:PSS/P3HT:PCBM/Al. The ITO coated glass substrates are subsequently cleaned in ultrasonic bath by acetone, alcohol,

and distilled water for 30 min each. PEDOT P100, P67, P50, P40, P33, P29, P25, and P0 are prepared by adding 100, 67, 50, 40, 33, 29, 25 and 0 volume percentage of PH510 (H. C. Starck) to PVP Al4083 (H. C. Starck), and then each PEDOT:PSS solution is stirred for ~24 h before using. The PEDOT layer is spun cast at 4000 r.p.m. for 120 s from the pre-dissolved composite PEDOT solution after filtering through a 0.45 μm syringe filter. The PEDOT:PSS layer is baked on a hot plate at 100 °C for 5 min. A blended solution with a P3HT:PCBM ratio of 1:0.8 is stirred at 40 °C for 24 h. After that, the 1, 2-dichlorobenzene solution comprising P3HT (10 mg/ml) and PCBM (8 mg/ml) is spin-casted at 700 r.p.m. for 40 s on the top of the PEDOT layer. Finally, an Al film is thermally deposited on the top of the active layer as a cathode. After vacuum evaporation, the device is thermally annealed at ~150 °C for 30 min, and then the device is stored inside a covered petri-dish and cooled to room temperature before measurements. Current density-voltage (*J-V*) characteristics of all polymer PV cells are measured by KEITHLEY 2420 under the illumination of simulated solar light with 100 mW/cm^2 (AM1.5G) by Newport Oriel 96000 150 W solar simulator. Optical transmission spectra are obtained by Cary 6000i spectrophotometer (Varian Inc.). Surface sheet resistance is determined from four point probe (4pp) measurements (Fig. 2.2), which has been described in Chapter 2.2.

3.2.2 Optical modeling

The methods of using TMF to evaluate the photon absorption and the internal optical electrical field distribution $|E|^2$ inside the PV device have been described by O. Inganäs [109], which is briefly summarized below:

Considering a plane wave incident from the left at a general multilayer structure having m layers between a semi-infinite transparent ambient and a semi-infinite substrate, each layer j (j=1, 2,...., m) has a thickness d_j and its optical properties are described by its complex index of refraction $\tilde{n} = \eta + ik$, where η is the refractive index and k is the extinction coefficient. An interface matrix describing each interface in the structure is

$$I_{jk} = \frac{1}{t_{jk}} \begin{bmatrix} 1 & r_{jk} \\ r_{jk} & 1 \end{bmatrix}, \tag{3.1}$$

where r_{jk} and t_{jk} stand for the Fresnel complex reflection and transmission coefficients at interface jk, respectively. The Fresnel complex reflection and transmission coefficients are expressed in the form

$$r_{jk} = \frac{q_j - q_k}{q_j + q_k} \tag{3.2a}$$

$$t_{jk} = \frac{2q_j}{q_j + q_k} \tag{3.2b}$$

for light with electric field perpendicular to the plane of incidence (s-polarized or TE waves), and

$$q_j = \tilde{n}_j \cos\phi_j = [\tilde{n}_j^2 - \eta_0^2 \sin\phi_0]^{1/2}$$

where ϕ_j is the angle of refraction in layer j. $\tilde{n}$ is complex index of refraction, ϕ_0 is the angle of incidence, in this calculation, I assume ϕ_0 is 0, thus, q_j is simplified to $\tilde{n}_j$ The layer matrix of the propagation through layer j is given by

$$L_j = \begin{bmatrix} e^{-i\xi_j d_j} & 0 \\ 0 & e^{i\xi_j d_j} \end{bmatrix} \tag{3.3}$$

and

$$\xi_j = \frac{2\pi}{\lambda} q_j \tag{3.4}$$

where $\xi_j d_j$ presents the layer phase thickness, which is related to the phase change that the wave experiences as it traverses layer j. From the interface matrix and the layer matrix of Eqs. (3.1) and (3.3), the total system transfer matrix S can be written

$$S = \begin{bmatrix} S_{11} & S_{12} \\ S_{21} & S_{22} \end{bmatrix} = \left(\prod_{v=1}^{m} I_{(v-1)v} L_v\right) \cdot I_{m(m+1)} \tag{3.5}$$

In this formalism, the optical electric field in layer j, E_j, is broken down into a component propagating to the right E^+_j, and out to the left E^-_j; S relates the components of the field in the ambient to those in the substrate in the following way,

$$\begin{bmatrix} E_0^+ \\ E_0^- \end{bmatrix} = S \begin{bmatrix} E_{m+1}^+ \\ E_{m+1}^- \end{bmatrix} \tag{3.6}$$

When the light is incident from the ambient side in the positive x direction, there is underlined propagation in the negative x direction inside the substrate, which means $E^-_{m+1} = 0$. In our case, the substrate is the aluminum. For the total layered structure, the resulting complex reflection and the transmission coefficients can be expressed by using the matrix elements of the total system transfer matrix of Eq. (3.5) as

$$r = \frac{S_{21}}{S_{11}} \tag{3.7}$$

$$t = \frac{1}{S_{11}} \tag{3.8}$$

To calculate the internal electric field in layer j, the layer system can be separated into two subsets, divided by layer j, and then the total system transfer matrix can be written as

$$S = S_j^{'} L_j S_j^{''} \tag{3.9}$$

The left boundary $(j\text{-}1)j$ partial system transfer matrices for layer j are defined as

$$S_j^{'} = \begin{bmatrix} S_{j11}^{'} & S_{j12}^{'} \\ S_{j21}^{'} & S_{j22}^{'} \end{bmatrix} = (\prod_{v=1}^{j-1} I_{(v-1)v} L_v) \cdot I_{(j-1)j} \tag{3.10}$$

and the right boundary $j(j+1)$ partial system transfer matrices for layer j are described by

$$S_j^{''} = \begin{bmatrix} S_{j11}^{''} & S_{j12}^{''} \\ S_{j21}^{''} & S_{j22}^{''} \end{bmatrix} = (\prod_{v=j+1}^{m} I_{(v-1)v} L_v) \cdot I_{m(m+1)} \tag{3.11}$$

The expression of the total electric field in an arbitrary plane in layer j at distance x to the right of boundary $(j\text{-}1)j$ is given by

$$E_j(x) = \frac{S_{j11}^{''} \cdot e^{-i\xi_j(d_j - x)} + S_{j21}^{''} \cdot e^{-i\xi_j(d_j - x)}}{S_{j11}^{'} S_{j11}^{''} \cdot e^{-i\xi_j d_j} + S_{j12}^{'} S_{j21}^{''} \cdot e^{-i\xi_j d_j}} E_0^{+} \tag{3.12}$$

where $0 \le x \le d_j$, we are considering the case where $\phi_j = 0$.

3.3 Results and discussion

3.3.1 Properties of PV devices with different buffer layers

Figure 3.1 shows the *J-V* characteristics of the cells with P0, P25, P29, P33, P40, P50, P67, and P100 layer, respectively.

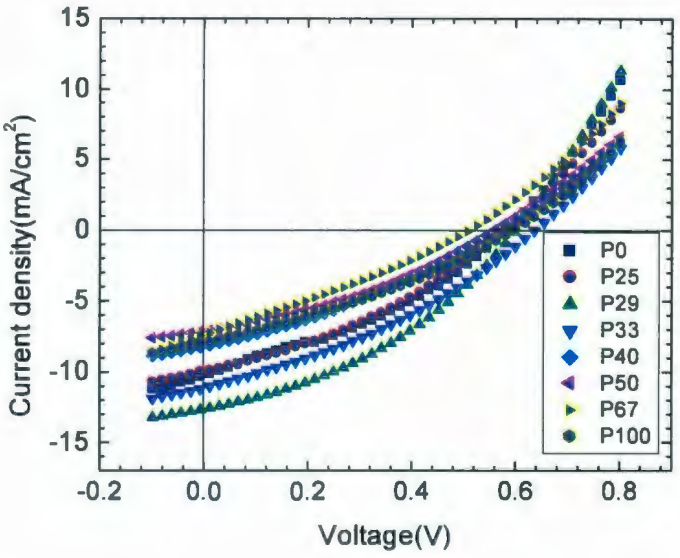

Figure 3.1: *J-V* characteristics of P3HT:PCBM devices with buffer layers of PEDOT Al4083 doped with different amounts of PH510 under AM 1.5G solar illumination.

Figure 3.2 shows the PV performance such as I_{sc}, V_{oc}, FF, and PCE under the AM 1.5 conditions of P3HT:PCBM solar cells with buffer layers of Al4083 doped with PH510 of different concentrations. The performance of the cells with different concentrations varies significantly, which is due to the sensitivity to the processing conditions and characterization in ambient conditions [112]. Each data point in this figure is the average of eight devices prepared under the identical conditions, yielding uncertainties within ±7.5%. The reference cell, which is the cell with pristine Al 4083 buffer layer, has I_{sc} = 10.3 mA/cm^2, V_{oc} = 0.58 V, FF = 32%, and a resulting PCE = 2.1%. The addition of a low wt% of PH510 shows a similar value of I_{sc}, V_{oc}, FF, and PCE. The photovoltaic parameters reach a maximum for the devices with a PH510 volume percentage of 29. The achieved values are I_{sc} = 12.66 mA/cm^2, V_{oc} = 0.6 V, FF = 0.39, and PCE = 2.9 %. For the cells with higher PH510 weight percentages (33%, 40%), the photovoltaic

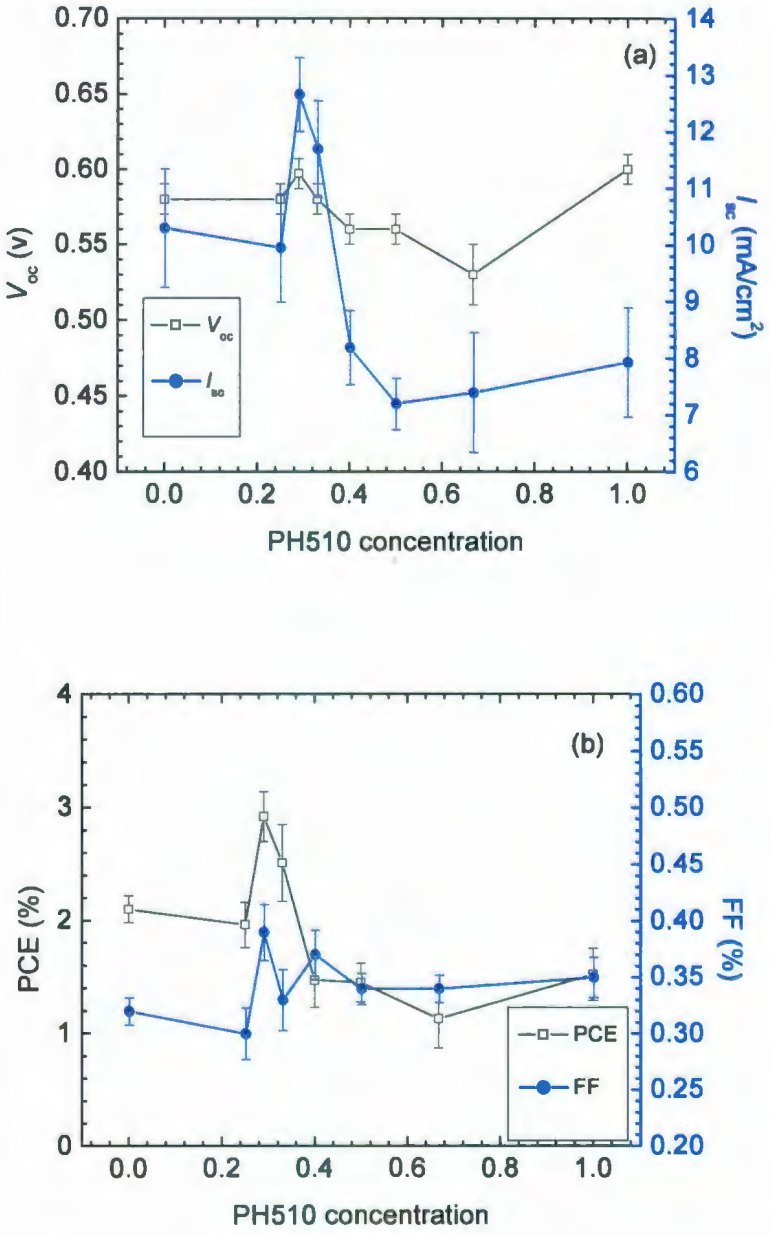

Figure 3.2: Photovoltaic performance of P3HT:PCBM bulk heterojunction devices processed with Al4083 buffer layers doped with different amounts of PH510.

performance rapidly decreases. The corresponding PCE are 2.51 and 1.47%, respectively. After increasing PH510 wt% to 50% and 67%, the performance of the PV devices decreases gradually with PCE = 1.45% and 1.13%, respectively.

From Fig. 3.2, V_{oc} remains nearly constant at 0.56 $\pm$ 0.04 V, which is agreeable with the fact that V_{oc} is a parameter dependent on the nature of the materials used and the structure of the devices [112]. Since I_{sc} is a parameter sensitive to the series resistance of the device and the absorption of the active layer, I_{sc} of the cells here reach a maximum for a buffer layer with 29% PH510 in Al4083 PEDOT.

To confirm the effect of PH510 addition on the conductivity of the PEDOT buffer layer, the current-voltage (*I-V*) characteristics of a modified PEDOT buffer layer deposited on a glass substrate are measured. The conductivity is estimated by the Eqs. (1.3) – (1.5). The resistances of these PH510 treated PEDOTs (R) are obtained from 4pp measurement and shown in Fig. 3.3. The resistance is gradually reduced by adding PH510 as expected. According to Eq. (3.5), the conductivity of modified PEDOT layer can be calculated from the slopes of curves in Fig. 3.3 and summarized in Fig. 3.4.

The conductivity is inversely proportional to the resistance and gradually increases by adding PH510 as expected. From the photovoltaic performance curve (Fig. 3.2), the photovoltaic parameters reach a maximum for the devices with a PH510 concentration of 29 vol%. At this percentage, the conductivity of the PEDOT buffer has been improved by more than 70 folds, from 0.0004 (pure Al4083) to 0.028 S/cm (29% PH510).

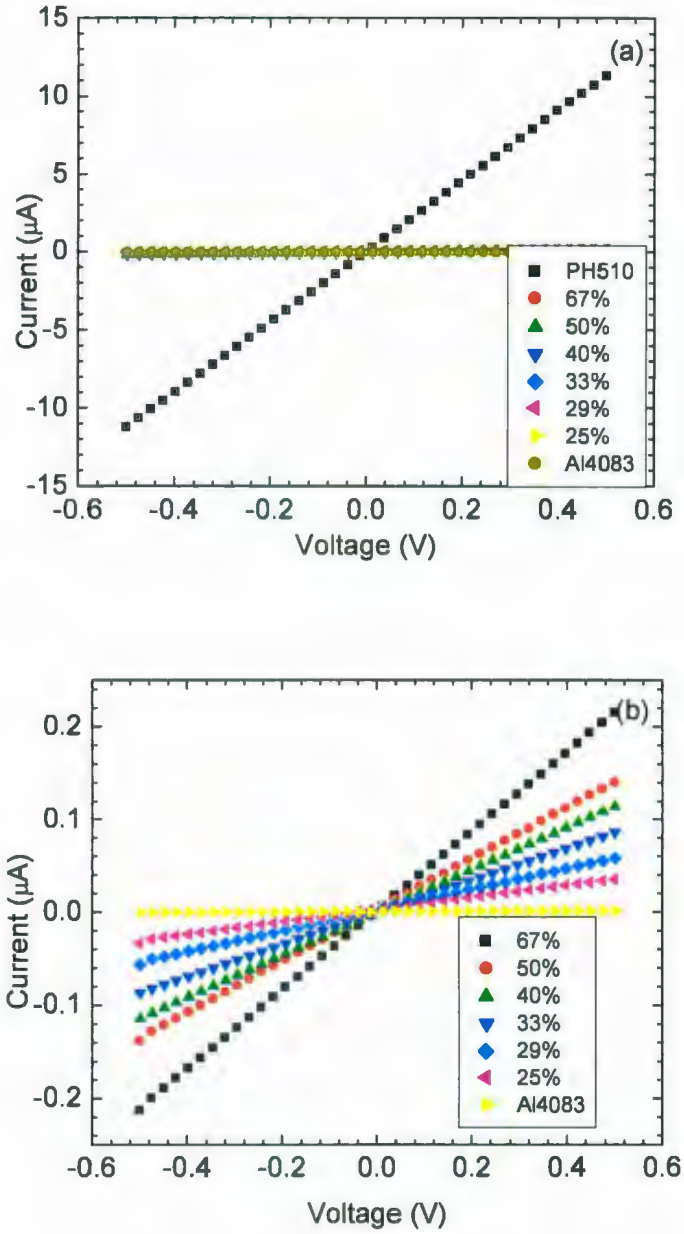

Figure 3.3: (a) Typical *I-V* curves for the Al4083 PEDOT film doped with PH510 of different concentrations. An enlarged figure without the curve for PH510 concentration of 100% is shown in (b).

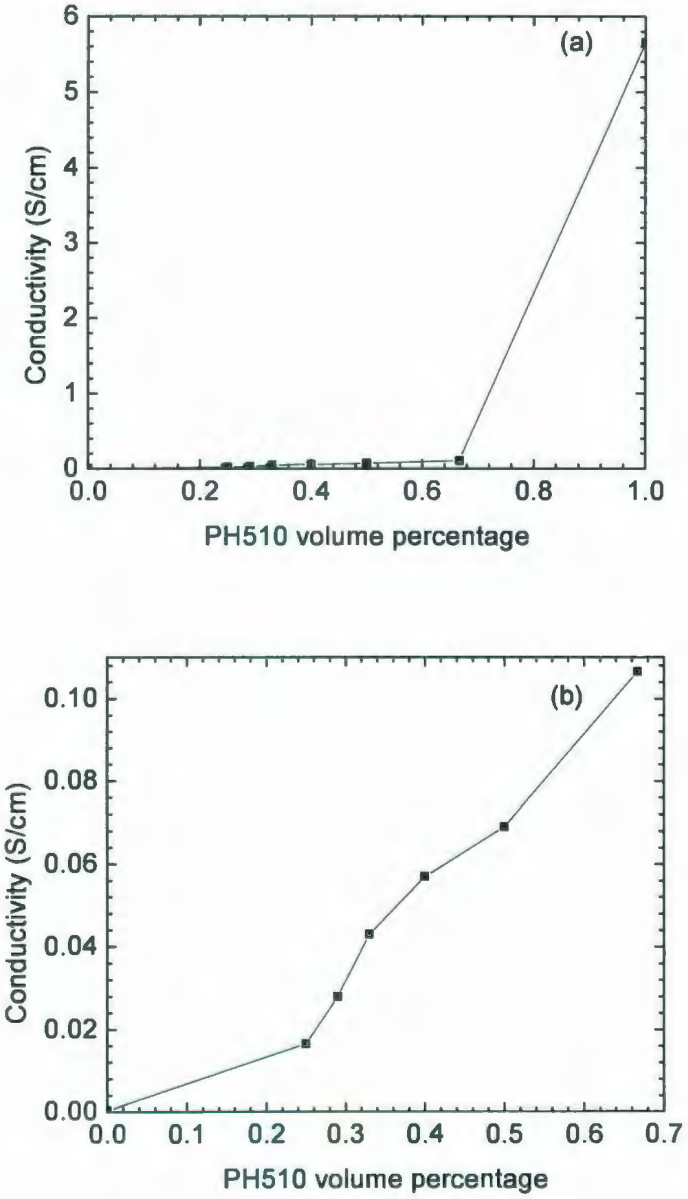

Figure 3.4: (a) Conductivities of the Al4083 PEDOT films doped with PH510 of different concentrations. An enlarged figure is shown in (b).

Figure 3.5 shows the atomic force microscope (AFM) images of the modified PEDOT film deposited on the glass substrate. It has been found that the surface of a pure Al4083 film is

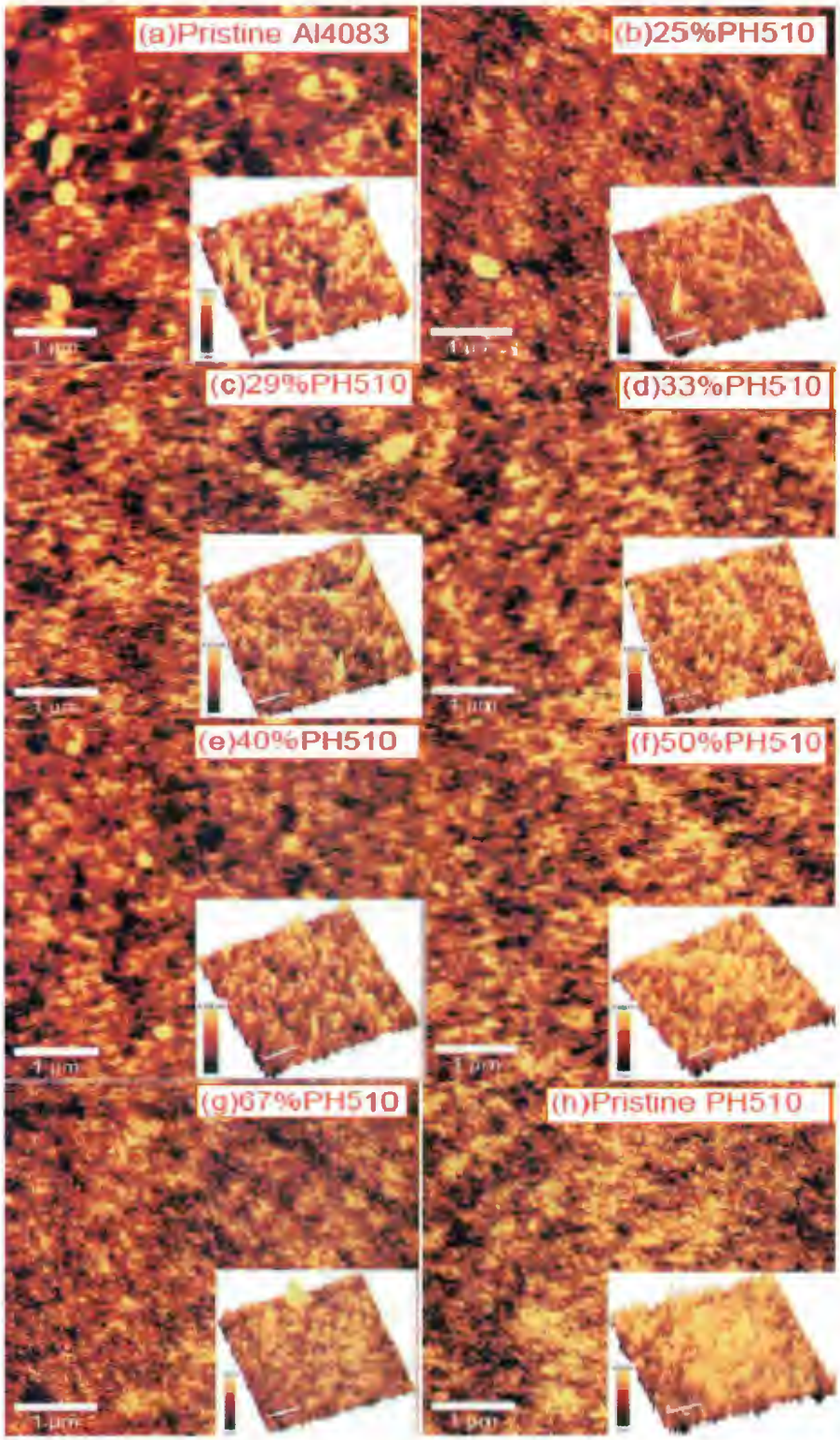

Figure 3.5: AFM images (5 μm×5 μm) of PEDOT films coated on glass substrates.

very rough. However, as the amount of PH510 is increased, the surface morphology of the modified PEDOT film becomes smooth (Fig. 3.6). The reason for that is due to the fact that the PEDOT:PSS ratios in the Al4083 and PH510 are different, in which Al4083 has a larger PEDOT:PSS ratio of 1:6, whereas PH510 has a smaller PEDOT:PSS ratio of 1:2.5. Since the active layer is directly deposited on the top of the PEDOT:PSS buffer layer, and the short circuit current I_{sc} is sensitive to the morphology of the active layer[112], thus the morphology of PEDOT buffer layer has a significant effect on I_{sc}.

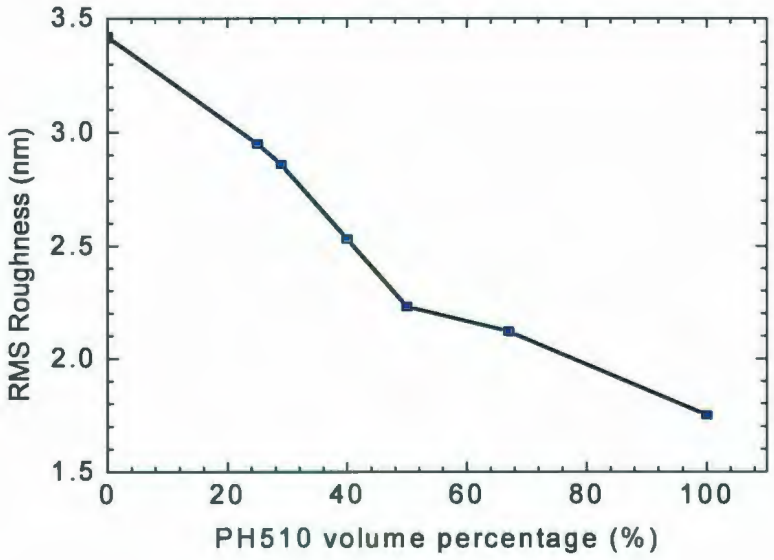

Figure 3.6: Root mean square roughnesses of PEDOT films with different PH510 volume percentages.

Transmission spectra of Al4083 PEDOT layer with different volume percentages of PH510 are shown in Fig. 3.7, indicating that the transmittance decreases gradually with the increase in the amount of PH510.

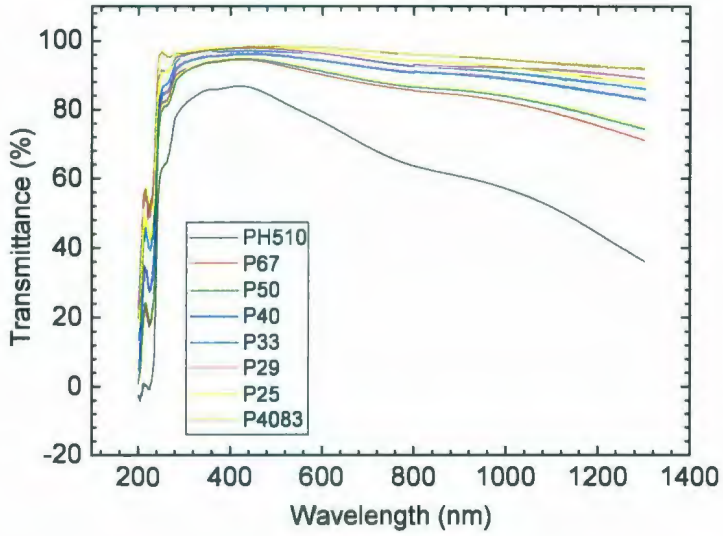

Figure 3.7: Transmission spectra of modified PEDOT:PSS films on glass substrates.

3.3.2 Optical modeling of P3HT:PCBM devices with modified buffer layer

In order to measure the optical electrical field distribution inside the device, the complex indices of refraction of the glass, ITO, and Al are extracted from literature [113,114]. The optical parameters (η and k) of modified PEDOT, and P3HT:PCBM used in the calculations then have been determined by a L116A ellipsometer from GAERTNER Corp. Assuming charge generation occur at the active layer, and the efficiency of the device is dependent on the distribution of the internal optical electrical field, thus, the maximized internal optical field in the active layer could increase the efficiency of the devices. In this part, the internal optical field distribution for different buffer layer is different. Reflection and absorption of the device with different ITO thickness were calculated. From these calculations, we are able to find the optimal thickness of

ITO; we then find that the optical electrical field distribution in the active layer is maximized by using ITOs of the optimal thickness.

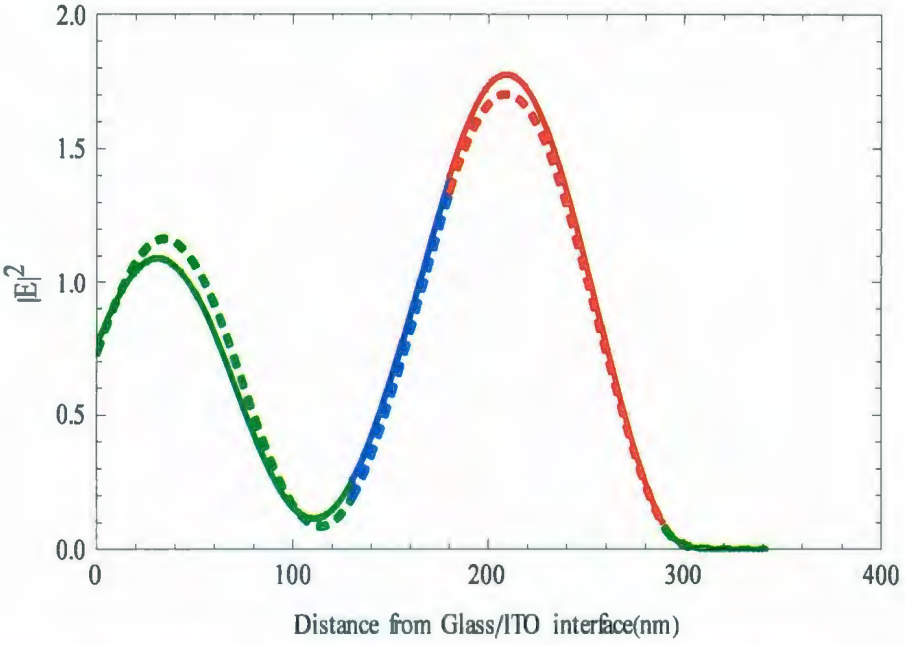

Figure 3.8: Calculated distribution of the normalized modulus squared of the optical electric field $|E|^2$ inside the photovoltaic device, ITO(130 nm)/PEDOT:PSS(Al4083) (50 nm)/P3HT:PCBM(110 nm) /Al (dash line) and ITO(130 nm)/PEDOT:PSS(29% PH510 in Al4083) (50 nm) /P3HT:PCBM(110 nm) /Al (solid line).

As stated in Section 3.2.2 on optical modeling, the generation of photoexcited species at a particular position inside the thin film structure is proportional to the product of the modulus squared of the electric field, the refractive index, and the absorption coefficient. The calculated distribution of the normalized modulus squared of the incident optical electrical field for two devices by using different PEDOT buffer layer (Al4083 and 29%PH510 in Al4083) for $\lambda = 632.8$ nm are shown in Fig. 3.8. The ellipsometer used only measures at 632.8 nm, and the solar light spectrum shows a great intensity (Fig. 2.4) at 632.8 nm. The active layer in the device is the

P3HT:PCBM layer, within which excitons form and dissociate. To increase the photocurrent, it is advantageous to maximize $|E|^2$ within the active layer, particularly near the interfaces with other layers in order to allow carriers to exit the active layer before recombining. Layer thickness and optical properties affect $|E|^2$ thoughout the cell. As seen in Fig. 3.8, $|E|^2$ within the active layer is different, with the modified buffer device showing a slightly larger (roughly 5%) $|E|^2$ in the active layer as compared with the regular Al4083 buffer layer device. Due to the optical interference between the incident (from the ITO side) and back-reflected light, the intensity of the light is nearly zero at the aluminum cathode.

In order to obtain the maximal light intensity in the active layer zone, the relationship between the ITO thickness and device reflection R is estimated in Fig. 3.9a. The reflectance is calculated by using optical constants at 633 nm. The reflectance is $R = |r|^2$, where r is defined by Eq. (3.7). Since the Al layer is much thicker than the incident depth of light at 633 nm, the total light absorption in the device equals to 1 - R, which is shown in Fig. 3.9b. According to the calculation of R and A (Fig. 3.10), devices show the lowest reflectance and the highest absorption by using a 100 nm ITO as the anode. The calculated distribution of the normalized modulus squared of the incident optical electric field for the device by using ITO of 100 nm thickness as the anode and modified PEDOT layer is shown in Fig. 3.10. Thus, the peak of the modulus squared of the optical electric field increases to 2 from 1.8, indicating a 10% increase in the generation of photo carriers.

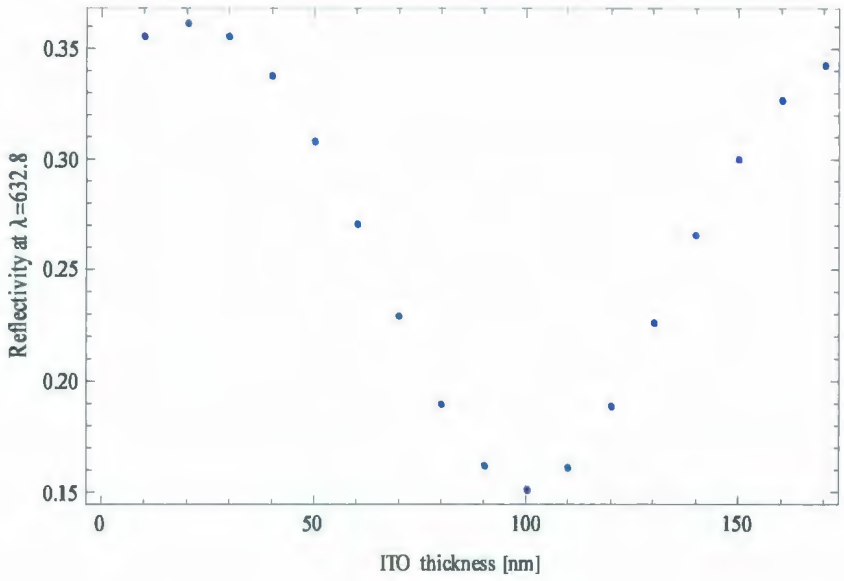

(a)

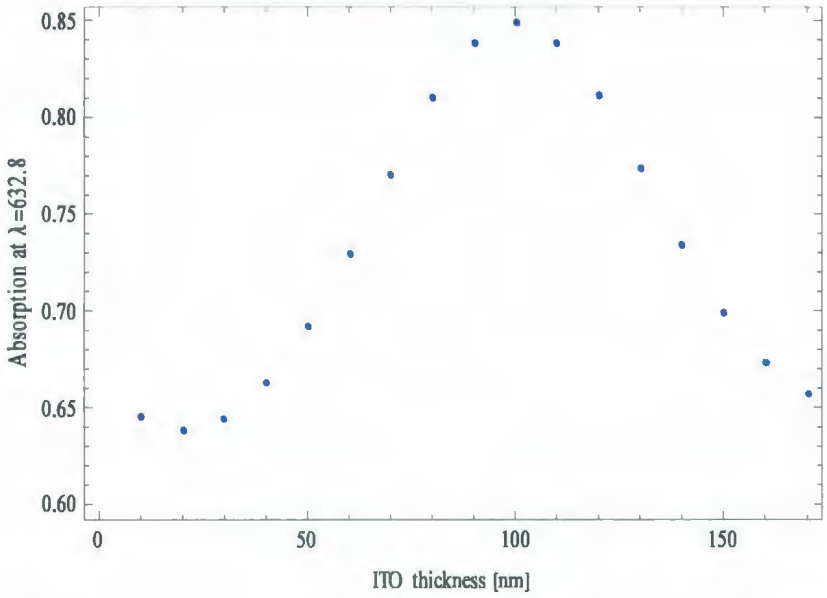

(b)

Figure 3.9: Calculated reflection *R* (a) and absorption *A* (b) from P3HT:PCBM devices with Al4083 doped with 29% PH510 buffer layer.

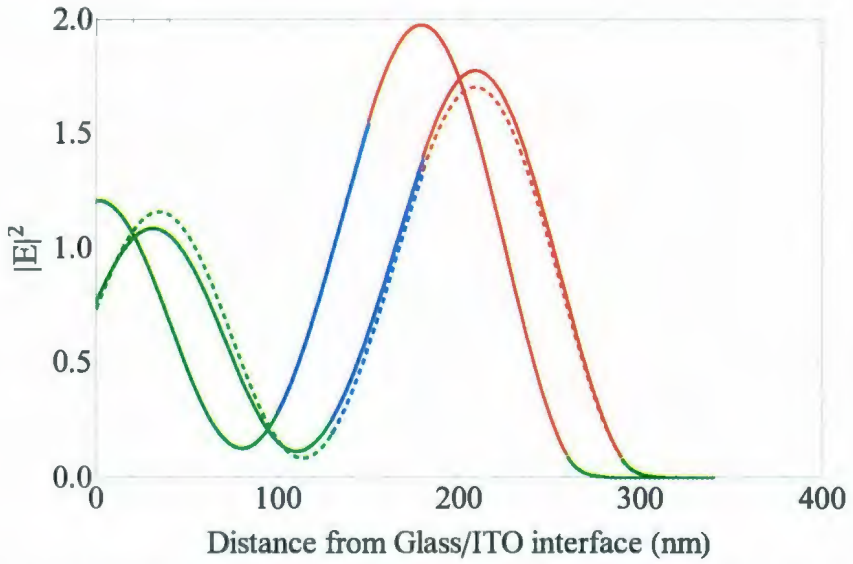

Figure 3.10: Calculated distribution of the normalized modulus squared of the optical electric field $|E|^2$ inside the photovoltaic device by using 100 nm thick ITO, compared with ITO (130 nm)/PEDOT:PSS(Al4083)(50 nm)/P3HT:PCBM(110 nm)/Al (dash line) and ITO(130 nm)/ PEDOT:PSS(29% PH510 in Al4083) (50 nm) /P3HT:PCBM(110 nm) /Al (solid line).

3.4 Conclusions

In this chapter, two typical PEDOT buffer layers (PH510 and PVP Al4083) and their mixtures with different ratios for applications in organic solar cells are investigated. By increasing the volume percentage of PH510 doped to Clevios PVP Al 4083, the conductivity increases as measured by 4pp method, however, the transmission and surface roughness decrease, as obtained by the respective spectrophotometer and AFM. The effect of different PEDOT buffer layers on the device performance of P3HT:PCBM photovoltaic cells is studied. Polymer solar cells with PCE approaching 3% have been achieved by using the buffer layer doped with 29% PH510 into Al4083, demonstrating a 40% increase in the PCE of the devices, as compared with the device adopting the regular Al4083 buffer layer. In order to reveal the mechanisms for the

increase in the PCE, optical modeling based on these two systems has beeen implemented, which shows that, the photovoltaic device with modified PEDOT buffer layer has a greater maximal absorption than the devices with the regular PEDOT buffer layer. The modulus squared of the electric field at the active layer of the photovoltaic device with modified buffer layer is larger than the modulus squared of the electric field at active layer of the photovoltaic device fabricated by the regular Al4083 buffer layer.

Chapter 4

Efficiency enhancement in solar cells by processing with additives

Abstract

The techniques to increase the PCEs of polymer photovoltaic cells are investigated by doping of additives. The doped BHJs in this study are polymer photovoltaic cells with poly [(2-methoxy-5-ethylhexyloxy)-1, 4-phenylenevinylene] (MEH-PPV) as the electron donor and [6,6]-phenyl-C61-butyric acid methyl ester (PCBM) as the electron acceptor. Two additives, i.e. 1,8-octanedithiol (ODT) or dimethyl sulfoxide (DMSO), have been used in this study. The measurement on the lifetimes of the photovoltaic cells has been carried out in ambient

environment. For the periods of time studied here (1000 min), the short circuit current I_{sc} and the efficiency decrease rapidly in the first 50 minutes. The effect on the performance of photovoltaic cells by incorporating a few volume percentages of additives in the solution for spin-cast is studied. After 1 vol% ODT doping, the efficiency of the photovoltaic cell has been improved from 2.5 to 2.8% accompanied by changes in the morphology of the bulk heterojunction. We propose for the first time to incorporate DMSO into MEH-PPV:PCBM bulk heterojunction and demonstrate the effectiveness of the doping effect from the significant increase in the PCE of the device. The efficiency of the photovoltaic cell increases from 1.75 to 3.15% by doping 5 vol% of DMSO. The power conversion efficiency of 3.15% achieved here is the highest value reported so far for the MEH-PPV:PCBM solar cells.

4.1 Introduction

Much of recent attention has focused on the blends of P3HT and PCBM with the corresponding bulk heterojunction reaching a high PCE value of 4.5 - 5% [12,10,13]. However, the open circuit voltage (V_{oc}) of the P3HT:PCBM composite is around 0.6 V, which is lower than the V_{oc} of MEH-PPV:PCBM devices (0.8 V). The following relationship has been reported from a comprehensive study of 26 different PCBM-polymer PV cells [27]:

$$V_{oc} = \frac{\left(\left|E_{HOMO(D)}\right| - \left|E_{LUMO(PCBM)}\right|\right)}{e} - 0.3 \tag{4.1}$$

where $E_{HOMO(D)}$ and $E_{LUMO(PCBM)}$ are the HOMO and LUMO energies of donor and PCBM, respectively. The HOMO energies of MEH-PPV and P3HT are -5.3 eV and -5.1 eV, respectively [115,28]. Therefore, V_{oc} of the MEH-PPV:PCBM solar cell is larger than that of the P3HT:PCBM device. Short circuit current (I_{sc}) and fill factor (FF) are the other important factors to determine the device's efficiency. However, I_{sc} and FF are sensitive to other factors, such as the thicknesses of the multilayers in the device, annealing temperature and duration, additives doped in the active layer, and solvents used to dissolve the organic materials for spin-coating. Recently, some papers reported techniques to enhance the efficiency of OSCs through the improvement of I_{sc} and FF [23,11]. Since the V_{oc} of MEH-PPV devices is higher than that of the device consisting of P3HT, the efficiencies of MEH-PPV devices possesses a possibility to achieve a value higher than that of the devices consisting of P3HT through the identification of optimal I_{sc} and FF values.

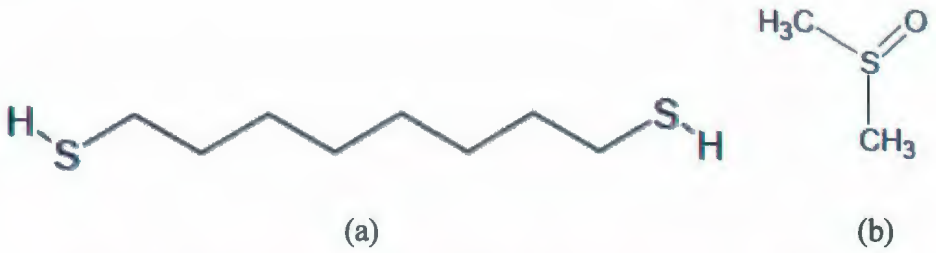

(a) (b)

Figure 4.1: Molecular structures of (a) 1,8-octanedithiol, and (b) DMSO.

The efficiency of the device could be enhanced, by incorporating a few volume percentages of addictive in the precursor used to spin-cast films comprising a low-bandgap polymer and a fullerene derivative. 1,8-octanedithiol (ODT), with its chemical structure shown in Fig. 4.1a, is an additives successfully used in P3HT:PCBM and PCPDTBT:PC71BM devices,

for which the efficiencies of the devices have been improved from 2.5% to 3.6% [116] and from 2.8% to 5.5% [43], respectively. Poly(3,4-ethylene dioxythiophene) (PEDOT) doped with poly(4-styrene sulfonate) (PSS) has been commonly used to prepare a spin-coated layer on ITO surface of OLED and OSCs in order to improve the surface quality of the ITO electrode [10,92]. However, PEDOT is limited by a low conductivity, ~2 ± 0.05 S/cm [117] and the conductivity of PEDOT obtained in the Chapter 3 is only 0.0004 S/cm. Recently, it is discovered that the conductivity of a PEDOT film can be enhanced by over 100-folds if a high dielectric solvent dimethyl sulfoxide (DMSO), is added to the PEDOT aqueous solution [118]. DMSO, with its molecular structure shown in Fig. 4.1b, is a hydrophilic polar aprotic solvent capable to dissolve P3HT, MEH-PPV, and PCBM. DMSO possesses a low toxicity, which is advantageous for the applications of photovoltaic devices in ambient atmosphere. In this study, we analyze the absorption spectra as a function of the volume percentage of the additives. The morphology and the Raman spectroscopy of the MEH-PPV:PCBM films doped with different percentages of the additive are investigated by atomic force microscopy (AFM) and Raman spectrometer, respectively. We demonstrate that the PCE increases from 2.5% to 2.8% by incorporating 1% of ODT into MEH-PPV:PCBM films. Furthermore, a large efficiency of 3.15% was obtained by doping 5% DMSO into MEH-PPV:PCBM layers, which surpasses all efficiencies reported for MEH-PPV solar cells.

4.2 Experimental details

In the experiment, MEH-PPV, purchased from American Dye Source, Inc., is first dissolved in 1,2-dichlorobenzene (DCB) to make 4 mg/ml solution, followed by blending with PCBM (Nano-C, Inc.) in 1:4 ratio. The blend solution is stirred for ~15 h at 70°C on a hot plate. ODT, purchased from Sigma-Aldrich, Inc., is added to MEH-PPV:PCBM solution with varying addictive concentration from 0 to 3 vol%. For the DMSO experiments, DMSO of varying concentrations at 5, 10, 20 and 30 vol% is incorporated into MEH-PPV:PCBM solution. Polymer solar cells are fabricated on indium-tin oxide (ITO) coated glass substrates (Delta technologies, Inc.). After spin-coating a PEDOT layer at 2000 r.p.m. for 80 s, the blend solution is spin-coated at 2000 r.p.m. for 40 s. The devices are completed upon the evaporation of an Al cathode, as shown in Fig. 4.2.

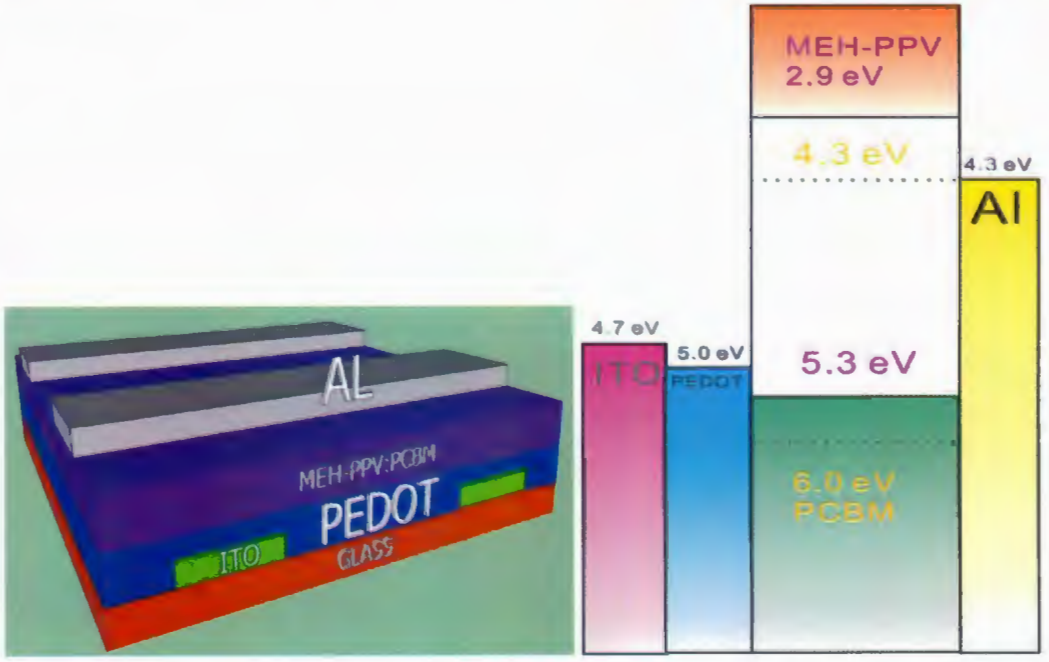

Figure 4.2: Schematic illustration and energy level diagram of a polymer solar cell with a multilayer structure of ITO/PEDOT:PSS/MEH-PPV:PCBM/Al.

Testing has been carried out in the ambient condition under AM 1.5 G irradiation (100 mW/cm^2) using a Newport Oriel 96000 solar simulator, whereas the *J-V* curve is collected by a Keithley 2420 source meter. Absorption spectra are obtained using a Cary 6000i spectrophotometer. AFM and optical microscopy images are observed in the acoustic mode of the atomic force microscopy modes of Alpha SNOM (WITec), which is a combined unit featuring a scanning near-field optical microscope, a confocal microscope, and an atomic force microscope. Raman spectra are obtained on confocal LabRAM (HORIBA Jobin Yvon). Cyclic voltammetry are measured by Epsilon-C3 (Bioanalytical Systems, Inc.)

4.3 Results and discussion

4.3.1 Octanedithiols doping for efficiency improvement

Figure 4.3 shows the UV-visible absorption spectra of MEH-PPV:PCBM films with curves representing films from solution without the ODT doping and doping concentrations of 1, 2, 2.5 and 3%, respectively. The absorbance decreases as the concentration of the ODT increases. It was reported that, as the doping concentration increases, the absorption band of the film exhibits a red shift in the P3HT:PCBM film doped with different vol % of ODT [116]. However, for the ODT doped MEH-PPV:PCBM films studied here, no red shift is evident in Fig. 4.3 as the absorbance peak is constant at ~510 nm at different ODT concentrations.

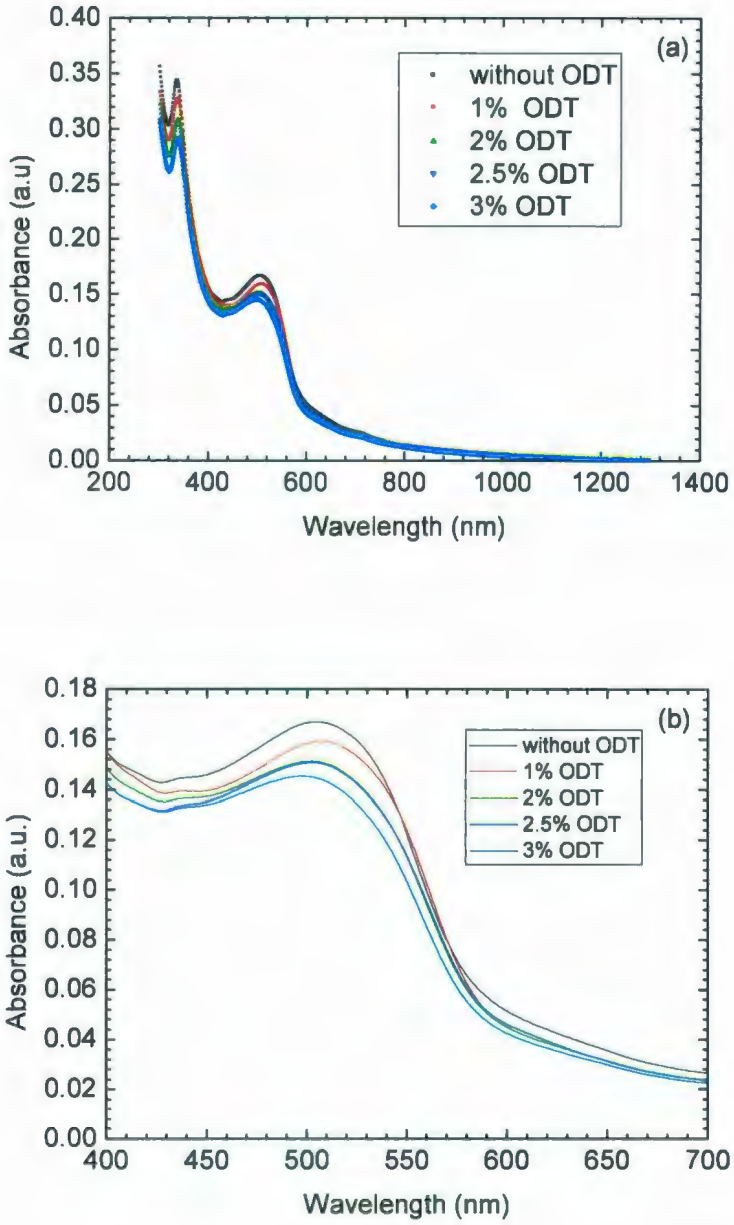

Figure 4.3: UV-visible spectra of MEH-PPV:PCBM films cast from dichlorobenzene as well as dichlorobenzene containing 1, 2, 2.5, and 3 vol % of ODT. (b) is an enlarged figure of (a) over a narrow wavelength range.

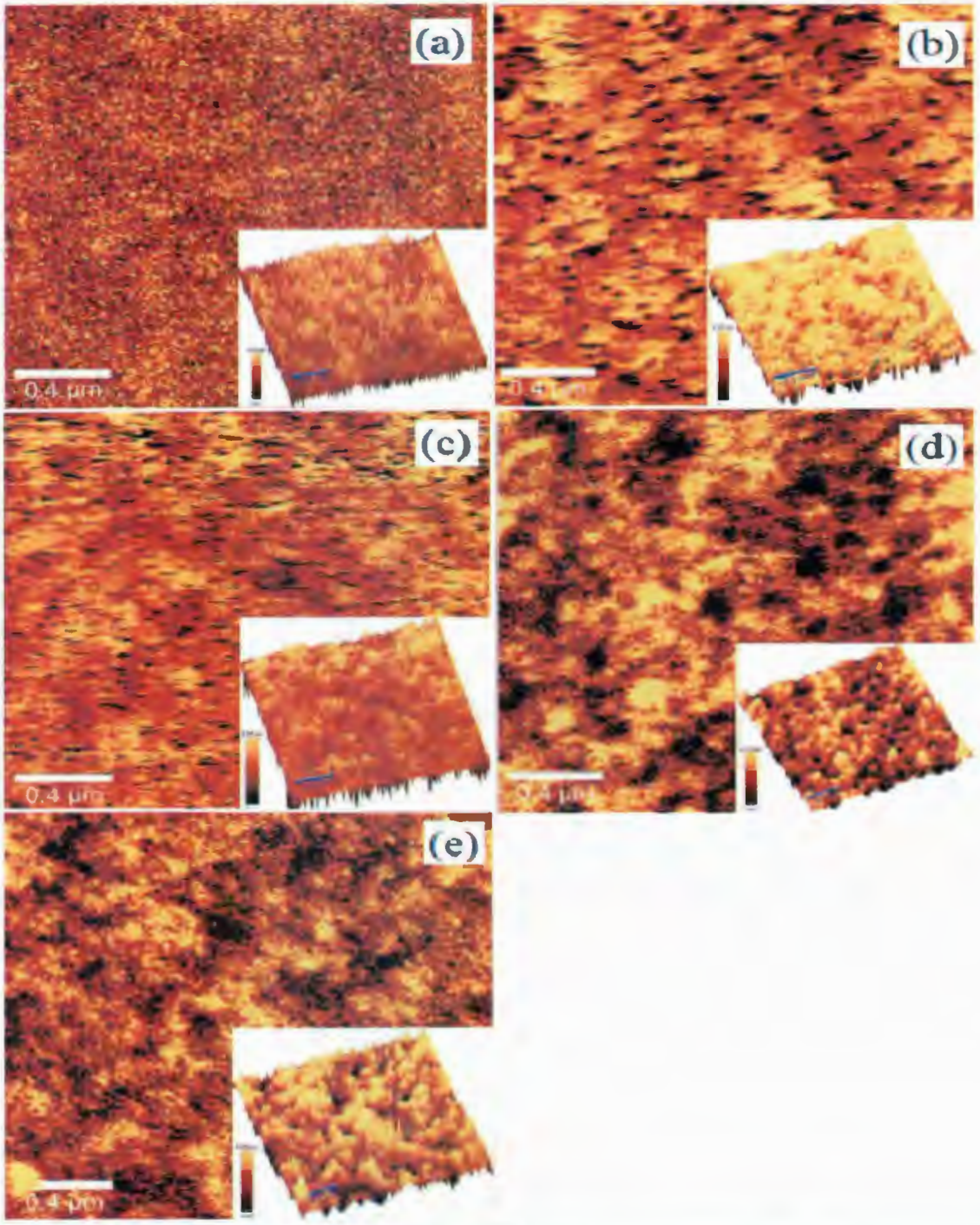

Figure 4.4: AFM images of (a) MEH-PPV:PCBM film cast from dichlorobenzene, and MEH-PPV:PCBM films cast from dichlorobenzene containing (b) 1 vol % , (c) 2 vol %, (d) 2.5 vol %, and (e) 3 vol % ODT. The insets cover exactly the same regions with the variations in height shown explicitly.

Figure 4.4 shows the surface morphology observed by AFM on MEH-PPV:PCBM films cast from DCB solvent as well as DCB doped with different ODT concentrations of 1, 2, 2.5, and 3 vol%, respectively. The root-mean-square (rms) values for the surface roughnesses of MEH-PPV:PCBM films doped with ODT are calculated and plotted in Fig. 4.5. The surface of the film with ODT doping is much rougher than that without ODT doping. As the concentration of the ODT increases from 0 to 3 vol %, the rms value increases from 1.23 to 12.31 nm.

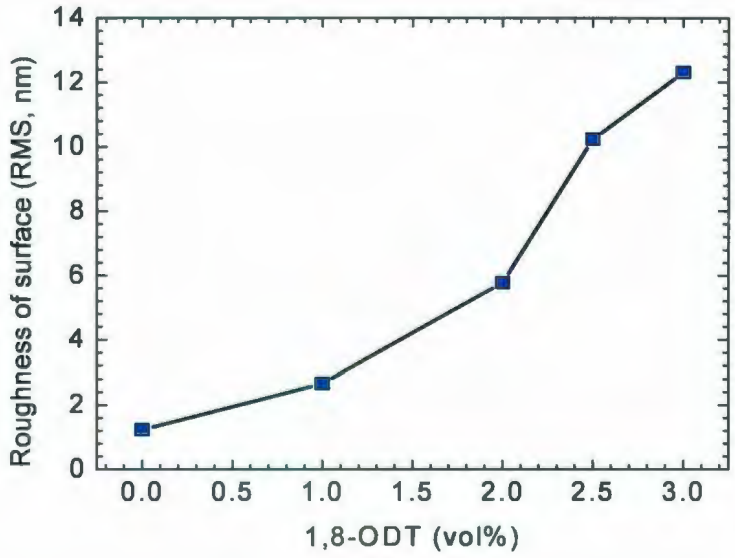

Figure 4.5: Surface roughness of the MEH-PPV:PCBM film as a function of ODT doping concentration.

J-V curves of the films doped with different volume percentages of ODT under Air Mass 1.5 (100 mW cm^{-2}) are shown in Fig. 4.6. The device without ODT doping (reference cell) shows an efficiency of 2.5%, which is close to the highest efficiency of MEH-PPV device reported so far, i.e., 2.9% [119]. When 1 vol % of ODT is doped, I_{sc} increases from 7.72 mA/cm^{-2} to 9.47 mA/cm^{-2}, corresponding a PCE value of 2.8%. Calculated from the reciprocal of the slope above

$J = 0$ on the J-V curves, the series resistances of the MEH-PPV:PCBM devices doped with different amounts of ODT are shown in Fig. 4.7. The series resistance of the device steadily increases with the increase in the amount of ODT in the MEH-PPV:PCBM layer.

The photovoltaic performance of MEH-PPV:PCBM solar cells fabricated by doping various volume percentages of ODT is shown in Fig. 4.8. The BHJ solar cells doped with ODT exhibit enhanced I_{sc} and PCE, while, V_{oc} and FF remain constant. Since V_{oc} is basically determined by the energy difference between the highest occupied molecular orbital of the polymer donor and the lowest unoccupied molecular orbital of the fullerene (Eqn. 4.1), it is reasonable to see that V_{oc} remain constant as the donor and acceptor materials in this study are MEH-PPV and PCBM, respectively. Compared with the reference cell, I_{sc} values of the devices with ODT doping increase in the concentration range studied here. Analysis based on the surface roughness (Fig. 4.5) and the absorption spectra (Fig. 4.3) indicates that the roughness of the MEH-PPV:PCBM layer is proportional to the volume percentage of the doping ODT, while the absorbance is inversely proportional to the volume percentage of the doping ODT. Since I_{sc} is closely related with the surface morphology of the active layer and the absorption, as a compromise to achieve both high device efficiency and maximal photon absorption, the highest I_{sc} and PCE occur at the ODT doping concentration of ~1 vol %.

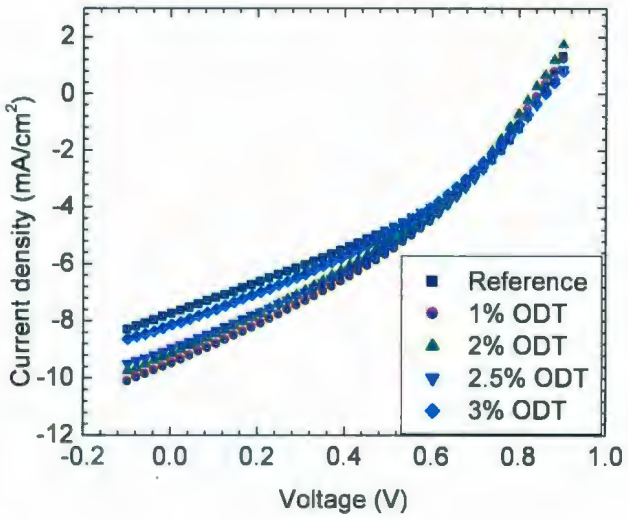

Figure 4.6: *J-V* curves of MEH-PPV:PCBM solar cells doped with different volume percentages of ODT.

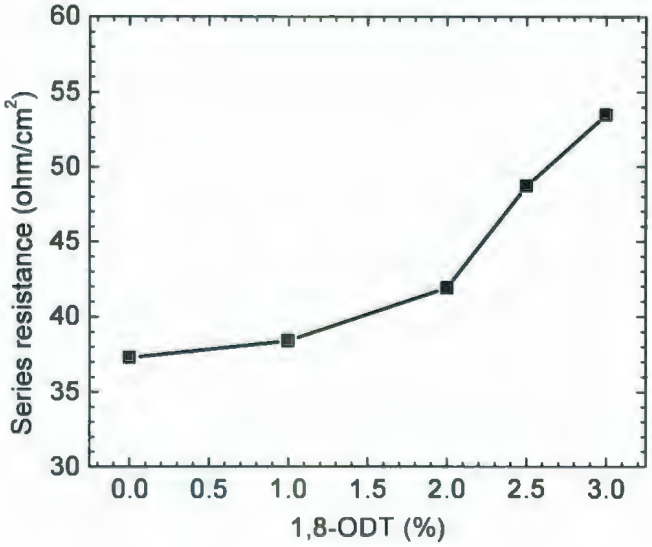

Figure 4.7: Series resistances of MEH-PPV:PCBM solar cells doped with different volume percentages of ODT.

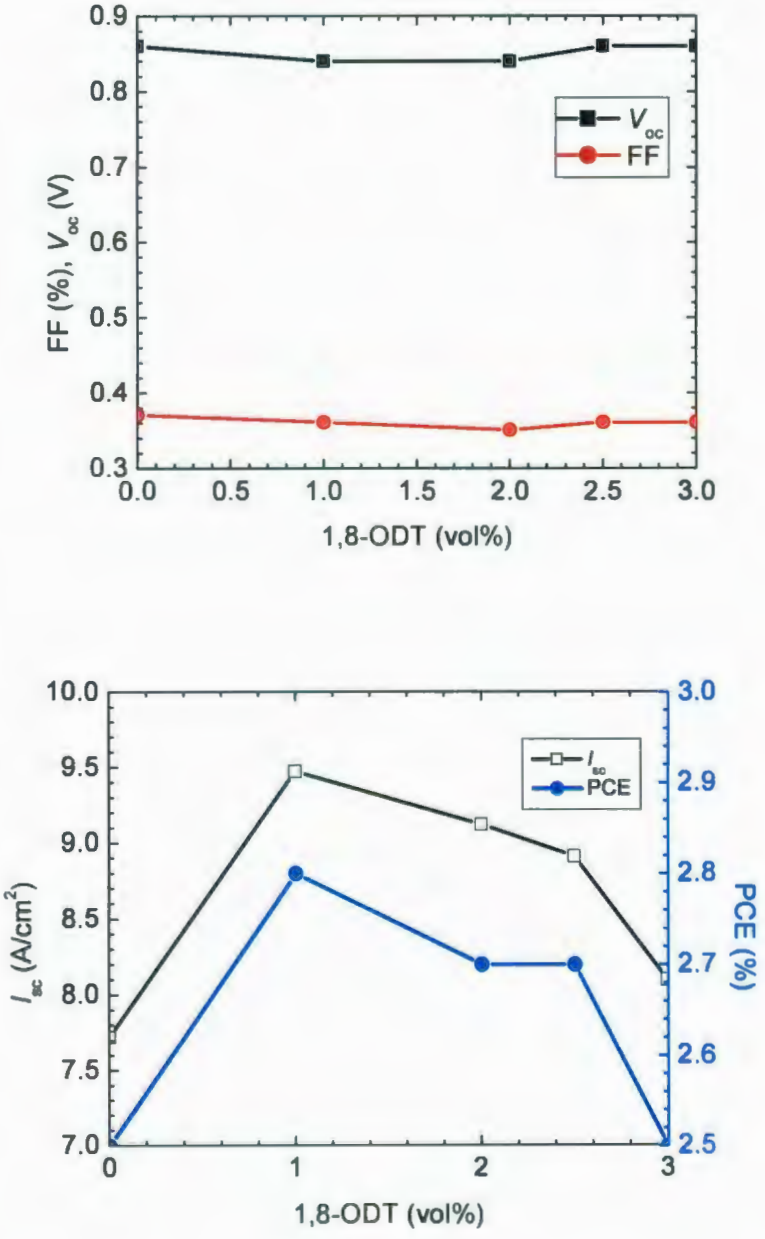

Figure 4.8: Photovoltaic performance of MEH-PPV:PCBM solar cells doped with different volume percentages of ODT.

4.3.2 Dimethyl sulfoxide (DMSO) for efficiency improvement

The UV-visible absorption spectra of a MEH-PPV:PCBM film cast from DCB solvent as well as films cast from DCB solvent doped with DMSO at volume percentages of 5, 10, 20, and 30 vol % are shown in Fig. 4.9. Since DMSO is a transparent solvent, it is reasonable to observe the decrease in the absorbance as the DMSO doping concentration increases, which is evident from Fig. 4.9.

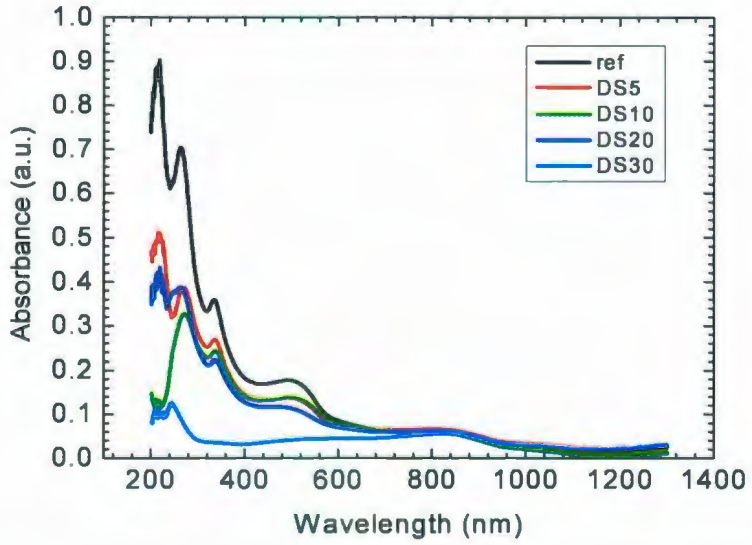

Figure 4.9: UV-visible spectra of MEH-PPV:PCBM films cast from dichlorobenzene solvent (reference), and MEH-PPV:PCBM films cast from dichlorobenzene doped with DMSO of different volume percentages at 5 (DS5), 10 (DS10), 20 (DS20), and 30 vol % (DS 30).

Figure 4.10 shows the optical micrographs of MEH-PPV:PCBM films cast from DCB solvent, and films cast from DCB doped with DMSO of different volume percentages at 5, 10, 20 and 30 vol %. Since MEH-PPV is insoluble in DMSO, as the DMSO amount increases, the film quality deteriorates. The rms roughnesses of the MEH-PPV:PCBM films doped with DMSO

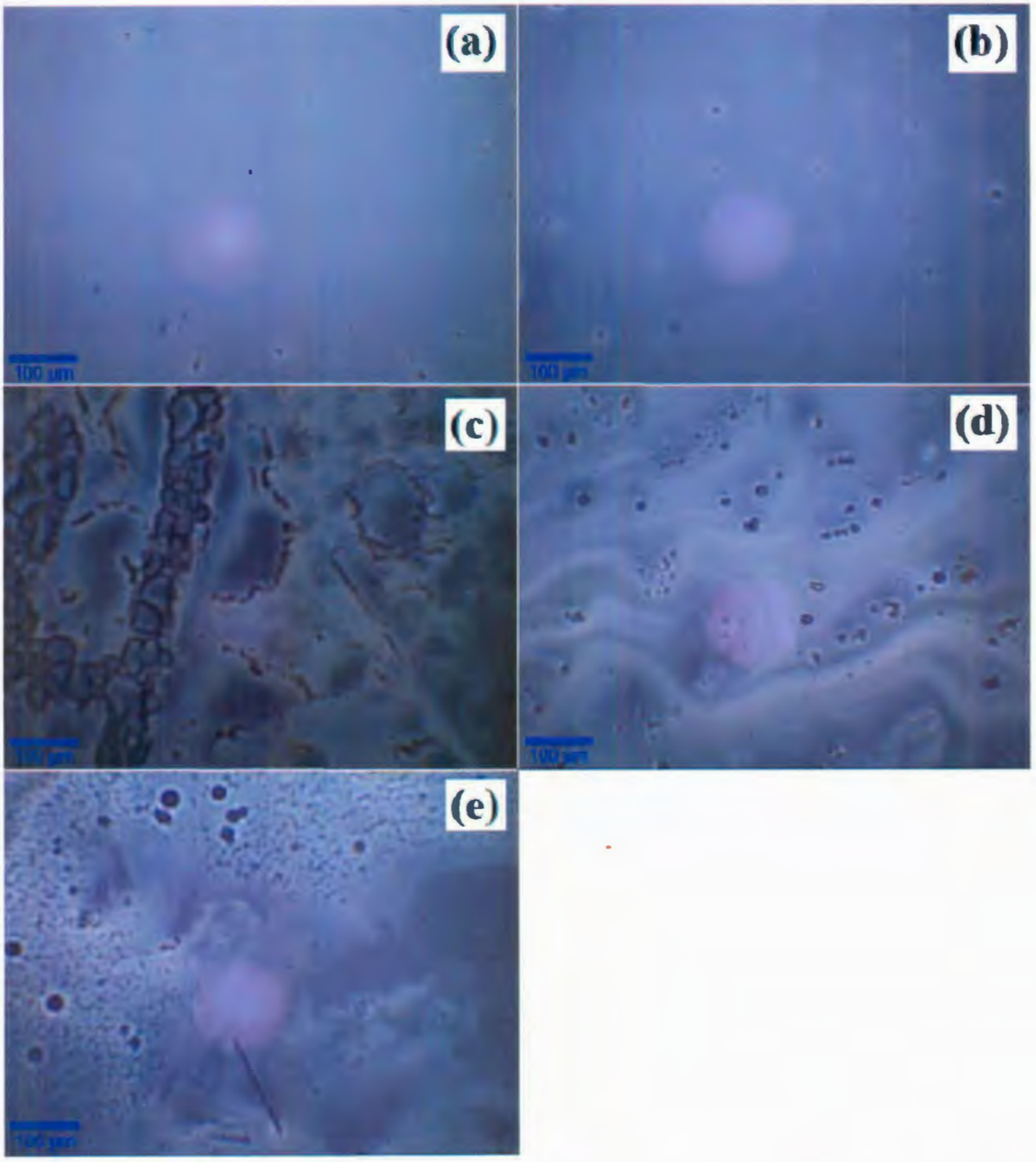

Figure 4.10: Optical micrographs of (a) a MEH-PPV:PCBM film cast from DCB solvent, and MEH-PPV:PCBM films cast from DCB doped with DMSO of concentrations at (b) 5, (c) 10, (d) 20, and (e) 30 vol %.

are calculated from the AFM images of Fig. 4.11. As the concentration of DMSO increases from 0 to 5 vol %, the surface roughness increases from 2.94 to 3.23 nm accordingly. However, when the DMSO doping concentration is increased further, the roughness is hard to measure by AFM as the quality of the film is not satisfactory, which is evident from (c), (d), and (e) in Fig. 4.10.

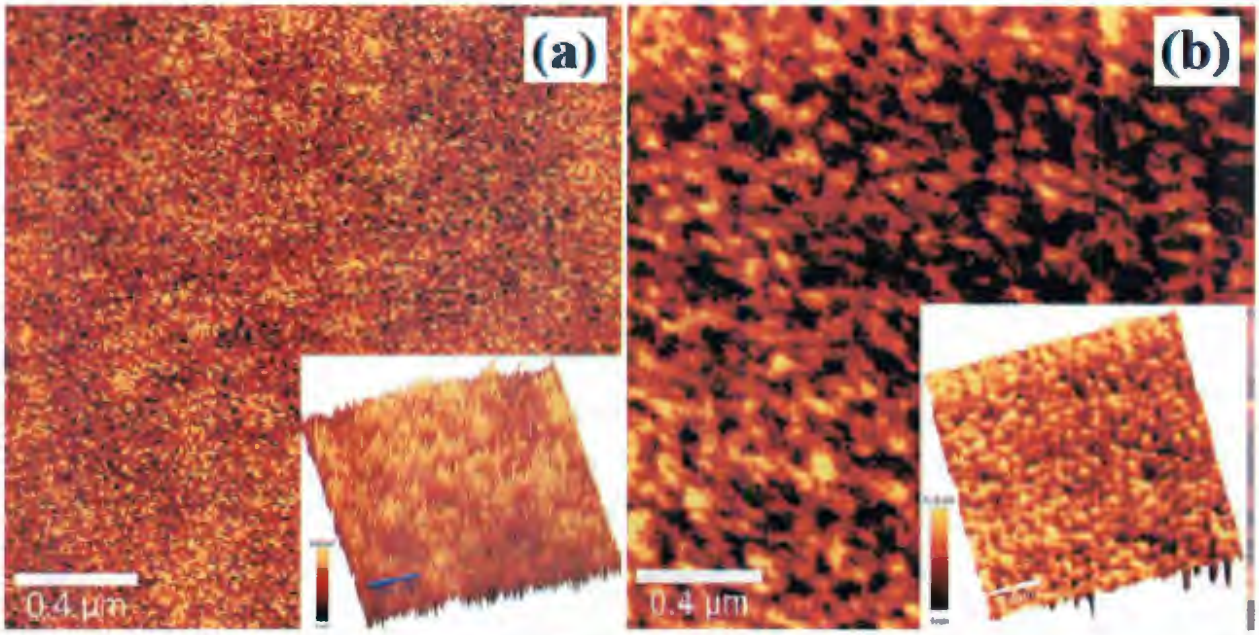

Figure 4.11: AFM morphology of (a) a MEH-PPV:PCBM film cast from DCB solvent (reference) and (b) a MEH-PPV:PCBM film cast from DCB doped with DMSO of 5 vol %.

Figure 4.12 shows the *J-V* curves of a MEH-PPV:PCBM films cast from DCB solvent (D0), and MEH-PPV:PCBM films cast from DCB doped with DMSO of 5 vol % (D5), 10 vol % (D10), 20 vol % (D20), and 30 vol % (D30). From the slopes of the curves of D0, D5, and D10, it is evident that the series resistance R_s (inverse slope above $J = 0$) decreases as the doping concentration increases from 5 to 10 vol %. Starting from a series resistance of 27.53 Ω/cm^2 for D0, after increasing the DMSO concentration to 5 and 10 vol%, the series resistance decreases to 19.62 and 10.32 Ω/cm^2, respectively. Since the film quality of the MEH-PPV:PCBM films

doped with either 20 vol % or 30 vol % of DMSO is low, as shown in (d) and (e) of Fig. 4.10, their series resistances are not compared with those values for the cases of low DMSO dopings. Nevertheless, the series resistance decreases from D20 to D30 due to the increase of the DMSO concentration. The photovoltaic performance of the solar cells fabricated by incorporating various amounts of DMSO is shown in Fig. 4.13. The BHJ solar cells doped with 5 vol % of DMSO exhibits enhanced I_{sc}, FF, and V_{oc}, corresponding to a higher PCE of ~3.15% from 1.75% for the film without DMSO doping. However, when the DMSO concentration is further increased to 10, 20, and 30 vol %, the performance of the devices degrades rapidly. From the observed morphologies of the film, it can be found that the performance of the device is closely related with the morphology of the film, i.e., reasonably increased surface roughness enhances the efficiency of the device. However, if the roughness is too large, the photovoltaic performance decreases due to the deteriorated film quality.

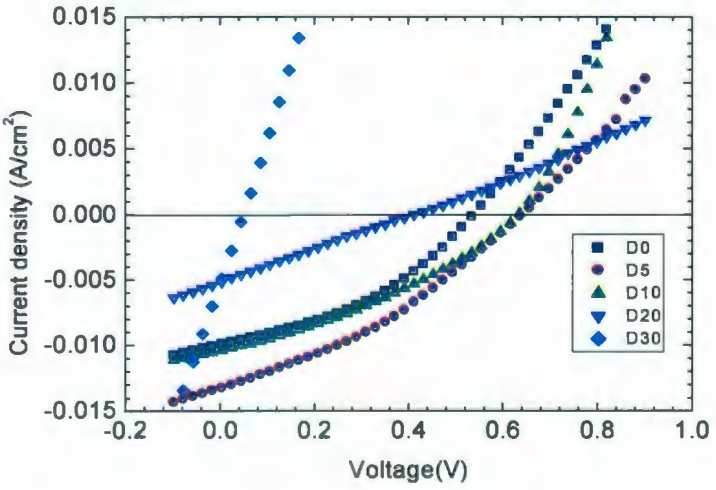

Figure 4.12: *J-V* characteristics of a MEH-PPV:PCBM film cast from DCB (D0), and MEH-PPV:PCBM films cast from DCB with different DMSO doping concentrations of 5 (D5), 10 (D10), 20 (D20), and 30 vol% (D30).

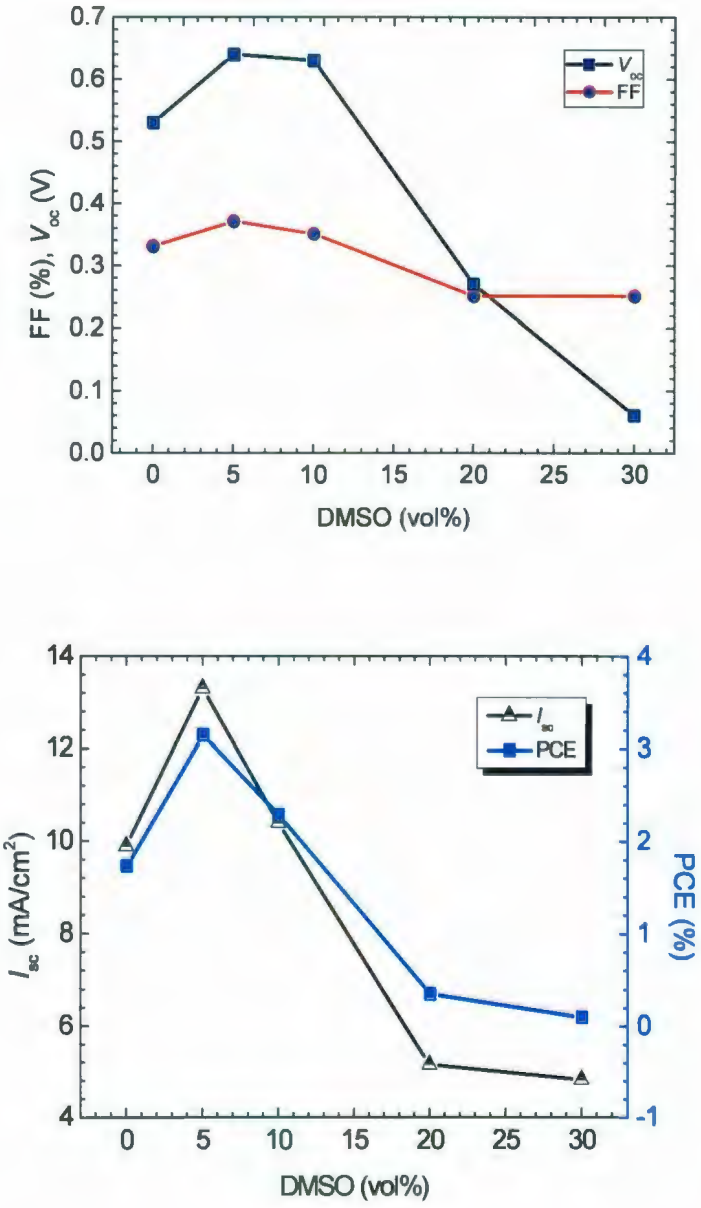

Figure 4.13: Photovoltaic performance of a MEH-PPV:PCBM film cast from DCB, and MEH-PPV:PCBM films cast from DCB with different DMSO doping concentrations of 5, 10, 20, and 30 vol %.

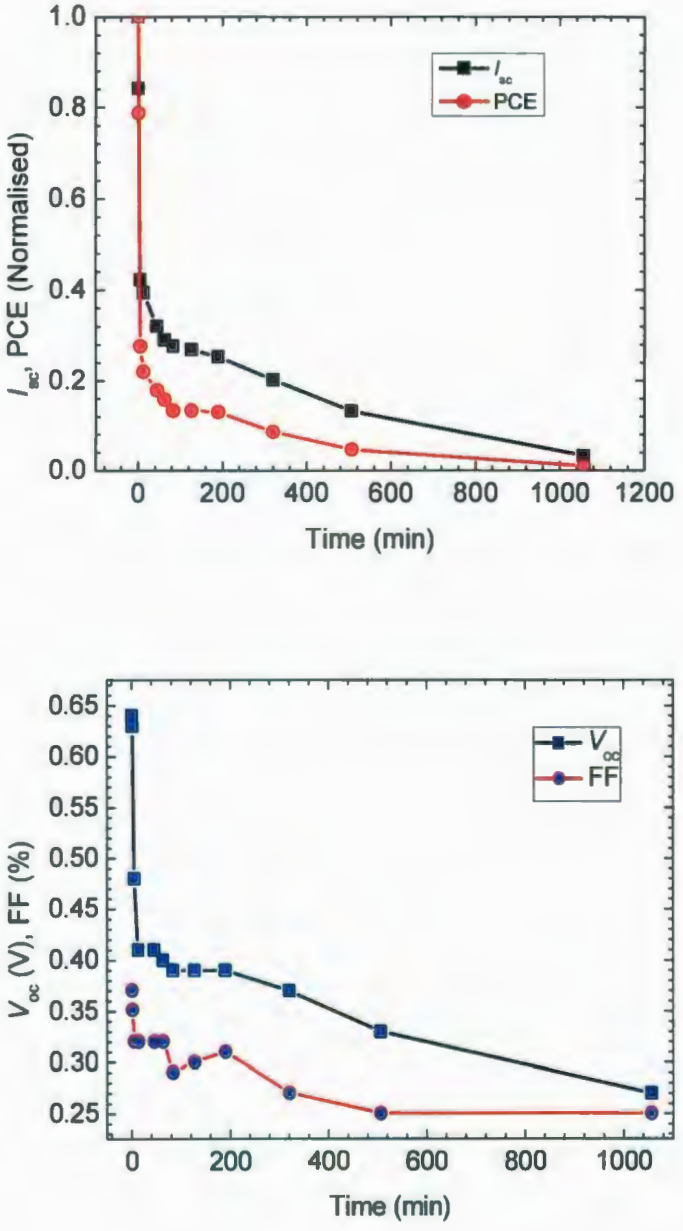

Figure 4.14: Normalized decay in the photovoltaic performance of a MEH-PPV:PCBM cell processed with 5 vol% DMSO in ambient environment.

The degradation of the MEH-PPV:PCBM solar cells doped with 5 vol % of DMSO in ambient enviroment is shown in Fig. 4.14, which exhibits a short lifetime of the devices as the efficiency is only 20% of its initial efficiency in 100 min after the device fabrication. The lifetime of the half maximum in efficiency is ~20 min. However, compared with the degradation of MEH-PPV solar cells (Fig. 4.15), the lifetime of MEH-PPV:PCBM solar cell without DMSO (~75 min) is longer than that of the MEH-PPV:PCBM solar cell processed with DMSO.

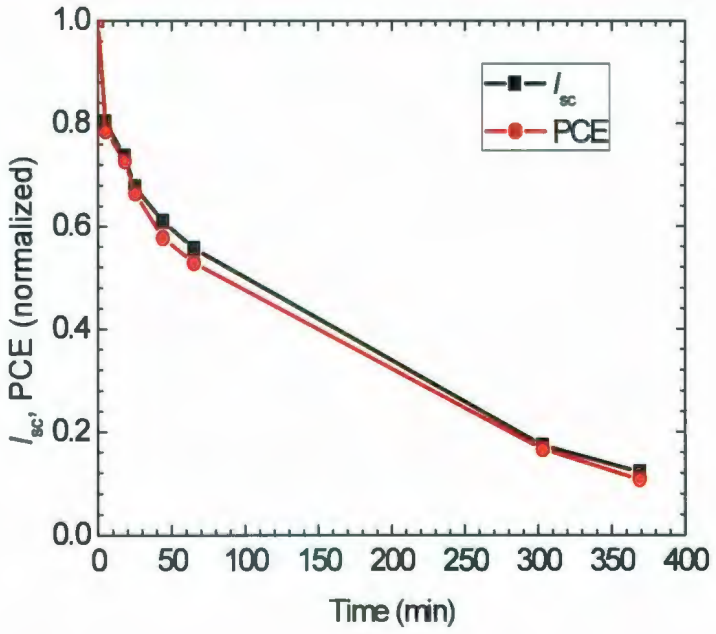

Figure 4.15: Normalized decay in photovoltaic performance of a MEH-PPV:PCBM solar cell without DMSO doping in ambient environment.

The mechanism for the degradation in the efficiency of MEH-PPV devices over time is complicated. Change in the series resistance may be one reason as the efficiency of the device is inversely proportional to the series resistance of the device [120]. Fig. 4.16 shows that, it takes

370 min for the series resistance of the MEH-PPV:PCBM solar cells to increase from 38.8 to 429 Ω/cm^2, in contrast to 1060 min that is needed for the R_s of the MEH-PPV:PCBM solar cells processed with 5 vol% DMSO to increase from 18 to 492 Ω/cm^2. The detail of the degradation mechanisms is still under investigation.

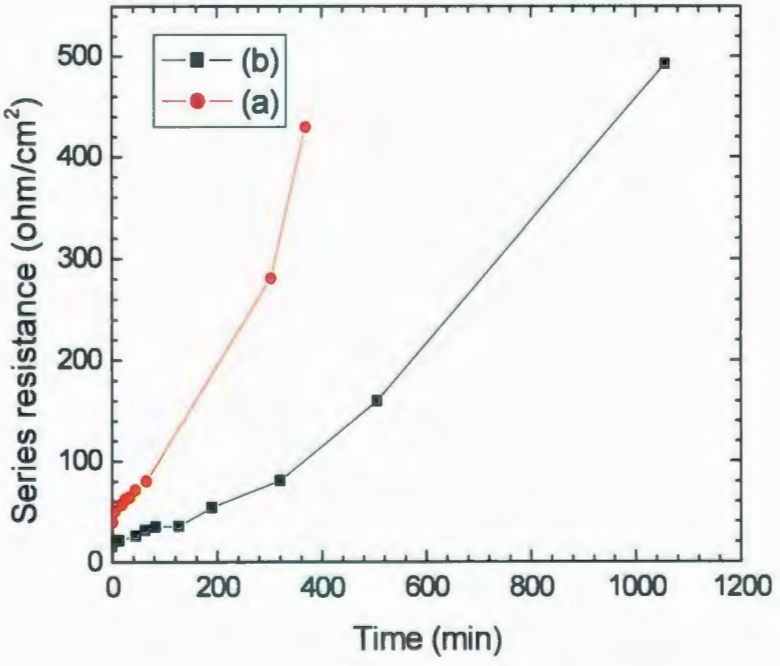

Figure 4.16: (a) Series resistances of a MEH-PPV:PCBM solar cell and (b) a MEH-PPV:PCBM cell processed with 5 vol% DMSO, in ambient environment as a function of time.

In order to investigate the origin of the improved efficiency induced by DMSO doping, scanning electron microscopy (SEM) has been used to examine the morphologies of the DMSO-treated and untreated MEH-PPV:PCBM layers, SEM images of single droplets of untreated, 5 and 10 vol% DMSO treated MEH-PPV:PCBM, deposited on a PEDOT film are shown in Figs. 4.17, 4.18, and 4.19, respectively.

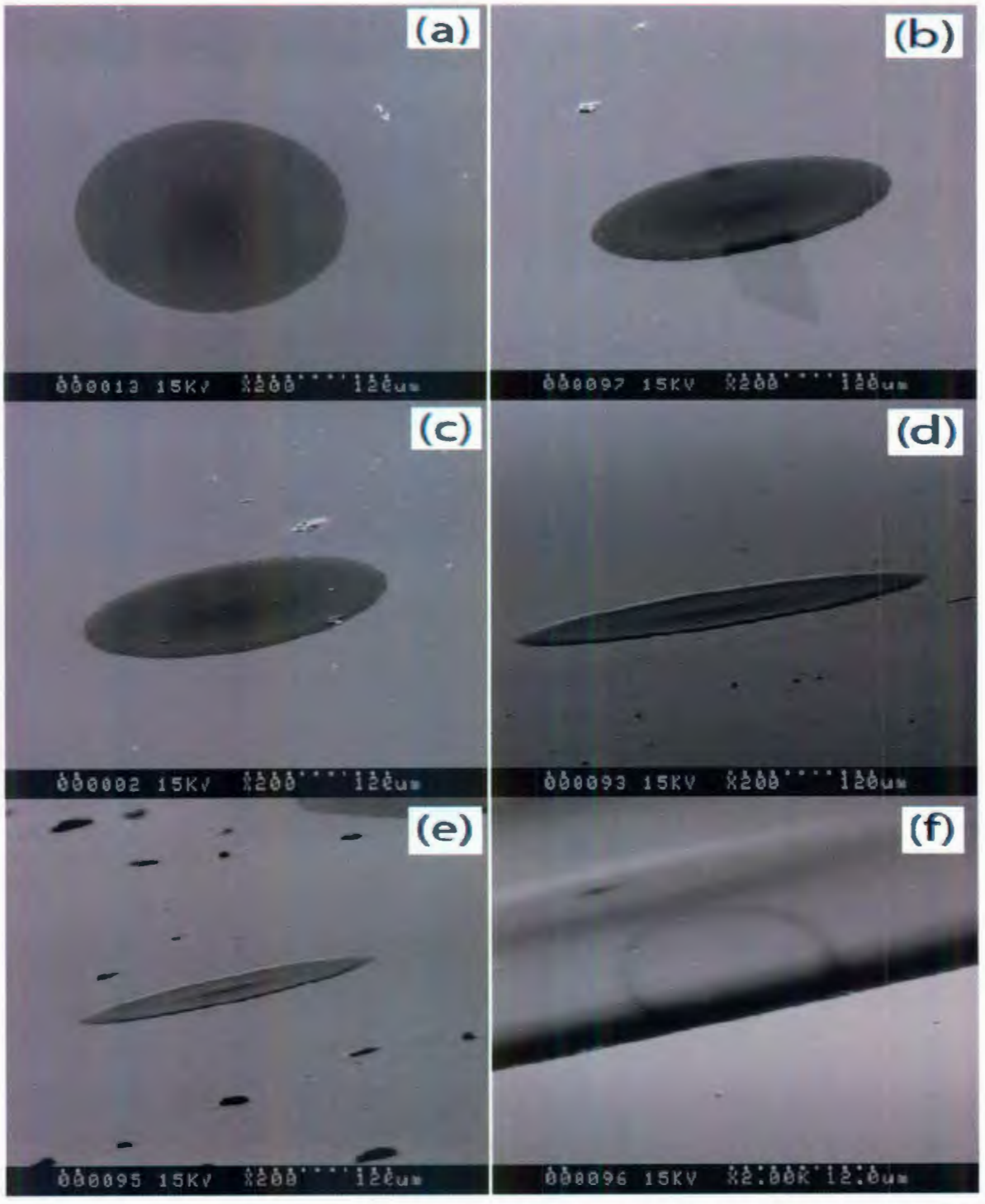

Figure 4.17: SEM images of the MEH-PPV:PCBM droplet on the PEDOT film, observed at (a) 75°, (b) 45°, (c) 15°, (d, e) 0° above the horizontal direction, and side view with a magnification of 2000 times (f).

The untreated MEH-PPV:PCBM droplet exhibits a crater-like shape (Fig. 4.17), which might be caused by "coffee stain effect" [94]. Specifically, solvent evaporation at the edge of the film is faster than that in the center region, resulting in different rates of volume changes in the central and edge regions of the MEH-PPV:PCBM droplet, therefore there is a net flow from the center to the edge of the droplet. As a comparison, in the case of the 5 vol% DMSO-treated MEH-PPV:PCBM droplet, a flat film is observed (Fig. 4.18), which may be due to a decrease in

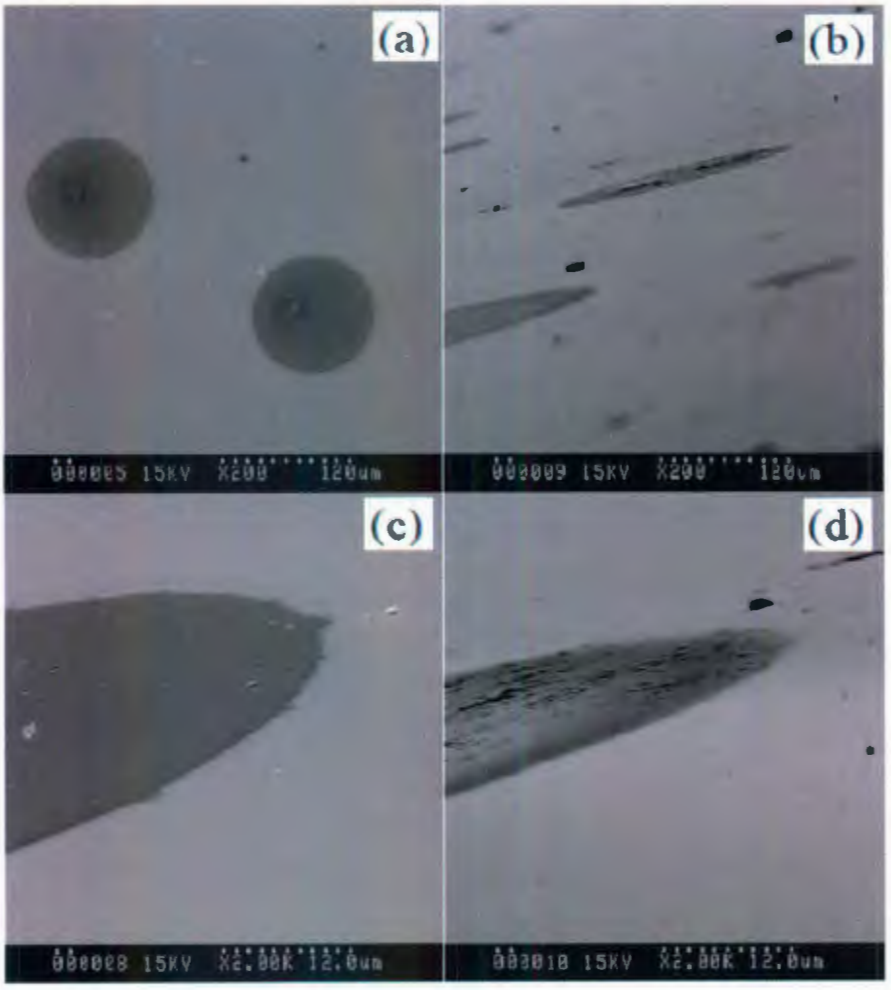

Figure 4.18: SEM images of the 5 vol% DMSO doped MEH-PPV:PCBM droplet on the PEDOT film, observed at (a) 90°, (b) 15° above the horizontal direction, and side views with a magnification of 2000 times (c, d).

the evaporation rate caused by the addition of DMSO of a high boiling point (189°C). A reduced evaporation rate is expected to decrease the net flow in the droplet. However, when 10 vol % of DMSO is doped into MEH-PPV:PCBM film, the quality of the film becomes worse with many insoluble DMSO spots on the MEH-PPV:PCBM droplet, as shown in Fig. 4.19.

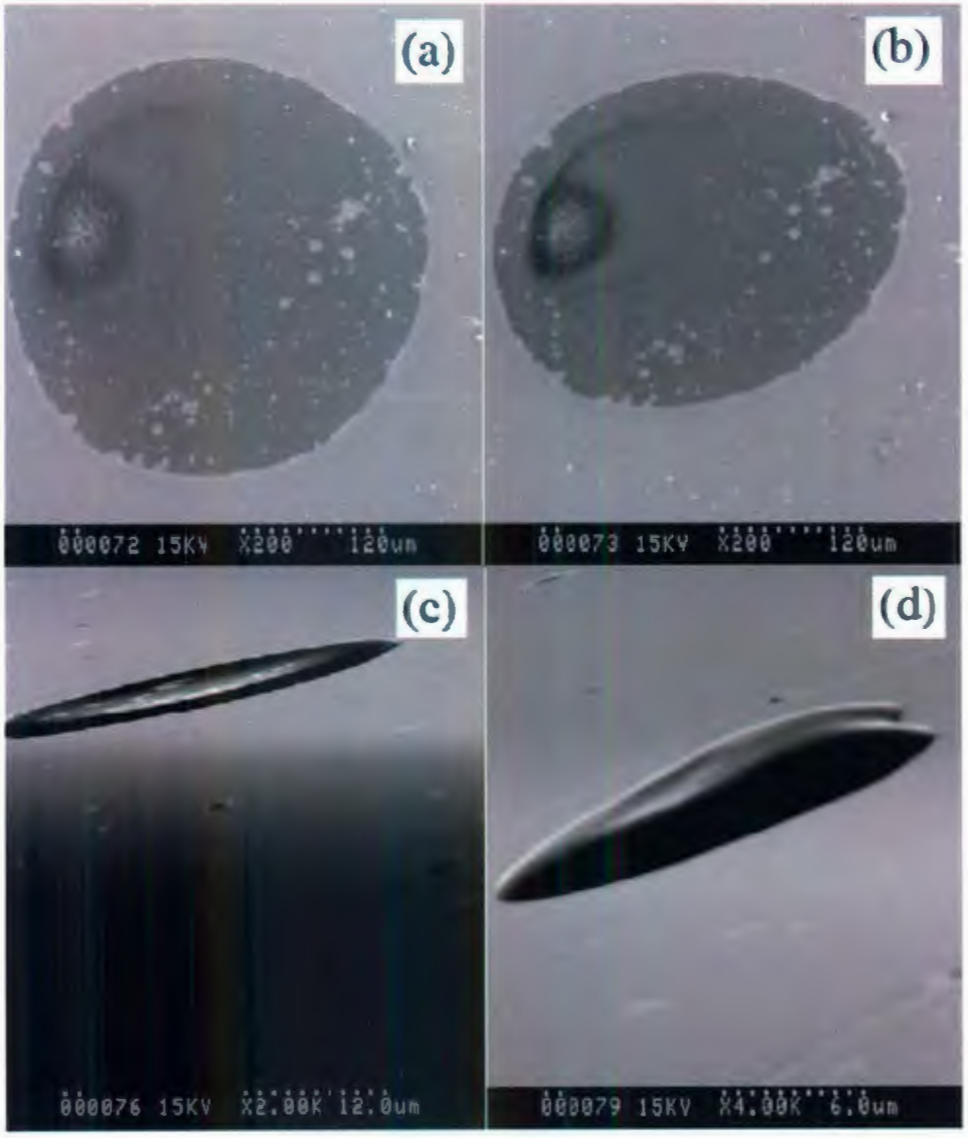

Figure 4.19: SEM images of the 10 vol% DMSO doped MEH-PPV:PCBM droplet on the PEDOT film, observed at (a) 90°, (b) 75° above the horizontal direction, and side views with magnifications of 2000 times (c) and 4000 times (d).

In addition, SEM images of the evaporated Al films on untreated, 5 and 10 vol% DMSO treated MEH-PPV:PCBM are shown in Figs. 4.20, 4.21, and 4.22, respectively. The untreated MEH-PPV:PCBM film presents a rough, irregular edge on Al film, and some air gaps between the electrode and the MEH-PPV:PCBM film. In contrast, the 5 and 10 vol% DMSO treated MEH-PPV:PCBM has improved interfacial stability, resulting in a smooth, uniform edge and no air gap in the contact region, as evident in Figs. 4.21 and 4.22, respectively.

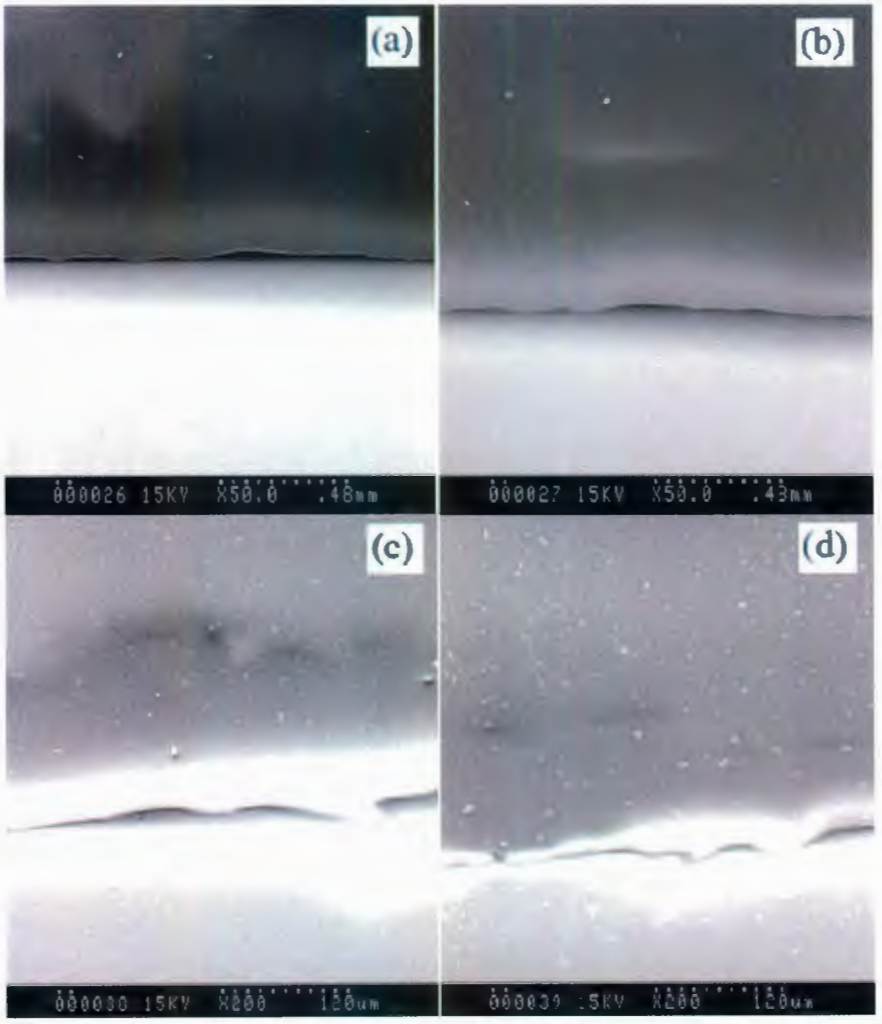

Figure 4.20: SEM images of the MEH-PPV:PCBM droplet on the Al film, observed at magnifications of 50 times (a, b) and 200 times (c, d).

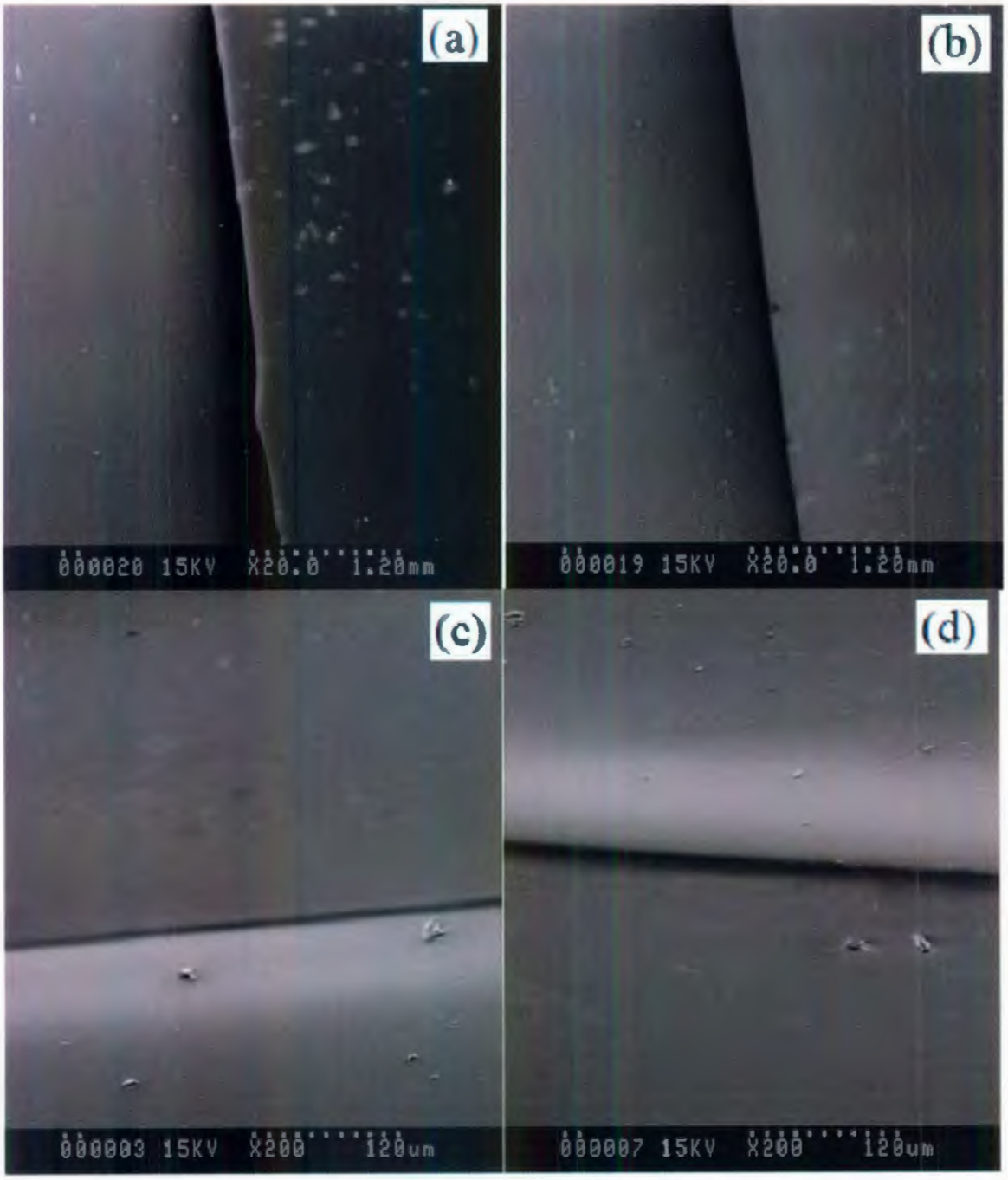

Figure 4.21: SEM images of 5 vol% DMSO doped MEH-PPV:PCBM droplet on the Al film, observed at magnifications of 20 times (a, b) and 200 times (c, d).

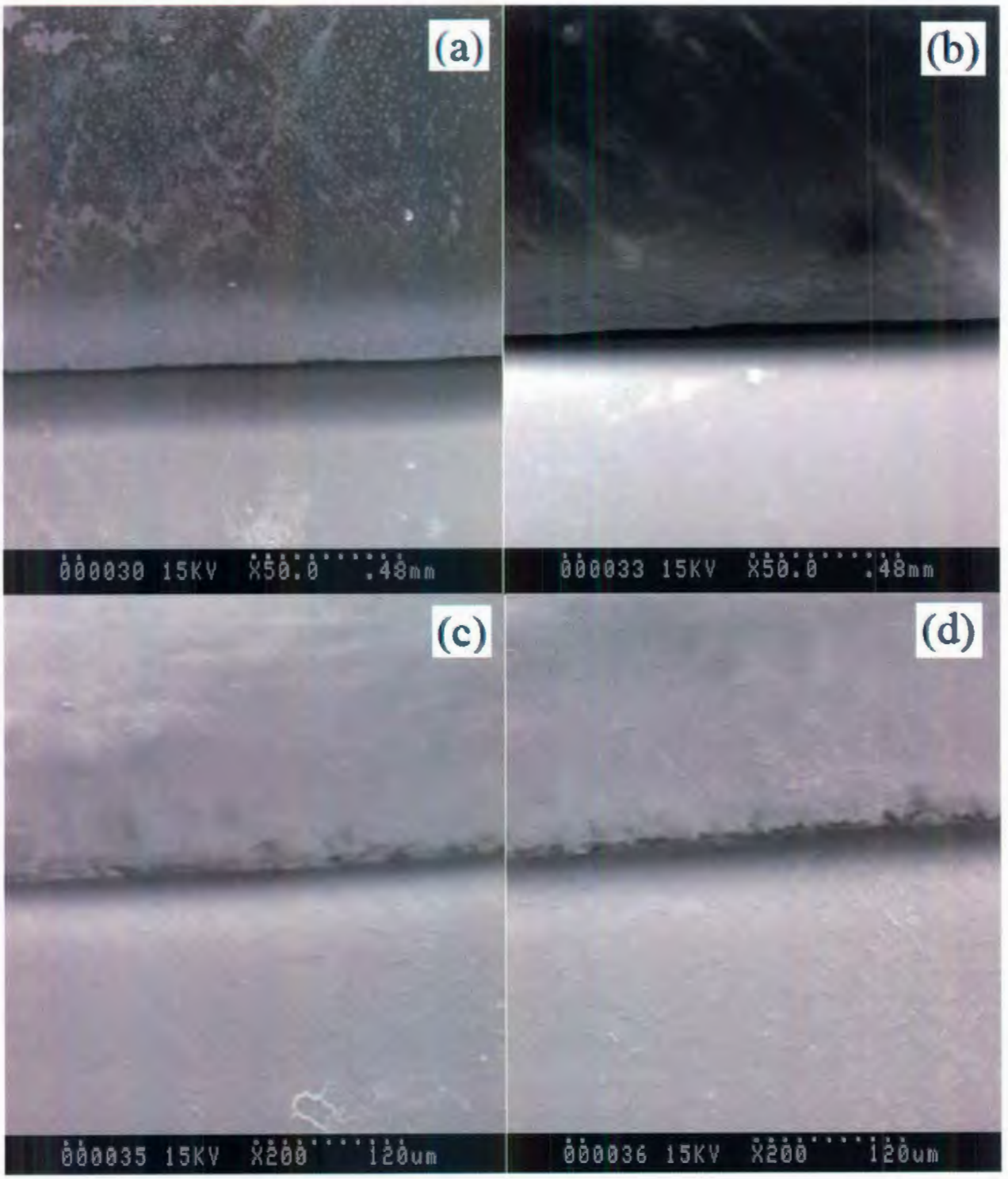

Figure 4.22: SEM images of 10 vol% DMSO doped MEH-PPV:PCBM droplet on the Al film, observed at magnifications of 50 times (a, b) and 200 times (c, d).

The effects of DMSO additives on the electrochemical behaviours of MEH-PPV:PCBM films have been studied by cyclic voltammetry (CV) in 0.1 M tetrabutylammonium tetrafluoroborate (TBATFB) acetonitrile solution as illustrated in Chapter 2. Figures 4.23 and 4.24 show the CV results for the ITO, DMSO treated and untreated MEH-PPV:PCBM films at scan rates of 50 and 100 mV/s, respectively. It is evident that the current density integrated over the potential range is almost doubled after treated with 10 vol% DMSO at these scan rates. Four reduction peaks and one oxidation peak can be found on the MEH-PPV:PCBM films with 5 and 10 vol% of DMSO doping concentrations. However, as the DMSO amount is increased to 5 and 10 vol%, the current density of the reduction peak increases, while, only the current density of the oxidation peak for the 10 vol% DMSO doped MEH-PPV films exhibits pronounce increase.

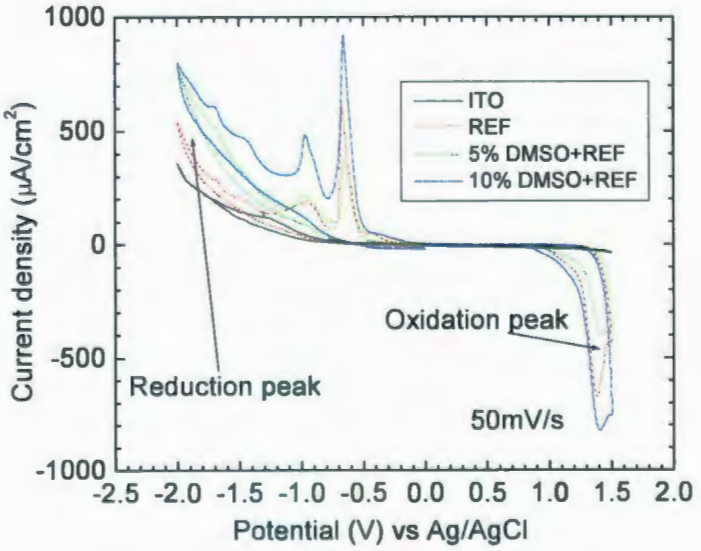

Figure 4.23: Cyclic voltammogram of ITO, MEH-PPV:PCBM, 5 and 10 vol% DMSO doped MEH-PPV:PCBM films. Scan rate: 50 mV/s.

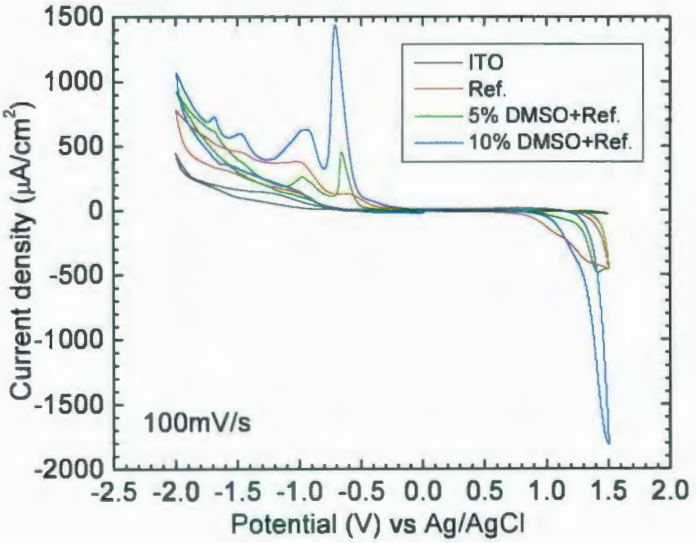

Figure 4.24: Cyclic voltammogram of ITO, MEH-PPV:PCBM, 5 and 10 vol% DMSO doped MEH-PPV:PCBM films. Scan rate: 100 mV/s.

4.4 Conclusions

Photovoltaic performance of MEH-PPV:PCBM solar cells doped with different amounts of ODT and DMSO has been studied. The morphology observation and the absorption spectra indicate that the surface roughness increases within certain doping levels as the concentrations of the addictives increases, whereas the absorbance decreases. The change in the surface roughness corresponds to a change in the efficiency of the device with an increase from 2.5% to 2.82% after doping with 1 vol % of ODT, equivalent to a ~15% improvement. In contrast, the efficiency of the MEH-PPV:PCBM solar cell doped with 5 vol % of DMSO rises to 3.15% from 1.75%,

exhibiting a ~80% enhancement. However, the lifetime of the half maximum in the efficiency of the device doped with 5 vol % of DMSO in ambient is reduced to 20 min from 75 min for a reference cell without DMSO doping, a larger series resistance in the device doped with 5% DMSO may be one reason for that. The detail of the degradation mechanisms is still under investigated.

or PET (P7) substrate. ITO or FTO on glass substrates are selectively patterned by a femtosecond laser and subsequently cleaned with de-ionized water. Patterned ITO or FTO on glass substrate is then undergone final cleaning in acetone and alcohol by ultrasonic bath for 30 min each. In order to avoid thermal shrinkage of the plastic substrates, the cleaned PET substrates are dried at room temperature. ITO or FTO on glass substrates is dried on the hot plate at ~90°C for 30 min. The PH510 or PH750 film is prepared by spin-coating on cleaned PET or glass at a speed of 3000 r.p.m. for 80 s, and then the sample is allowed to dry under gentle air flow for 10 mins to obtain relatively thick film with lower sheet resistance. Subsequently, PEDOT PVP Al 4083 is spin-coated (4000 r.p.m.) on the dried PH510 as a buffer layer. The P3HT powder or flake is first dissolved in 1, 2-dichlorobenzene (DCB) to prepare 10 mg/ml solution, followed by blending with PCBM at 1:0.8 ratio. Then, the blend is stirred for ~24 h at 40°C on the hot plate. The active layer is obtained by spin-coating the blend at 800 r.p.m. for 40 s, followed by drying in a covered glass petri dish on the hot plate at 70 °C for 10 min. Aluminum cathode is deposited by thermal evaporation. *J-V* curves are measured with a Keithley 2420 source meter under simulated AM 1.5G irradiation (100 mW cm^{-2}) using a xenon-lamp-based solar simulator (Newport Oriel 96000 150W solar simulator). Since the typical active area of an OSC is 0.09 - 0.15 cm^2 [23,10,12,46], which is too small for bending test, the active area of the OSC needs to be enlarged in order to measure the relationship between the bending angle and the performance of OSCs. Here, OSCs with six active areas of 0.12, 0.25, 0.5, 0.75, 1.0, and 1.25 cm^2 are fabricated and tested.

Surface sheet resistance is determined from four point probe measurement, as described in the Chapter 3. Transmission spectra are measured by Cary 6000i spectrophotometer (Varian Inc.).

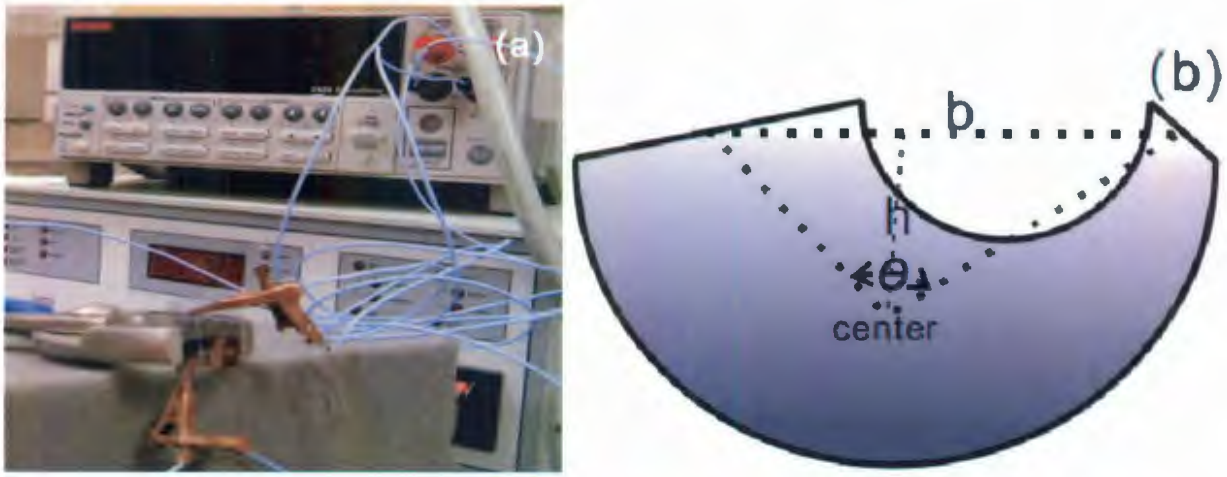

Figure 5.1: Bending angle measurement: (a), experimental setup, and (b) geometry definition.

As shown in Fig. 5.1(a), a home-built system is used to measure the relationship between the bending angle and the performance of the OSCs. The bending angle θ is defined by

$$\theta = 2\tan^{-1}(\frac{b}{2h}) \tag{5.1}$$

where b is the opening between the jaws of the substrate, and h is the height of the bending solar cells, as illustrated in Fig.5.1b.

5.3 Results and discussion

In order to maximize the number of photons arriving at the active layer, both the anode and substrate need to be highly transparent. Figure 5.2(a) shows the optical transmittances of the PET and glass substrate, which indicate that the transmittance of PET (90%) from 300 to 1300 nm is lower than that for the glass substrate (94%) as a reference. The transmittance spectra of PH510, PH750, FTO and ITO are shown in Fig. 5.2(b). The relationship between these transmittances is complicated; which is hard to tell which anode has a greater transmittance over

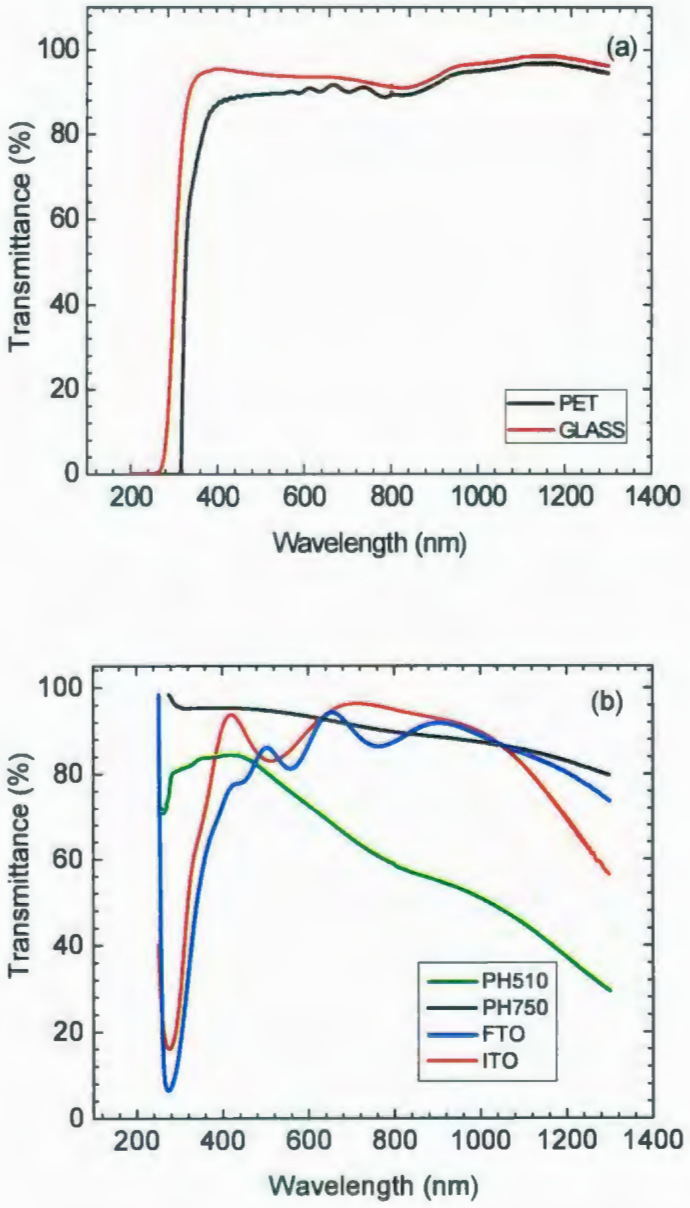

Figure 5.2: Transmission spectra of (a) PET film and glass substrate, and (b) PH510, PH750, FTO and ITO anodes.

the wavelength range from 200 to 1300 nm. In order to match with the solar spectra (AM1.5G) with the peaks mainly in the range of 400 – 700 nm, PH750 exhibits the highest transmittance,

followed by ITO, FTO, and PH510 in the order of decreasing integrated transmittance over the wavelength range. Lower transmittance means fewer photons can arrive at the active layer, which may result in a lower efficiency of the OSC.

In order to reveal the relationship between the efficiency of the OSCs, the transmittances of anodes on the substrates need to be measured, which are shown in Fig. 5.3 for PH750 on glass (G7), FTO on glass (GF), PH510 on glass (G5), ITO on glass (GI), PH510 on PET (P5), and PH750 on PET (P7). A comparison of these anode/substrate systems over the range of 400 - 700 nm indicates that the transmittances of these anode/substrates exhibit the highest transmittance for G7, followed by P7, GF, and GI in the order of decreasing transmittance. However, GF and GI show a higher transmittance than G7 in the range of 600 – 700 nm as well as a higher transmittance than P7 over the whole wavelength range (200 – 1300 nm). The transmittance of ITO on glass (GI) is higher than that of FTO on glass (GF). Although G5 exhibits higher transmittance at short wavelengths (300 – 350 nm) than other anode/substrate systems except GI, the transmittance of G5 is still low over the whole wavelength range (200 – 1300 nm), especially for the infrared range (800 – 1300 nm). The lowest transmittance is obtained by P5 in the wavelength range of 400 – 700 nm, although the transmittance of P5 is higher than that of G5 at infrared wavelengths.

To compare the conductivities of ITO, FTO, PH750, and PH510 anodes, the current-voltage (*I-V*) characteristics of each of these films on a glass substrate are shown in Fig. 5.4. The sheet resistance of a 120 nm thick ITO film is 10.11 Ω/□, which is agreeable with the specifications provided by Delta Technologies, Inc. (10 ± 5 Ω/□), indicating a conductivity of 8240 S/cm. The sheet resistance of the FTO is 11.43 Ω/□, matches with the sheet resistance

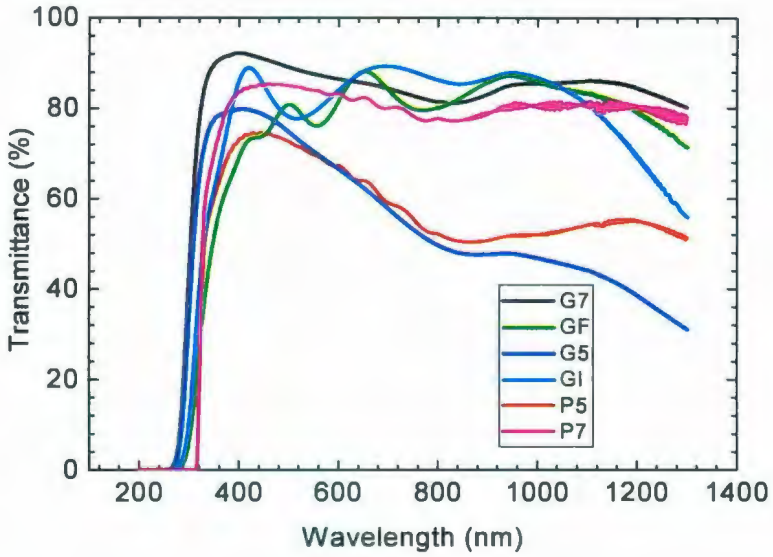

Figure 5.3: Transmission spectra of different anode/substrate systems: PH750 (G7), FTO (GF), PH510 (G5), ITO (GI) on glass substrates, and PH510 (P5), PH750 (P7) on PET substrates.

resistance specified by Solaronix SA (~10 Ω/□), thus the conductivity is 7290 S/cm. The sheet resistance of the PH510 film with a thickness of 65 nm is 500 Ω/□, corresponding to 310 S/cm for the conductivity, which falls in the range suggested by H. C. Starck (> 300 S/cm). The sheet resistance of the PH750 film is 342 Ω/□, which corresponds to 630 S/cm with a good agreement with the conductivity given by H. C. Starck (650 S/cm). In device applications such as organic thin film transistor, solar cell, and dye-sensitized solar cell, the effect of a highly conductive anode on the device performance has been studied [94,96,117], which indicated that an anode of higher conductivity or a lower sheet resistivity results in a superior device performance.

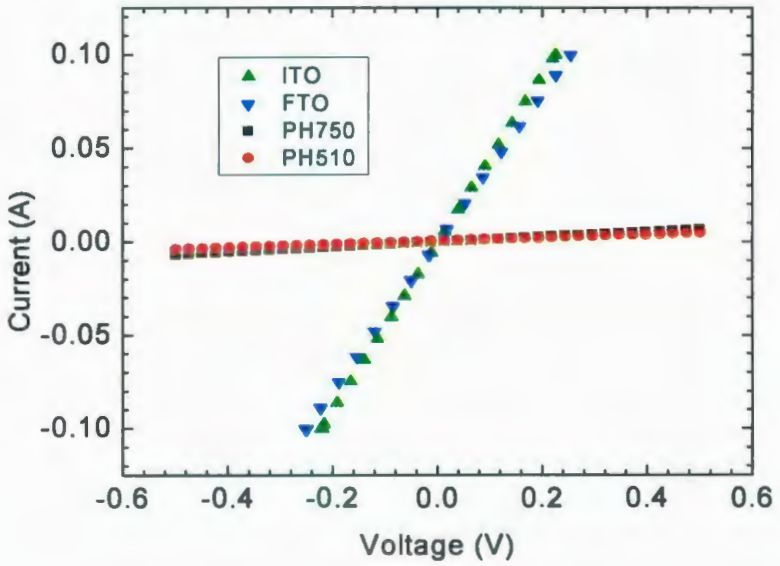

Figure 5.4: *I-V* curves for different anodes (ITO, FTO, PH750, and PH510) on glass substrates.

Figure 5.5 shows the AFM images of ITO, FTO, PH510, and PH750 films coated on glass substrates and PH510 coated on a PET substrate. It is difficult to perform a morphological observation on PET film by AFM because plastics suffer from shrinkage (Fig. 5.5e). The rms roughnesses of the ITO and FTO films on glass are 1.986 and 1.657 nm, respectively. The rms roughnesses of the PH510 and PH750 films spin-coated on glass are 2.157 and 2.717 nm, respectively. These rms roughness data were calculated from the AFM software "WITec Project 1.92", this software calculated the roughness with three decimal places, and without experimental uncertainty. Djurišić *et al.* studied the influence of the anode roughness on the performance of an organic solar cells by using CuPc and C_{60} as donor and acceptor materials, respectively, and reported that the short circuit current of the organic solar cells is inversely proportional to the rms roughness of the anode [30]. Therefore, low roughness of FTO on a glass substrate should

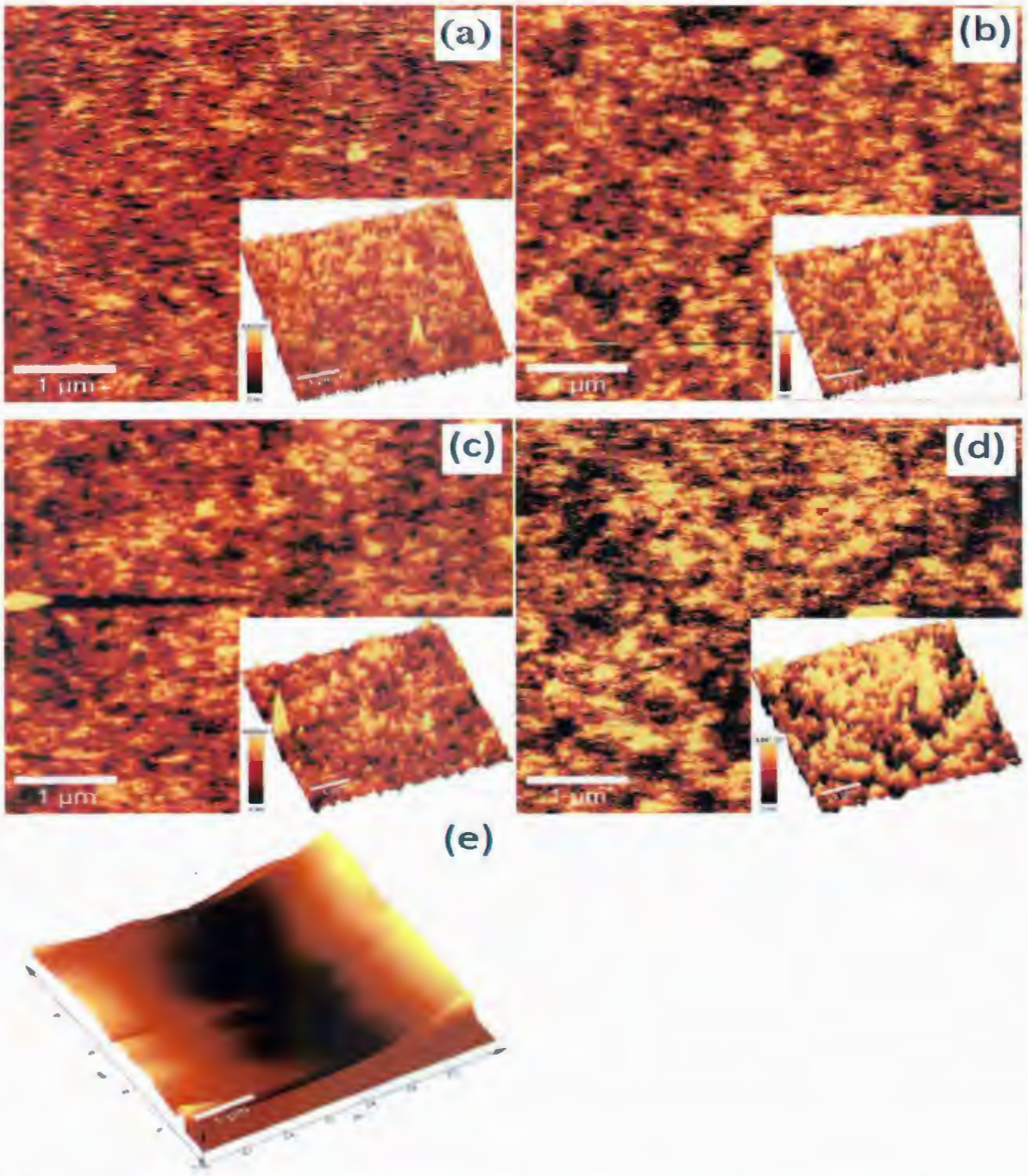

Figure 5.5 Morphologies of different anodes observed by AFM in AC mode: (a) ITO on a glass substrate, (b) FTO on a glass substrate, (c) PH510 on a glass substrate, (d) PH750 on a glass substrate, and (e) PH510 on a PET substrate.

have a positive effect on the performance of OSCs. However, the performance of an OSC is not solely dependent on the roughness of the anode film, which is also influenced by other factors, such as the transmittance and conductivity of the anode. It is not conclusive to determine which anode/substrate system gives the best photovoltaic performance simply by judging the roughness of the anode film.

After characterizing PH510 and PH750 on glass or PET substrate, P3HT:PCBM solar cells based on these six different anode/substrate systems are fabricated. *J-V* curves of these six different solar cells are compared in Fig. 5.6. The reference cell (ITO on glass) shows a relatively high performance with I_{sc} = 9.51 mA/cm^2, V_{oc} = 0.59 V, *FF* = 41%, corresponding a PCE of 2.33%. The highest PCE (2.35%) which is close to the PCE of the reference cell is obtained by using FTO as an anode, due to the accompanying lowest roughness, second highest conductivity and relatively high transmittance. The corresponding I_{sc}, V_{oc}, and *FF* are 9.58 mA/cm^2, 0.56 V, and 41%, respectively. For the systems of glass substrate with the lowest conductivity, the second largest roughness, and relatively low transmittance, the device consisting of PH510 shows the lowest PCE, with I_{sc} = 8.19 mA/cm^2, V_{oc} = 0.56, *FF* = 32%, and PCE = 1.47%. Compared with G5 devices, the device of PH750 on glass substrate shows a relatively higher performance with I_{sc} = 9 mA/cm^2, V_{oc} = 0.56 V, and *FF* = 32%, corresponding a PCE of 1.62%. The reason for that is because PH750 film has a larger transmittance, and higher conductivity which is nearly double the value for the PH510 film, though the PH750 film has a rougher surface than the PH510 film.

A femtosecond laser is not able to pattern an anode film on a plastic substrate due to the thermal shrinkage. In this case, a PVC tape is used to pattern the anode on the plastic substrate.

The viscosity of PH510 (20 – 100 mPa.s) is higher than that of PH750 (15 – 40 mPa.s). After the patterning, some parts of the PH750 film are peeled off by the tape, while the PH510 anode exhibits a better quality after patterning. Because of the lower surface quality of the PH750 film, the flexible cell P7 (PH750 on PET) exhibits an I_{sc} of 7.21 mA/cm^2, which is the same as that of the P5 cell (7.20 mA/cm^2), a FF value of 29%, and a V_{oc} value of 0.54 V, which are lower than those values of the P5 cell, i.e., 36% and 0.56 V, respectively. Thus, the PCE of the P7 is 1.14%, which is lower than that of the P5 cell (1.45%). However, the comparison between PH510 and PH750 on glass substrates shows that the PH750 film possesses a better photovoltaic performance than PH510, e.g. high transmittance, and high conductivity. This difference is attributed to the defferences in the anode properties on soft and hard substrates.

The V_{oc} values in these six anode/substrates systems remain nearly constant (0.54 – 0.59 V). The reason is that V_{oc} is influenced mainly by the difference between the highest occupied molecular orbital level of the donor and the lowest unoccupied molecular orbital level of the acceptor [37] as well as the difference in the work functions between the two electrodes [124]. The work function of ITO has been reported in the range from 4.4 to 5.1 eV [65,76,87,125]. According to the data sheet provided by H. C. Starck Inc., the work function of PH510 is approaximately 5.2 eV. Since the active layers and the cathodes adopted in these six devices are the same, the difference in the work functions of PH750 and PH510 accounts for the small variation in V_{oc}.

Since the performance of the device is influenced by many factors, including anode surface roughness, transmittance, and conductivity, it is impossible to conclude which anode/substrate system could generate the highest PCE simply by taking account of single factor.

However, as we can find from the slopes of the curves in Fig. 5.6, the series resistance R_s (inverse slope above $J = 0$) increases with the anode sheet resistance. R_s of the GI, GF, G7, and G5 devices are 15.1, 16.8, 36.8, and 40.5 Ωcm^{-2}, respectively. These results agree well with the sheet resistances of these anodes on glass substrates, which are 10.11, 11.43, 342, and 500 $\Omega/\square$ for the GI, GF, G7, and G5 devices, respectively. It can be concluded that the series resistance of the device is proportional to the sheet resistances of the anode, and thus inversely proportional to the conductivity of the anode.

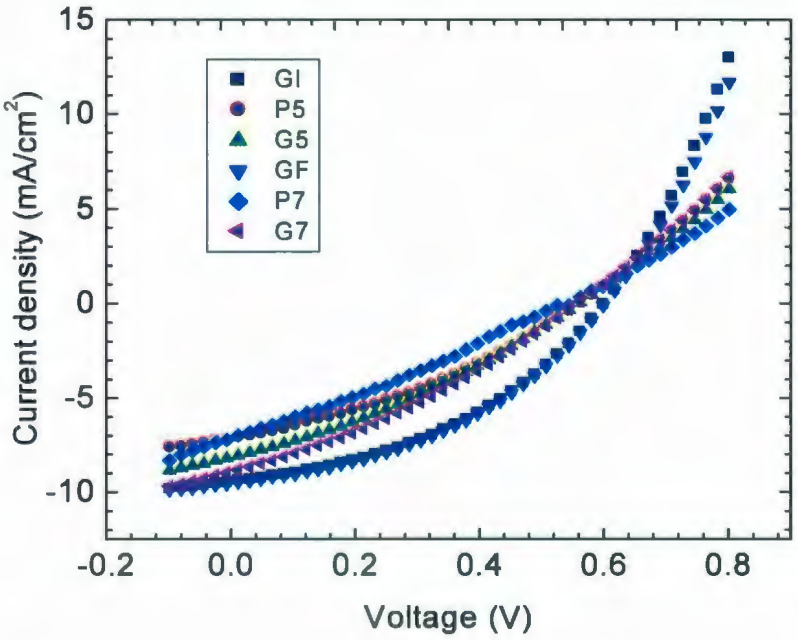

Figure 5.6: *J-V* characteristics under AM 1.5 (100 mW/cm^2) illumination for the cells with the substrate/anode systems of glass/ITO (GI), PET/PH510 (P5), glass/PH510 (G5), glass/FTO (GF), PET/PH750 (P7) and glass/PH750 (G7).

After studying the performance of the flexible devices, the effects of the cell area on the performance of the OSCs are studied. Figure 5.7 shows the effect of the six different active area

0.12 cm^2 (A0.12), 0.25 cm^2 (A0.25), 0.5 cm^2 (A0.5), 0.75 cm^2 (A0.75), 1.0 cm^2 (A1.0), and 1.25 cm^2 (A1.25) on the photovoltaic performance under AM1.5 illumination with an intensity of 100 mW/cm^2. As we can find from the slopes of the curves, the series resistance R_s (inverse slope

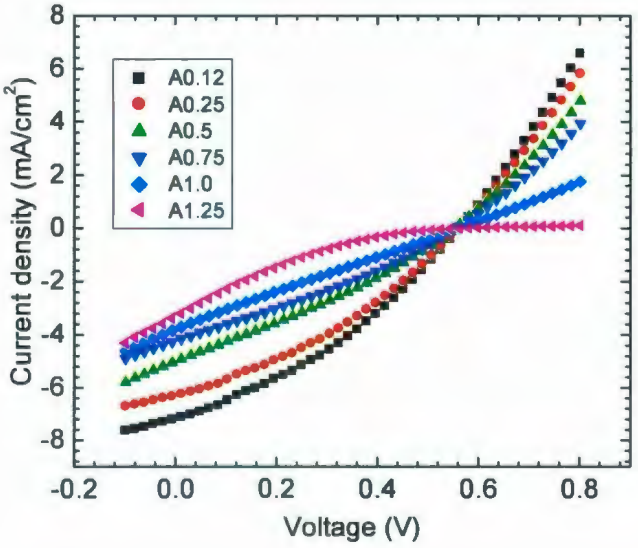

Figure 5.7: Influence of device size on the *J-V* characteristics of polymer solar cells with a configuration of PET/PH510/PEDOT:PSS(Al4083)/P3HT: PCBM/Al

above $J = 0$) increases with the cell area while the shunt resistance (inverse slope below $V = 0$) remains approximately unchanged. R_s values of 37.2, 42.3, 53.7, 64.4, 137.9, and 2285 Ωcm^{-2} have been obtained for the device areas of 0.12, 0.25, 0.5, 0.75, 1.0 and 1.25 cm^2, respectively. This tendency is in excellent agreement with the results reported by Pandey *et al.*, in which the performance of a pentacene/PCBM device is inversely proportional to the device area [120]. The parameters of the OSCs, i.e., I_{sc}, V_{oc}, FF, and PCE, are shown as a function of the cell area in Fig.

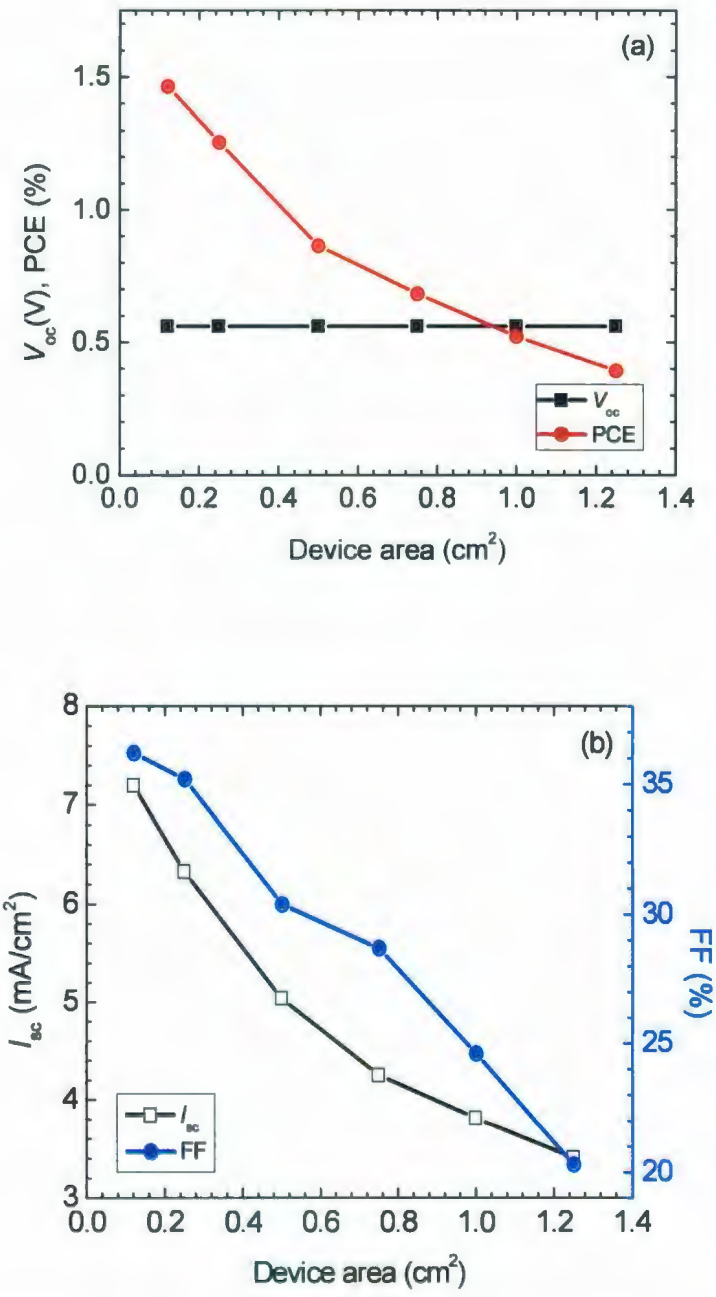

Figure 5.8: Photovoltaic performance of a flexible polymer solar cell as a function of active area: (a), V_{oc} and PCE, and (b), I_{sc} and FF. The device configuration is PET/PH510/PEDOT:PSS(Al4083)/P3HT:PCBM/Al.

5.8. Therefore, by increasing the area of the solar cell, we demonstrate that while the open circuit voltage remains unchanged (Fig. 5.8a), the electric parameter I_{sc} and *FF* decrease, corresponding to a decrease in the PCE. Because of the higher series resistance which results in lower *FF* and J_{sc}, a device with a large area (larger than 0.5 cm^2) exhibits a loss of 50% in the PCE.

The main advantage of OSCs is that they offer a low-cost, printable, portable and flexible renewable energy source. For the *J-V* measurement of a flat solar cell, P_{in} equals to P_0 (100 mW/cm^2) (Fig. 5.9). However, for a bent solar cell, the average P_{in} equals to P_0 times the ratio of

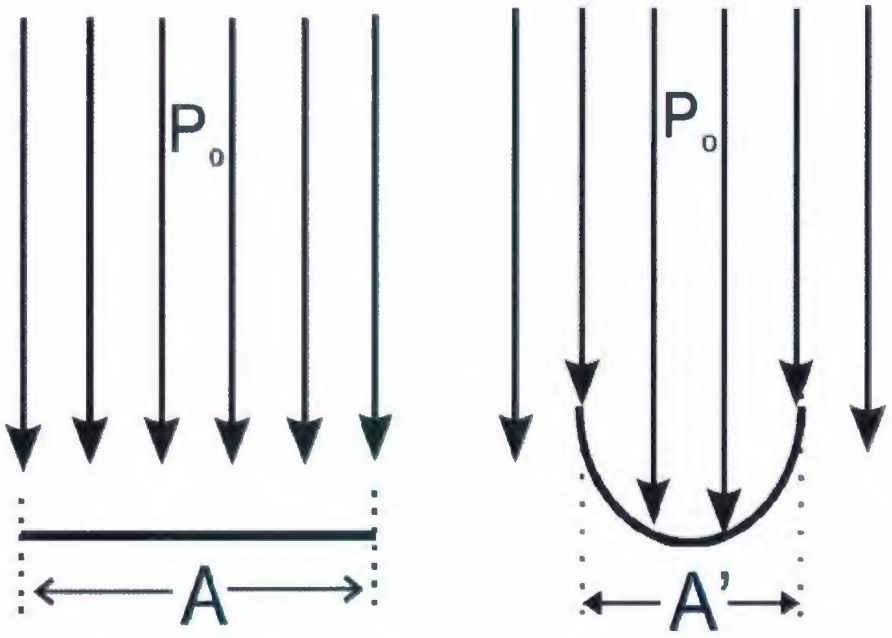

Figure 5.9: Schematic illustration of light incidence on a flat cell (left) or on a bent cell (right).

The projected area of the bent OSC area (A') over the flat OSC area (A), which is less than 100 mW/cm^2. The relationship between P_{in} and P_0 can be expressed as:

$$P_{in} = \frac{P_o A'}{A} \tag{5.2}$$

The bending angle measured here is not the real bending angle, if b equals to 14 mm, while b is the opening between the jaws of the PET substrate (Fig. 5.1), the shape of the bent OSC is a half-circle, which will be described with the definition illustrated in Fig. 5.1. A device with a smaller bending angle θ (less than 90°), which corresponds to a more significant bending of the cell, exhibits a loss of 50% in the overall performance because of the damaged morphology of the active layer that is responsible for the lower I_{sc} and V_{oc}. I_{sc} is influenced by the morphology of the active layer, which has been previously reported [16,10]. V_{oc} is mainly affected by the work function of the materials used in OSCs and some experimental observations have indicated that V_{oc} is also influenced by the morphology of the active layer [16,116] which is due to the fact that the local internal field is changed when the morphology of the active layer is changed [116]. The relationship between the performance of OSCs and the bending angle is shown in Fig. 5.10.

The SEM images of a flat cell observed under two different magnifications are shown in Fig. 5.11, indicating a smooth and uniform film. After bending the device to 100°, the SEM images of three different regions on the bent cell are shown in Fig. 5.12. Figure 5.12a illustrates the locations on the cell for the SEM observations in Fig. 5.12(b) – (c). The image manifests many cracks and rods aggregated at the abruptly bent region (Fig. 5.12c), whereas only a few cracks and rods existing on the less bent regions of the devices (Fig. 5.12 b and d). SEM images of four observation regions of a cell bent at a bending angle of 30° are shown in Fig. 5.13 with many cracks and rods at these four observation regions. The quantities of the cracks and rods are more than those of the cell with a bending angle of 100° or a flat cell. For a flexible solar cell with a bending angle of 100°, in addition to the occurrence of cracks, the film becomes rough

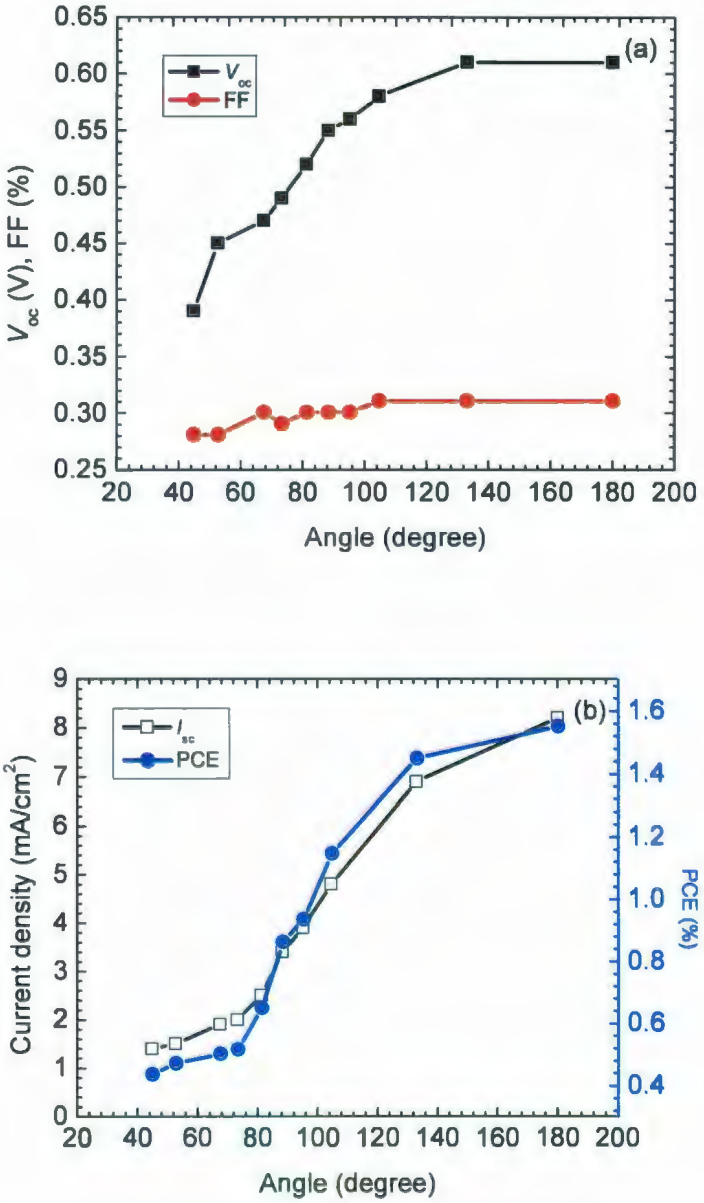

Figure 5.10: Photovoltaic performance of a flexible polymer solar cell as a function of bending angle θ: (a), V_{oc} and FF, and (b), I_{sc} and PCE. The device configuration is PET/PH510/PEDOT:PSS(Al4083)/P3HT:PCBM/Al

and inhomogeneous (Fig. 5.12). These cracks may result in the degradation of conduction in some parts of the active layer, thus an inhomogeneous layer is not desired in optoelectronic devices, e.g. OLED, organic thin film transistor (OTFT), and OSC. More cracks appear (Fig. 5.13) in the case for a flexible solar cell with a bending angle of 30°. Fortunately, these cracks do not connect together to cause an open circuit and a *J-V* curve is still possible to obtain. Therefore, the performance of an OSC critically depends on the bending angle with the PCE of the OSC decreases as the bending angle decreases.

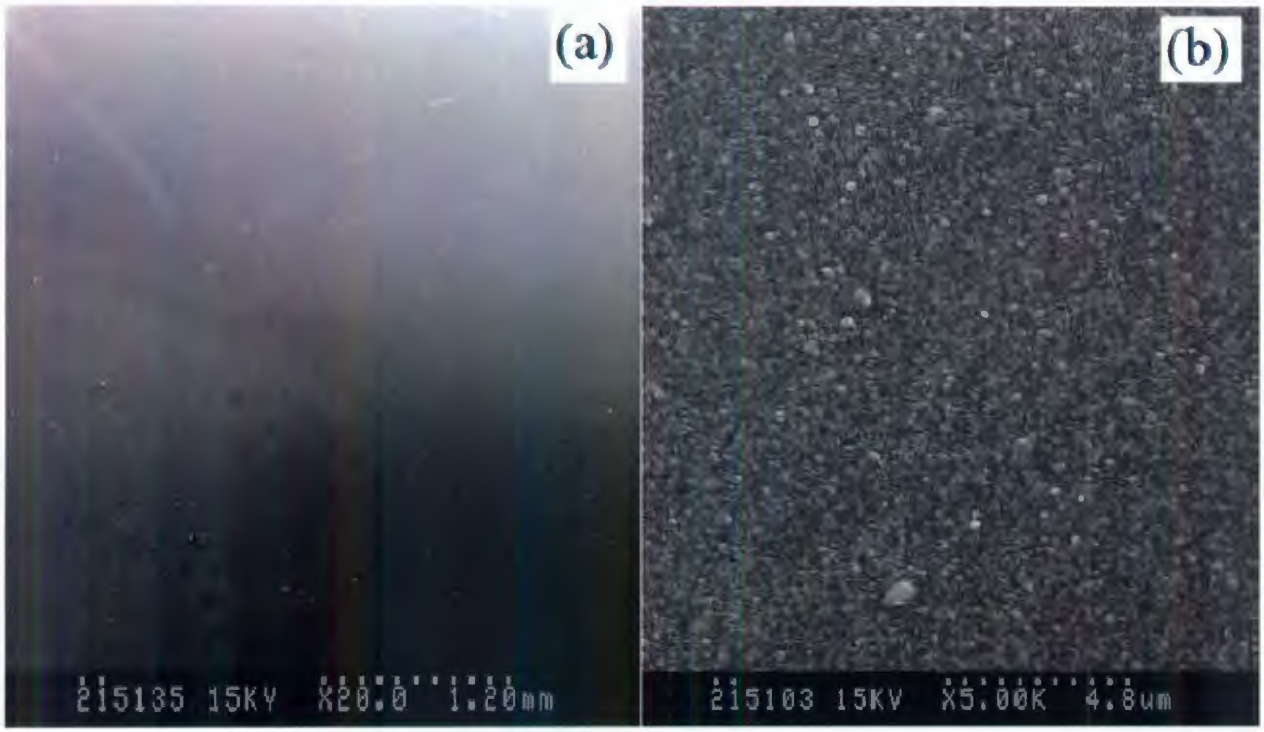

Figure 5.11: SEM images of a flexible solar cell before bending observed under different magnifications.

In order to reveal the morphology changes of each layer of the cell under bending, the SEM images of each layer of the multilayered cell before and after bending are shown in Figs. 5.14-17. A flat PH510 deposited PET is uniform and smoothes (Fig. 5.14a). However, after

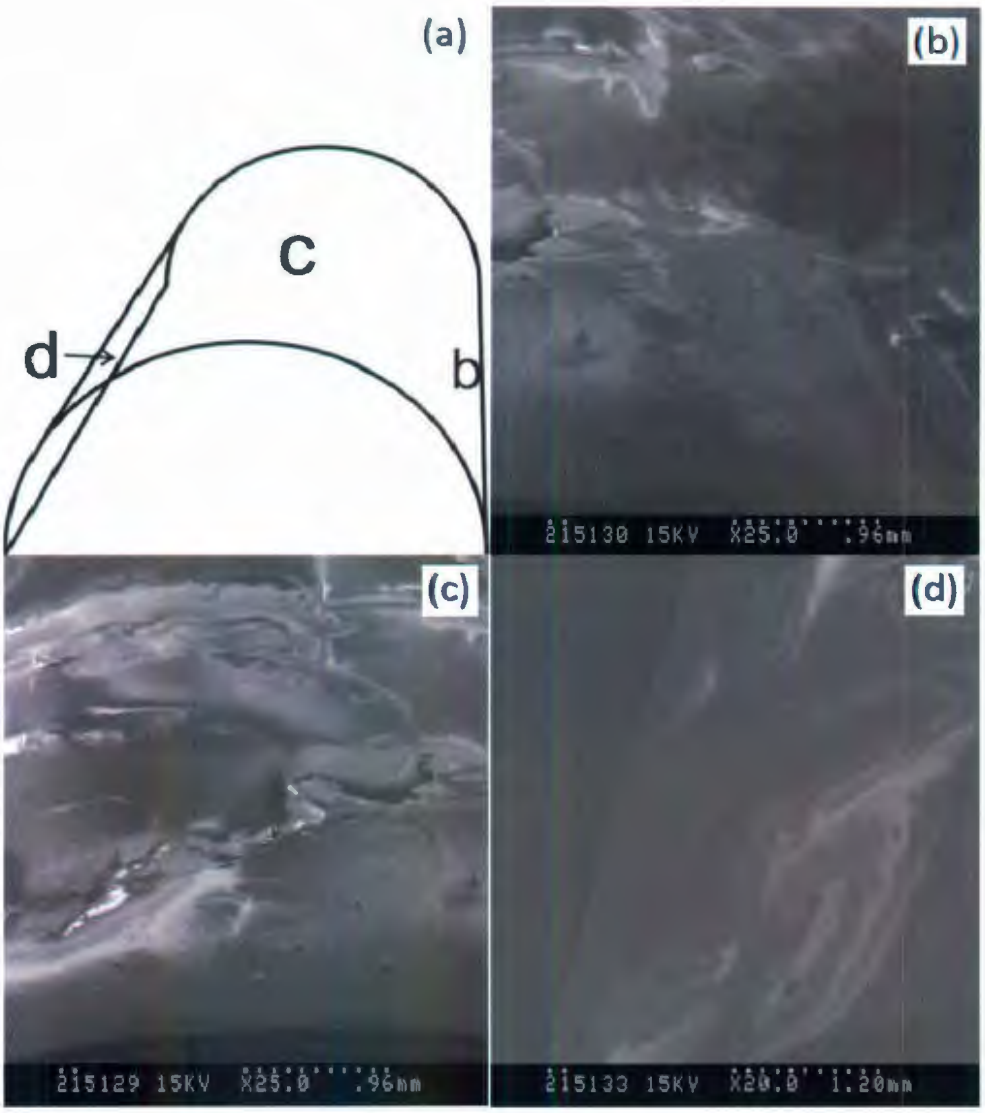

Figure 5.12: SEM images of the flexible solar cell with a bending angle of 100° observed at different locations: (a), schematic illustration of the regions on the device for observation, (b), image taken at one side of less bent region, (c), image taken at the bent region, and (d) image taken at the other side of the less bent region.

bending PH510 film to 30°, there are many rods occurred at the abruptly bent regions, which is evident in Fig. 5.14(c) - (e), whereas only a few rods are found in less bent regions (Fig. 5.14c). Similar rods can also be found after further increasing the observation magnification. These rods

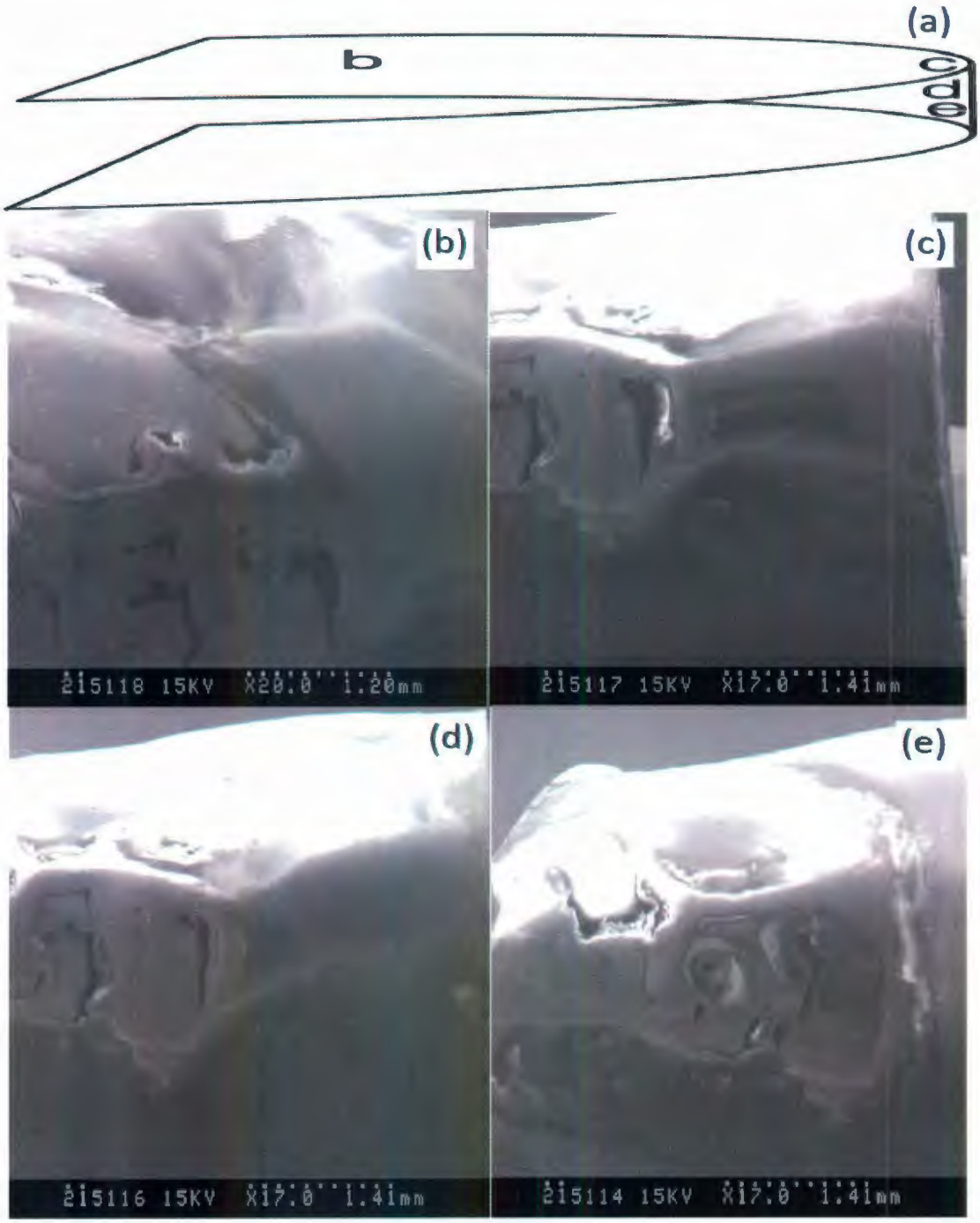

Figure 5.13: SEM images of the flexible solar cell with a bending angle of 30° observed at different locations: (a), schematic illustration of the regions on the device for observation, (b), image taken at one side of less bent region, (c), image taken at the bent region, and (d) image taken at the other side of less bent region, (e) image taken at the other side of bent region.

do not exist on a flat PH510 film in the SEM observation under the same magnification (Fig. 5.14b). SEM images of PVP Al 4083 and P3HT:PCBM films deposited on the PET substrates are shown in Figs. 5.15 and 5.16, respectively. Figure 5.15 (a), (c), and (e) show the morphologies of the flat PVP Al4083 film observed at increasing magnifications. After bending the 4083 film to 30°, as shown in Fig. 5.15(b), (d), and (f), the film shows the similar morphology as the flat 4083 film, which is smooth and uniform. P3HT:PCBM layer also exhibits a less influence upon bending, the flat P3HT:PCBM film on PET substrate is smooth and uniform, as shown in Fig. 5.16(a), (c), and (e). After bending the P3HT:PCBM film to 30°, no significant change in the morphology has been found in Fig. 5.16 (b), (d), and (f), which are similar to the quality of the flat P3HT:PCBM film. As shown in Fig. 5.17(a), (c), and (e), a flat Al film deposited on the PET substrate shows a smooth and uniform morphology, however, some inhomogeneities appear on the film when the Al film is bent with a bending angle of 30° (Fig. 5.17b), thus the film becomes rough. Many cracks are visible from the image taken at a higher magnification, and become significant when the SEM magnification is further increased as shown in Fig. 5.17 (d), and (f). The SEM observation of the individual layers of the device (Figs. 5.14-17) indicates that the morphologies of the Al and PH510 films are significantly deformed by the bending effect, which is evident from the occurrence of many cracks and rods in the bent Al and PH510 films. Since both PVP Al4083 and P3HT:PCBM films are soft materials, they are less susceptible to the bending. Although PH510 is also a soft material, the rods found in the bent PH510 films may be due to the tension resulted from the bending as the thickness of the PH510 is the largest in the device. As shown in Fig. 5.18 for the SEM images of PH510/PVP Al4083 films deposited on the PET substrates, this bilayer system presents a smooth and uniform

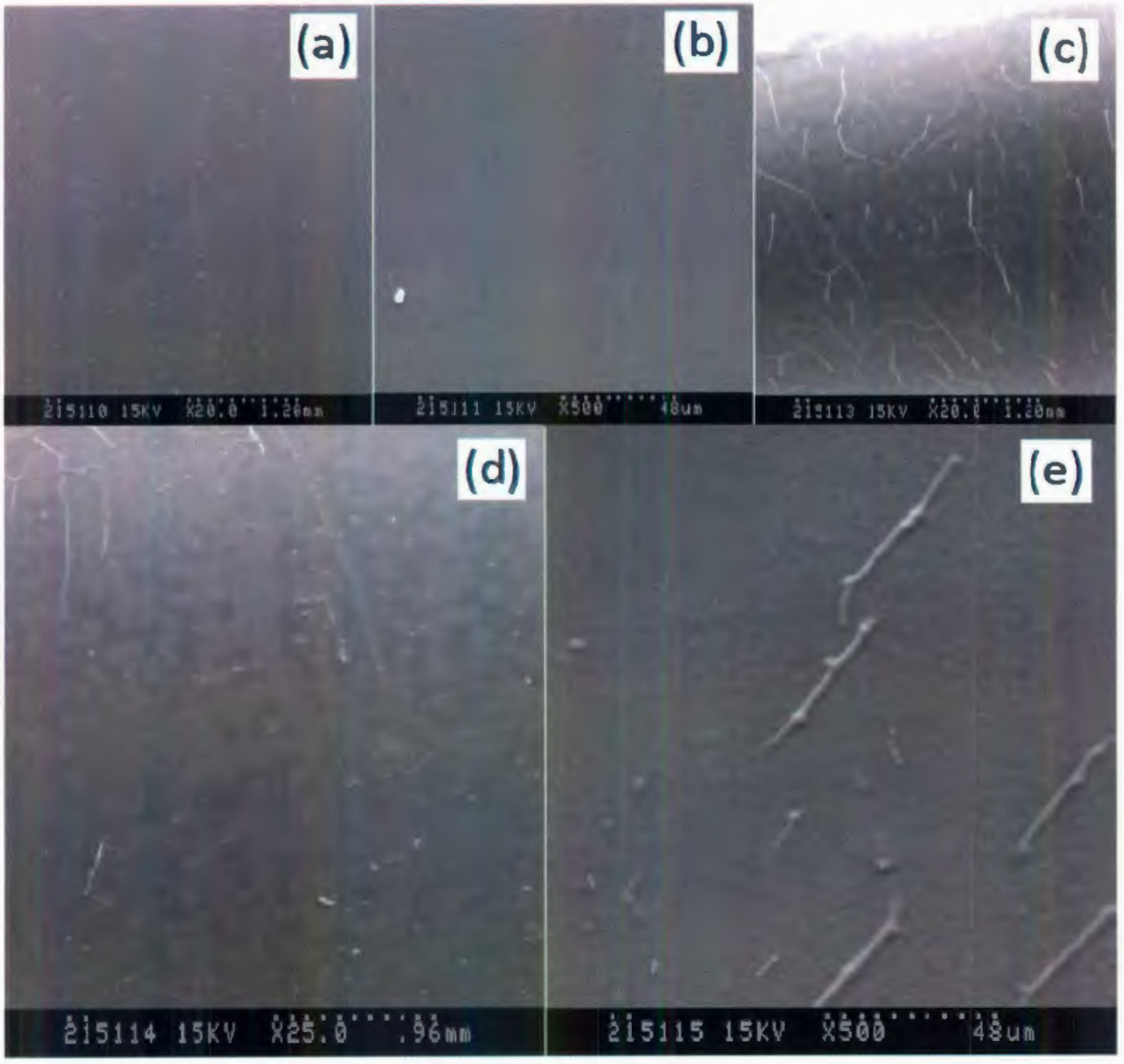

Figure 5.14: SEM images of the PH510 film: (a) and (b), observed before bending with different magnifications, and (c), (d), and (e), with a bending angle of 30° observed at different magnifications.

morphology in Fig. 5.18 (a), (c), and (e) before bending. When the film is bent with a bending angle of 30°, there are some cracks and wrinkles observed on the films, and some parts of the film become thin as seen in Fig. 5.18 (b). When the magnification is further increased, more

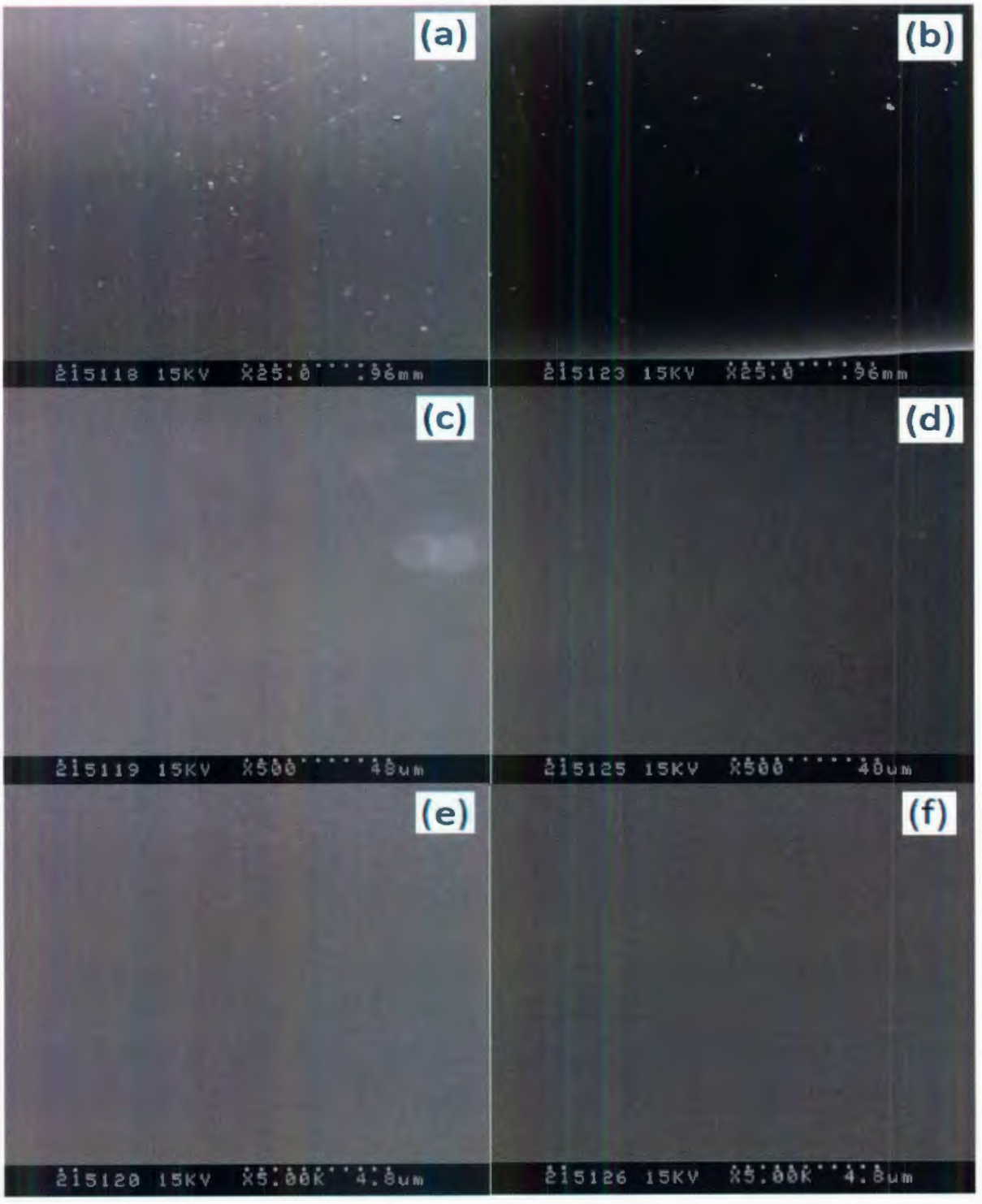

Figure 5.15: SEM images of the PVP Al4083 film: (a), (c), and (e), observed before bending with different magnifications and (b), (d), and (f), with a bending angle of 30° at different magnifications.

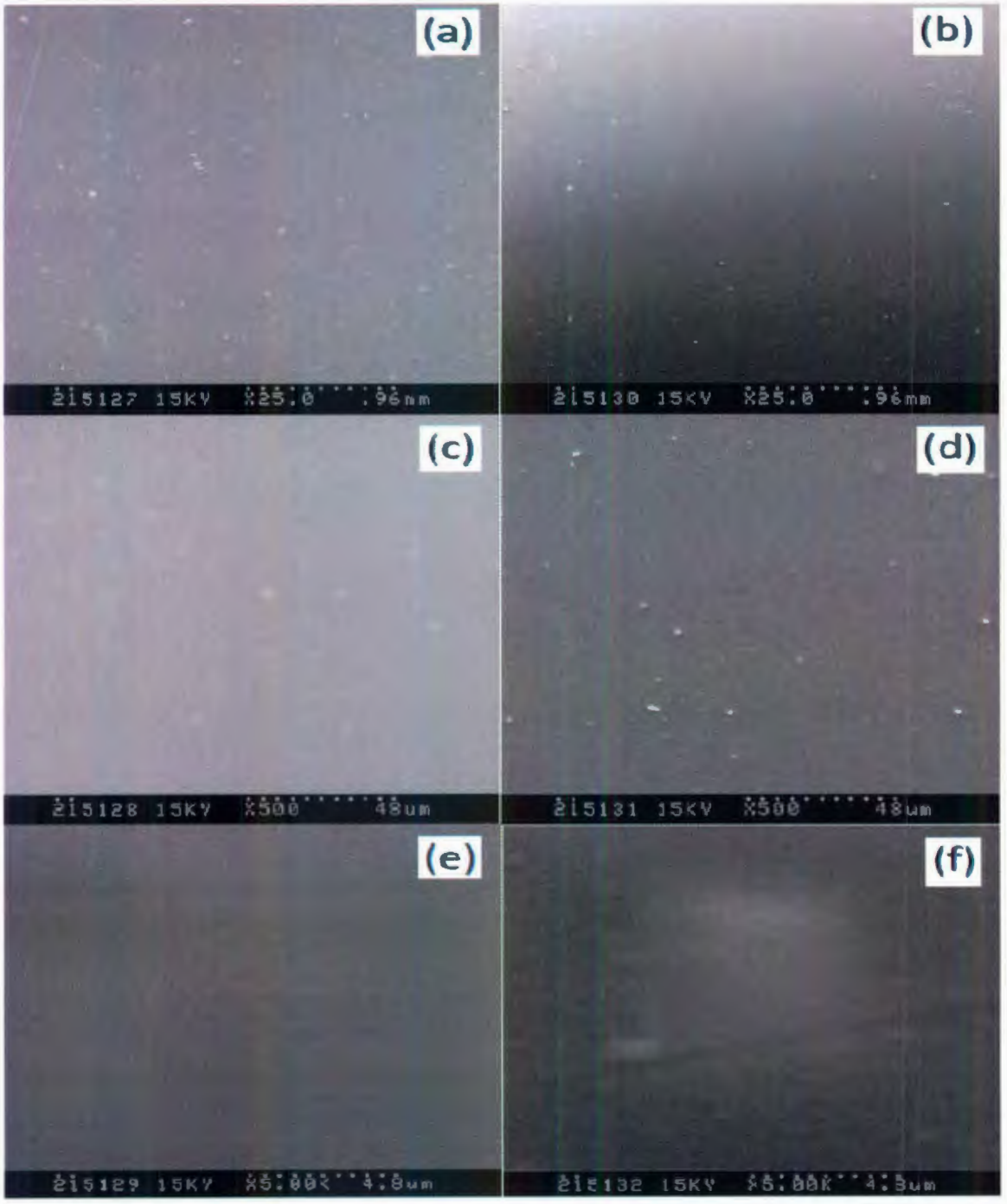

Figure 5.16: SEM images of the P3HT:PCBM film: (a), (c), and (e), observed before bending with different magnifications, and (b), (d), and (f), with a bending angle of 30° observed at different magnifications.

wrinkles and bubbles can be observed in Fig. 5.18 (d) and (f). From the SEM images of PH510/PVP Al 4083/P3HT:PCBM films deposited on the PET substrates shown in Fig. 5.19, a flat film of PH510/PVP Al4083/P3HT:PCBM exhibits uniform morphology, however, cracks are observed on the film at a bending angle of 30° in Fig. 5.19(b). When the magnification is increased to 500, some bubbles and black holes display on the film. With a further increased magnification, these black holes appear to be the aggregation of some bubbles.

5.4 Conclusions

The relationship between the performance of OSCs and electrode properties is studied on four kinds of anodes (ITO, FTO, PH750, and PH510), and six anode/substrate systems in order to identify a low-cost, efficient and flexible anode/substrate system. Since the FTO and ITO films have a high transmittance, conductivity, and relatively low roughness, OSCs with FTO and ITO films on glass substrates show PCE values of 2.35% and 2.33%, respectively. Due to the fact that the PH750 film has a higher transmittance and conductivity than those of PH510 film, the PCE value of PH750 film on glass substrate (1.62%) is higher than that of PH510 film (1.47%). Series resistance of an OSC is proportional to the sheet resistance of the anode. For flexible solar cells, since the PH510 film shows a better film quality after patterning, the performance of the PH510 film on a PET substrate (1.45%) is higher than that of the PH750 film on PET substrate (1.14%). Since the typical size of an OSC is 0.09 - 0.15 cm^2, which is too small to be bent, OSCs of varying sizes have been fabricated in order to measure the relationship between the bending angle and the performance of OSCs. Due to the fact that the series

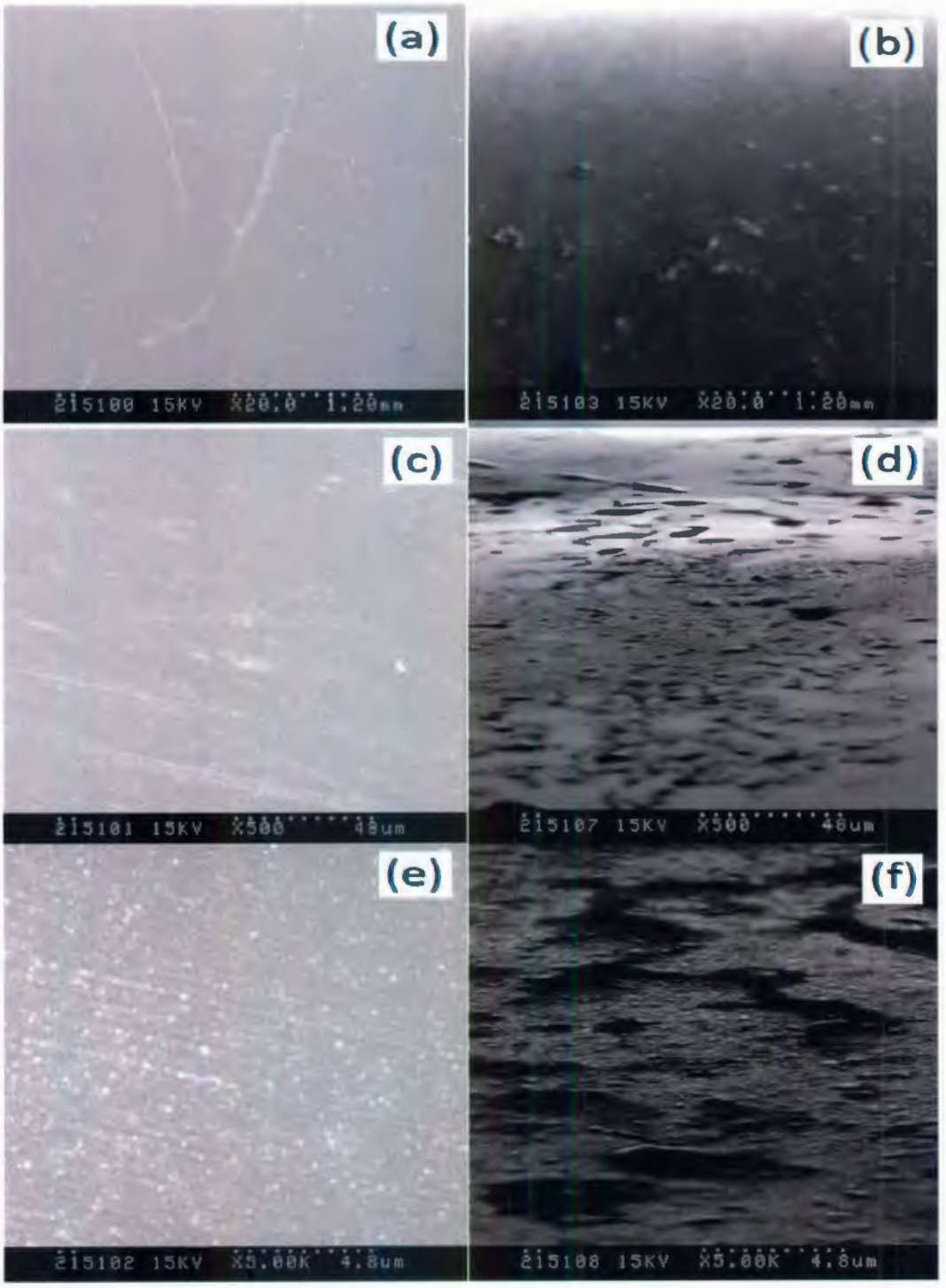

Figure 5.17: SEM images of the Al film: (a), (c), and (e), observed before bending with different magnifications, and (b), (d), and (f), with a bending angle of 30° observed at different magnifications

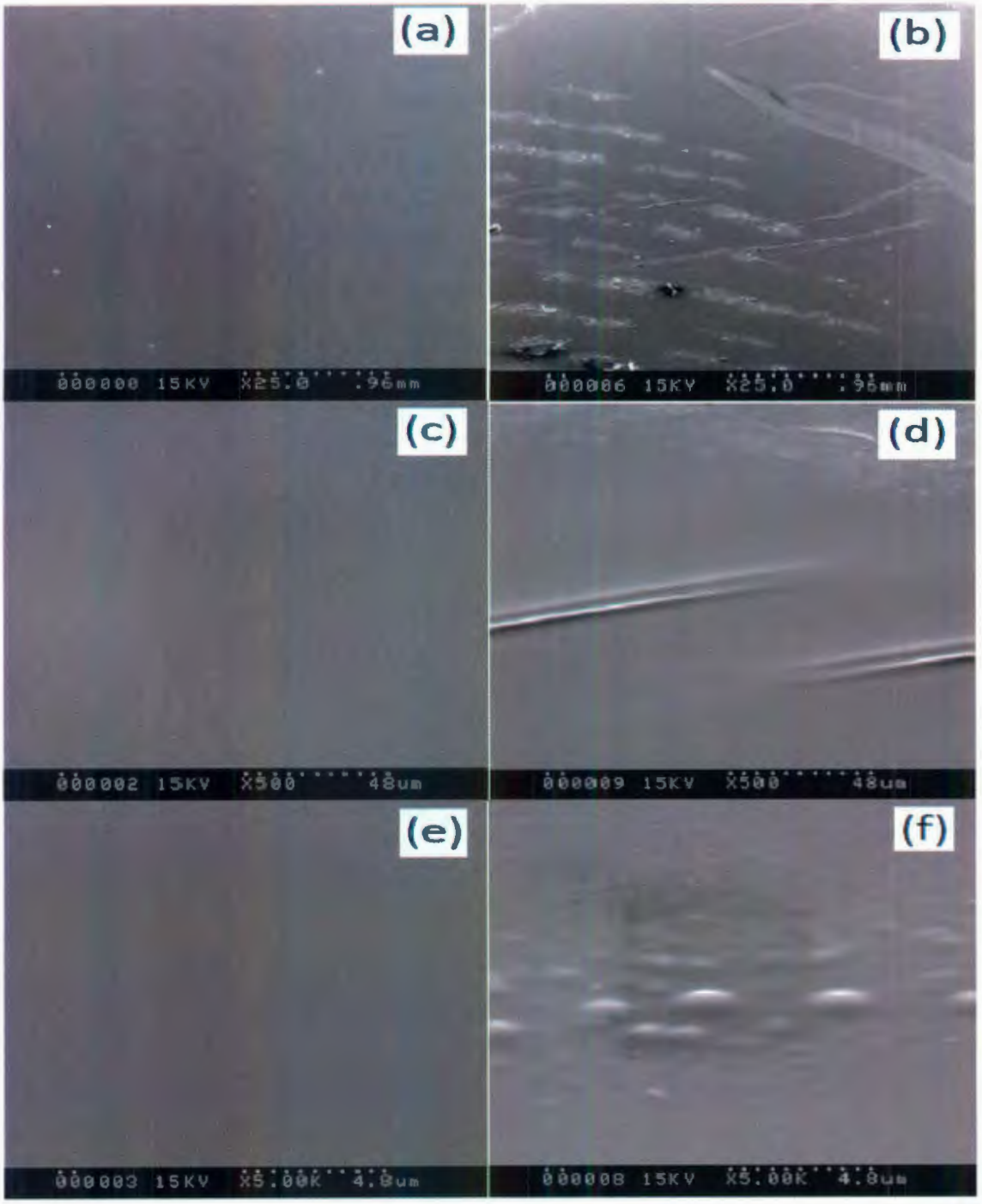

Figure 5.18: SEM images of the PH510/PVP Al4083 bilayer: (a), (c), and (e), observed before bending with different magnifications, and (b), (d), and (f), with a bending angle of 30° observed at different magnifications.

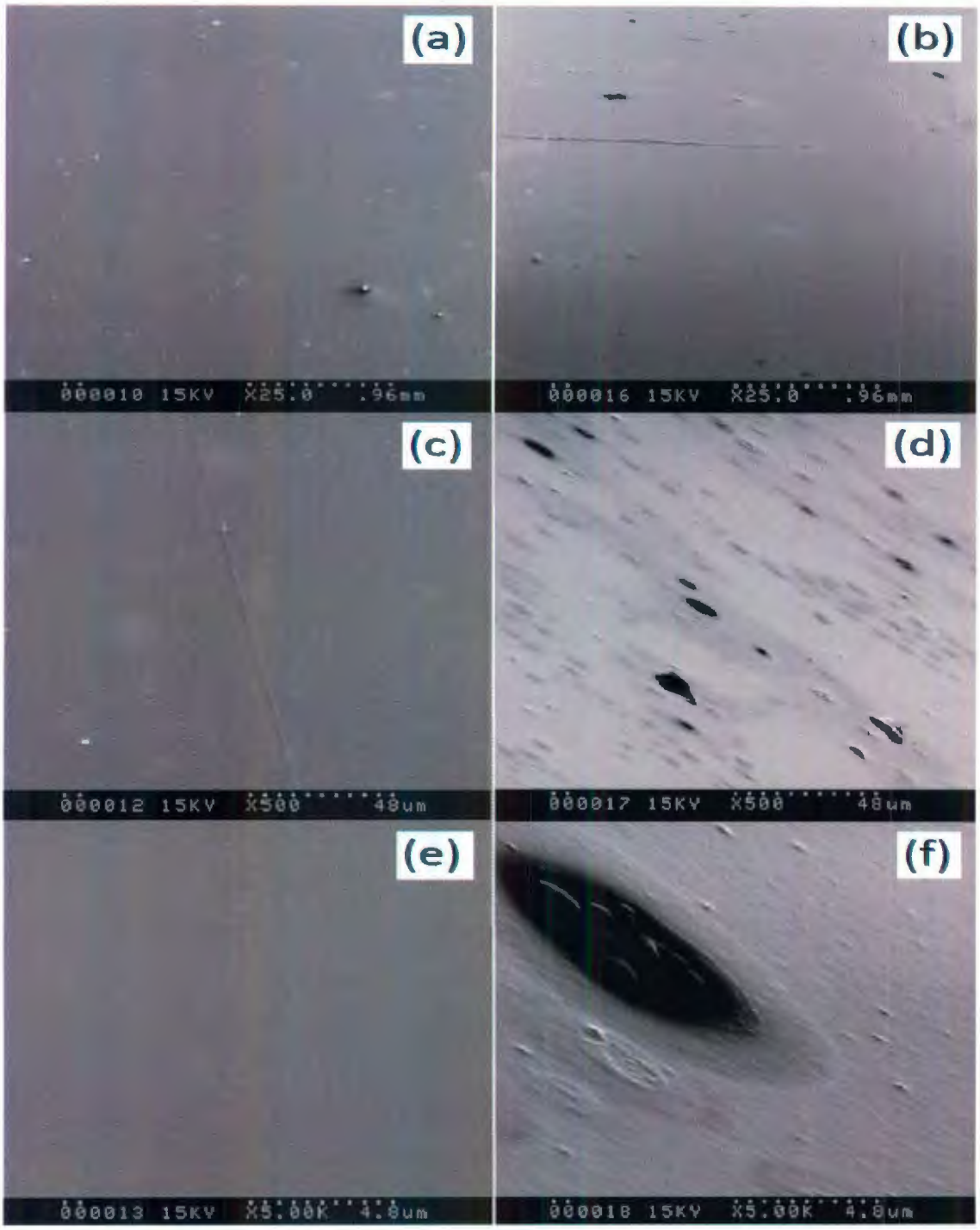

Figure 5.19: SEM images of the PH510/PVP Al4083/P3HT:PCBM trilayer: (a), (c), and (e), observed before bending with different magnifications, and (b), (d), and (f), with a bending angle of 30° observed at different magnifications.

resistance of an OSC increases with the increase in the device area, the performance of the OSC is inversely proportional to the area of the device. Considering the size and the performance of the OSC, an active area with a size of 20 mm in length and ~1.2 mm in width is adopted in this study to measure the relationship between the device performance and the bending angle. SEM study indicates that the quality and morphology of the films become worse after bending with more cracks at significant bending. The SEM images of the individual layer of the device reveal that the morphologies of the PH510 and Al layers are significantly influenced by the bending effect. The performance of an OSC gradually decreases as the bending angle decreases.

Chapter 6

Conclusions and future work

6.1 Conclusions

The goal of this thesis is to develop universal techniques in ambient environment to improve the efficiency of organic solar cells, which has been carried out with several approaches: (a) surface treatments of ITO substrates, (b) optimization of buffer layer, and (c) device processing with additives.

There are a few reports so far on the ITO treatments used in OSCs, however, our study here presents the first investigation on the ITO treatment for P3HT solar cells. The efficiency of the device with ITO irradiated by 23 mW/cm^2 UV light shows an 80% increment, as compared with the efficiency of the device fabricated on untreated ITO substrate. PH510 is a highly conductive PEDOT usually used on electrode, PVP Al4083 is another PEDOT commonly used

as buffer layer. Here, we first propose an approach to blend and dissolve them at 1:2.5 ratio in solvents, and then spin coating this precursor on the top of ITO to be the buffer layer of OSCs. The efficiency of the OSCs indicates a significant improvement of 40%, i.e., from 2.08% to 2.92%. We find for the first time that the efficiency of MEH-PPV solar cell can be enhanced by processing with either 1,8-octanedithiol (ODT) or dimethyl sulfoxide (DMSO) additives, i.e., efficiency of MEH-PPV solar cell increases from 2.5% to 2.8% after doped 1% of ODT, and from 2.5% to 3.15% by doping 5% (vol) of DMSO. Our PCE value of 3.15% is the highest efficiency of MEH-PPV solar cells reported so far.

Figure 6.1: A flexible organic solar cell.

One main advantage of OSC is its flexibility. However, most of the OSCs reported so far are based on glass substrates. In this study, we succeed in the fabrication of OSCs on a flexible PET substrate (Fig. 6.1). The efficiencies of the OSCs with different anode/substrate systems are measured and compared. In order to measure the bending effects of OSCs, large-sized OSCs have been adopted instead of conventional small cells with an area between 0.04 and 0.15 cm^2.

The size effect of OSCs has been revealed, indicating that the efficiency of the devices decrease as the device area increases due to the increase in the series resistance. Furthermore, the relationship between the bending angle of an OSC and its efficiency has been identified as the efficiency of the OSC decreases as the bent angle decreases, due to the significant change in the morphology of PH510 and Al films at a small bending angle.

6.2 Future work

In this study, the efficiency of the OSC has been improved through three universal techniques. However, the lifetime and stability issues associated with organic solar cells are still challenging aspects for further study.

All the FF values of the OSCs in this study are lower than those of the OSCs fabricated in nitrogen condition. The reason is that Al oxidizes quickly in ambient condition, which is a fast process to change Al to Al_2O_3, accompanying with ten millions times increase in the resistivity. Since the series resistance of the device is proportional to the Al cathode resistance, series resistance of the cell built in ambient condition is much larger than that of the device fabricated in nitrogen condition. Since FF is closely related with the series resistance, it will be interesting to fabricate OSCs in an inert environment in order to compare the FF value with that of the OSC built in ambient condition.

Recently, zinc oxide (ZnO) has attracted much attention as solar cell electrode [126,127], optical spacer [128,129], and active layer additive [130,131]. It may be possible to use ZnO film as the electrode in OSCs, or as a buffer layer in an OSC instead of PEDOT.

6.3 Contributions

Part of the results in this thesis has been reported and published in the following conferences and proceedings. Several journal submissions are currently in preparation.

1. Y. Ding and Q. Chen, "Improved bulk-heterojunction polymer solar cells with paraphenylenevinylene and fullerene," in *Conference on Lasers and Electro-Optics/International Quantum Electronics Conference*, OSA Technical Digest (CD) (Optical Society of America, 2009), paper CFQ6.

2. Y. Ding, P. Lu, and Q. Chen, Optimizing material properties of bulk-heterojunction polymer films for photovoltaic applications, Proc. SPIE, 7099, 7099-57 (2008).

3. Y. Ding and Q. Chen, "Improving composite polymer films for photovoltaic applications", Canadian Association of Physicists Congress, June 8-11, 2008, Quebec City, Quebec, Canada.

Bibliography

[1] C. B. Hatfield, "Oil back on the global agenda," *Nature*, vol. 387, p. 121, 1997.

[2] Intergovernmental Panel on Climate Change (IPCC), "Second Assessment Report-Climate Change 1995," 1995.

[3] United Nations Environment Program (UNEP), *Global Environment Outlook (GEO)-2000.* London: Earth Scan Publications Ltd., 2000.

[4] M. D. Archer, and R. Hill, *Clean Electricity from Photovoltaics*. London: Imperial College Press., 2001.

[5] L. Frazer, "Organic Electronics: A Cleaner Substitute for Silicon," *Environmental Health Perspectives*, vol. 111, 2003.

[6] J. Y. Kim, K. Lee, N. E. Coates, D. Moses, T. Nguyen, M. Dante, and A. J. Heeger, "Efficient tandem polymer solar cells fabricated by all-solution processing," *Science*, vol. 317, pp. 222-225, 2007.

[7] R. McNeill, R. Siudak, J. H. Wardlaw, and D. E. Weiss, "Electronic conduction in polymers. I. the chemical structure of polypyrrole," *Australian Journal of Chemistry*, vol. 16, pp. 1056-1075, 1963.

[8] [Online]. http://nobelprize.org/nobel_prizes/chemistry/laureates/2000/

[9] G. Yu, J. Gao, J. C. Hummelen, F. Wudl, and A. J. Heeger, "Polymer photovoltaic cells: enhanced efficiencies via a network of internal donor-acceptor heterojunctions," *Science*, vol. 270, pp. 1789-1791, 1995.

[10] G. Li, V. Shrotriya, J. Huang, Y. Yao, T. Moriarty, K. Emery, and Y. Yang, "High-efficiency solution processable polymer photovoltaic cells by self-organization of polymer blends," *Nature Materials*, vol. 4, pp. 864-868, 2005.

[11] Y. Kim, S. Cook, S. M. Tuladhar, S. A. Choulis, J. Nelson, J. R. Durrant, D. D. C. Bradley, M. Giles, I. McCulloch, C. Ha and M. Ree, "A strong regioregularity effect in self-organizing conjugated polymer films and high-efficiency polythiophene:fullerene solar cells," *Nature Materials*, vol. 5, pp. 197-203, 2006.

[12] M. Reys-Reys, K. Kim, and D. L. Caroll, "High-efficiency photovoltaic devices based on annealed poly(3-hexylthiophene) and 1-(3-methoxycarbonyl)-propyl-1-phenyl-(6,6)C61 blends," *Appl. Phys. Lett.*, vol. 87, p. 083506, 2005.

[13] W. Ma, C. Yang, X. Gong, K. Lee, and A. J. Heeger, "Thermally stable, efficient polymer solar cells with nanoscale control of the interpenetrating network morphology," *Adv. Funct. Mater.*, vol. 15, p. 1617, 2005.

[14] C. V. Hoven, R. Yang, A. Garcia, V. Crockett, A. J. Heeger, G. C. Bazan, and T. Nguyen, "Electron injection into organic semiconductor devices from high work function cathodes," *Proc. Nati. Acad. Sci.*, vol. 105, pp. 12730-12735, 2008.

[15] D. W. Sievers, V. Shrotriya, and Y. Yang, "Modeling optical effects and thickness dependent current in polymer bulk-heterojunction solar cells," *J. Appl. Phys.*, vol. 100, p. 114509, 2006.

[16] G. Li, V. Shrotriya, Y. Yao, and Y. Yang, "Investigation of annealing effects and film thickness dependence of polymer solar cells based on poly(3-hexylthiophene)," *J. Appl.*

Phys., vol. 98, p. 043704, 2005.

[17] E. Lebedev, T. Dittrich, V. Petrova-Koch, S. Karg, and W. Brutting, "Charge carrier mobility in poly(p-phenylenevinylene) studied by the time-of-flight technique," *Appl. Phys. Lett.*, vol. 71, p. 2686, 1997.

[18] R. Gómez, J. L. Segura, and N. Martín, "Highly efficient light-harvesting organofullerenes," *Org. Lett.*, vol. 7, pp. 717-720, 2005.

[19] D. Chirvase, Z. Chiguvare, M. Knipper, J. Parisi, V. Dyakonov, J. C. Hummelen, "Electrical and optical design and characterisation of regioregular poly(3-hexylthiophene-2,5diyl)/fullerene-based heterojunction polymer solar cells," *Syn. Metals*, vol. 138, pp. 299-304, 2003.

[20] G. Yu, A. J. Heeger, "Charge separation and photovoltaic conversion in polymer composites with internal donor/acceptor heterojunctions," *J. Appl. Phys.*, vol. 78, pp. 4510-4515, 1995.

[21] J. J. M. Halls, C. A. Walsh, N. C. Greenham, E. A. Marseglia, R. H. Friend, S. C. Moratti, A. B. Holmes, "Efficient photodiodes from interpenetrating polymer networks," *Nature*, vol. 376, pp. 498-500, 1995.

[22] K. Yoshino, K. Tada, A. Fujii, E. M. Conwell, A. A. Zakhidov, "Novel photovoltaic devices based on donor-acceptor molecular and conducting polymer systems," *IEEE Trans. Electron Dev.*, vol. 44, pp. 1315-1324, 1997.

[23] S. H. Park, A. Roy, S. Beaupré, S. Cho, N. Coates, J. Moon, D. Moses, M. Leclerc, K. Lee,

A. J. Heeger, "Bulk heterojunction solar cells with internal quantum efficiency approaching 100%," *Nature Photonics*, vol. 3, p. 297, 2009.

[24] S. E. Shaheen, C. J. Brabec, N. S. Sariciftci, F. Padinger, T. Fromherz, and J. C. Hummelen, "2.5% efficient organic plastic solar cells," *Appl. Phys. Lett.*, vol. 78, pp. 841-843, 2001.

[25] K. Lee, J. Y. Kim, and A. J. Heeger, "New architecture for high-efficiency polymer photovoltaic cells using solution-based titanium oxide layer," *Proc. SPIE*, vol. 6117, p. 61170T, 2006.

[26] T. J. Prosa, M. J. Winokur, J. Moulton, P. Smith, A. J. Heeger, "X-ray structural studies of poly(3-alkylthiophenes): an example of an inverse comb," *Macrommolecules*, vol. 25, p. 4364, 1992.

[27] B. R. Saunders, and M. L. Turner, "Nanoparticle-polymer photovoltaic cells," *Adv. Coll. Interf. Sci.*, vol. 138, pp. 1-23, 2008.

[28] H. Sirringhaus, N. Tessler, and R. H. Friend, "Integrated optoelectronic devices based on conjugated polymers," *Science*, vol. 280, p. 1741, 1998.

[29] C. W. Tang, "Two-layer organic photovoltaic cell," *Appl. Phys. Lett.*, vol. 48, p. 183, 1986.

[30] A. B. Djurišić, C. Y. Kwong, P. C. Chui, and W. K. Chan, "Indium–tin–oxide surface treatments: Influence on the performance of CuPc/C60 solar cells," *J. Appl. Phys.*, vol. 93, p. 5472, 2003.

[31] J. C. Bernède, Y. Berredjem, L. Cattin, and M. Morsli, "Improvement of organic solar cell

performances using a zinc oxide anode coated by an ultrathin metallic layer," *Appl. Phys. Lett.*, vol. 92, p. 083304, 2008.

[32] J. Meiss, M. K. Riede, and K. Leo, "Towards efficient tin-doped indium oxide (ITO)-free inverted organic solar cells using metal cathodes," *Appl. Phys. Lett.*, vol. 94, p. 013303, 2009.

[33] N. Li, B. E. Lassiter, R. R. Lunt, G. Wei, and S. R. Forrest, "Open circuit voltage enhancement due to reduced dark current in small molecule photovoltaic cells," *Appl. Phys. Lett.*, vol. 94, p. 023307, 2009.

[34] B. Yu, F. Zhu, H. Wang, G. Li, and D. Yan, "All-organic tunnel junctions as connecting units in tandem organic solar cell," *J. Appl. Phys.*, vol. 104, p. 114503, 2008.

[35] H. Hoppe, N. S. Sariciftci, "Organic solar cells: An overview," *J. Mater. Res*, vol. 19, p. 1924, 2004.

[36] S. Gunes, H. Neugebauer, and N. S. Sariciftci, "Conjugated polymer-based organic solar cells," *Chem. Rev.*, vol. 107, pp. 1324-1338, 2007.

[37] C. J. Brabec, A. Cravino, D. Meissner, N. S. Sariciftci, T. Fromherz, M. T. Rispens, L. Sanchez, J. C. Hummelen, "Origin of the open circuit voltage of plastic solar cells," *Adv. Funct. Mater.*, vol. 11, p. 374, 2001.

[38] M. C. Scharber, D. Mühlbacher, M. Koppe, P. Denk, C. Waldauf, A. J. Heeger, C. J. Brabec, "Design rules for donors in bulk-Heterojunction solar Cells - towards 10 % energy-conversion efficiency," *Adv. Mater.*, vol. 18, p. 789, 2006.

[39] J. Rostalski, and D. Meissner, "Monochromatic versus solar efficiencies of organic solar cells," *Sol. Energy Mater. Sol. Cells*, vol. 61, p. 87, 2000.

[40] J. Duren, X. Yang, J. Loos, C. Bulle-Lieuwma, A. B. Sieval, J. Hummelen, R. Janssen, "Relating the Morphology of Poly(p-phenylene vinylene)/Methanofullerene Blends to Solar-Cell Performance," *Adv. Funct. Mater.*, vol. 14, p. 425, 2004.

[41] H. Hoppe, M. Niggemann, C. Winder, J. Kraut, R. Hiesgen, A. Hinsch, D. Meissner, N. S. Sariciftci, "Nanoscale Morphology of Conjugated Polymer/Fullerene-Based Bulk-Heterojunction Solar Cells," *Adv. Funct. Mater.*, vol. 14, p. 1005, 2004.

[42] H. Hoppe, T. Glatzel, M. Niggemann, W. Schwinger, F. Schaeffler, A. Hinsch, M. Ch. Lux-Steiner, N.S. Sariciftci, "Efficiency limiting morphological factors of MDMO-PPV:PCBM plastic solar cells," *Thin Solid Films*, vol. 511, p. 587, 2006.

[43] J. Peet, J. Y. Kim, N. E. Coates, W. L. Ma, D. Moses, A.J. Heeger, and G. C. Bazan, "Efficiency enhancement in low-bandgap polymer solar cells by processing with alkane dithiols," *Nature Mater.*, vol. 6, pp. 497-500, 2007.

[44] A. K. Pandey, and J. M. Nunzi, "Efficiency flexible and thermally stable pentacene/C60 small molecule based organic solar cells," *Appl. Phys. Lett.*, vol. 89, p. 213506, 2006.

[45] P. Peumans, S. Uchida, and S. R. Forrest, "Efficient bulk heterojunction photovoltaic cells using small molecular-weight organic thin films," *Nature*, vol. 425, p. 158, 2003.

[46] J. Xue, S. Uchida, B. P. Rand, and S. R. Forrest, "4.2% efficient organic photovoltaic cells with low series resistances," *Appl. Phys. Lett.*, vol. 84, p. 3013, 2004.

[47] F. Yang, M. Shtein, and S. R. Forrest, "Controlled growth of a molecular bulk heterojunction photovoltaic cell," *Nature Materials*, vol. 4, pp. 37-41, 2005.

[48] N. S. Sariciftci, L. Smilowitz, A. J. Heeger, and F. Wudl, "Photoinduced electron transfer from a conducting polymer to buckminster fullerene," *Science*, vol. 258, p. 1474, 1992.

[49] S. Yoo, W. J. Potscavage, B. Domercq, J. Kim, J. Holt, and B. Kippelen, "Integrated organic photovoltaic modules with a scalable voltage output," *Appl. Phys. Lett.*, vol. 89, p. 233516, 2006.

[50] A. J. Moulé, J. B. Bonekamp, and K. Meerholz, "The effect of active layer thickness and composition on the performance of bulk-heterojunction solar cells," *J. Appl. Phys*, vol. 100, p. 094503, 2006.

[51] P. Peumans and S. R. Forrest, "Very-high-efficiency double-heterostructure copper phthalocyanine/C60 photovoltaic cells," *Appl. Phys. Lett.*, vol. 79, pp. 126-128, 2001.

[52] M. Al-Ibrahim, and O. Ambacher, "Effects of solvent and annealing on the improved performance of solar cells based on poly(3-hexylthiophene): fullerene," *Appl. Phys. Lett.*, vol. 86, p. 201120, 2005.

[53] D. Mühlbacher, M. Scharber, M. Morana, Z. Zhu, D. Waller, R. Gaudiana, C. Brabec, "High photovoltaic performance of a low-bandgap polymer," *Adv. Mater.*, vol. 18, pp. 2884-2889, 2006.

[54] P. Schilinsky, U. Asawapirom, U. Scherf, M. Biele, and C. J. Brabec, "Influence of the molecular weight of poly(3-hexylthiophene) on the performance of bulk heterojunction

solar cells," *Chem. Mater.*, vol. 17, pp. 2175-2180, 2005.

[55] D. Gebeyehu, M. Pfeiffer, B. Maennig, J. Drechsel, A. Werner, and K. Leo, "Highly efficient p–i–n type organic photovoltaic devices," *Thin Solid Films*, vol. 451-452, pp. 29-32, 2004.

[56] W. U. Huynh, J. J. Dittmer, and A. P. Alivisatos, "Hybrid nanorod-polymer solar cells," *Science*, vol. 295, pp. 2425-2427, 2002.

[57] M. Al-Ibrahim, H. K. Roth, M. Schroedner, A. Konkin, U. Zhokhavets, G. Gobsch, P. Scharff, and S. Sensfuss, "The influence of the optoelectronic properties of poly(3-alkylthiophenes) on the device parameters in flexible polymer solar cells," *Organic Electronics*, vol. 6, pp. 65-77, 2005.

[58] J. Cremer, P. Bäuerle, M. M. Wienk, and R. A. J. Jansse, "High open-circuit voltage poly(ethynylene bithienylene):pullerene solar cells," *Chem. Mater.*, vol. 18, pp. 5832-5834, 2006.

[59] L. H. Nguyen, S. Günes, H. Neugebauer, N. S. Sariciftci, F. Banishoeib, A. Henckens, T. Cleij, L. Lutsen, and D. Vanderzande, "Precursor route poly(thienylene vinylene) for organic solar cells: photophysics and photovoltaic performance," *Sol. Energy Mater. Sol. Cells*, vol. 90, pp. 2815-2828, 2006.

[60] E. Kymakis, E. Koudoumas, I. Franghiadakis, and G. A. J. Amaratunga, "Post-fabrication annealing effects in polymer-nanotube photovoltaic cells," *J. Phys. D: Appl. Phys.*, vol. 39, pp. 1059-1062, 2006.

[61] F. Wudl, "The chemical properties of buckminsterfullerene (C60) and the birth and infancy of fulleroids," *Acc. Chem. Res.*, vol. 25, pp. 157-161, 1992.

[62] S. Rait, S. Kashyap, P. K. Bhatnagar, P. C. Mathur, S. K. Sengupta, J. Kumar, "Improving power conversion efficiency in polythiophene/fullerene-based bulk heterojunction solar cells," *Sol. Energy Mater. Sol. cells*, vol. 91, pp. 757-763, 2007.

[63] Y. Ding, "Optical properties of photovoltaic polymers," Memorial University of Newfoundland, St.John's, Honours thesis 2007.

[64] J. S. Kim, R. H. Friend, and F. Cacialli, "Improved operational stability of polyfluorene-based organic light-emitting diodes with plasma-treated indium–tin–oxide anodes," *Appl. Phys. Lett.*, vol. 74, p. 3048, 1999.

[65] J. S. Kim, M. Granstrom, R. H. Friend, N. Johanson, W. R. Salaneck, F. Cacialli, "Indium–tin oxide treatments for single- and double-layer polymeric light-emitting diodes: The relation between the anode physical, chemical, and morphological properties and the device performance," *J. Appl. Phys.*, vol. 84, p. 6859, 1998.

[66] J. S. Kim, F. Cacialli, A. Cola, G. Gigli, and R. Cingolani, "Hall measurements of treated indium tin oxide surfaces," *Synth. Met.*, vol. 111, p. 363, 2000.

[67] F. Cacialli, A. Cola, G. Gigli, and R. Cingolani J. S. Kim, "Increase of charge carriers density and reduction of Hall mobilities in oxygen-plasma treated indium–tin–oxide anodes," *Appl. Phys. Lett.*, vol. 75, p. 19, 1999.

[68] J. S. Kim, R. H. Friend, and F. Cacialli, "Surface energy and polarity of treated indium–

tin–oxide anodes for polymer light-emitting diodes studied by contact-angle measurements," *J. Appl. Phys.*, vol. 86, p. 2774, 1999.

[69] C. N. Li, C. Y. Kwong, A. B. Djurišić, P. T. Lai, P. C. Chui, W. K. Chan, and S. Y. Liu, "Improved performance of OLEDs with ITO surface treatments," *Thin Solid Films*, vol. 477, p. 57, 2005.

[70] Z. You, and J. Dong, "Surface modifications of ITO electrodes for polymer light-emitting devices," *Appl. Surf. Sci.*, vol. 253, p. 2102, 2006.

[71] Z. H. Huang, X. T. Zeng, X. Y. Sun, E. T. Kang, Jerry Y. H. Fuh, and L. Lu, "Influence of plasma treatment of ITO surface on the growth and properties of hole transport layer and the device performance of OLEDs," *Organic Electronics*, vol. 9, p. 51, 2008.

[72] J. S. Yu, S. L. Lou, W. Z. Li, Y. D. Jiang and W. Li L. Li, "Surface modification and characterization of indium–tin oxide for organic light-emitting devices," *J. Mater. Sci. : Mater. in Electronics*, vol. 19, p. 1214, 2008.

[73] T. Hua, F. Zhang, Z. Xua, S. Zhao, X. Yue, and G. Yuana, "Effect of UV–ozone treatment on ITO and post-annealing on the performance of organic solar cells," *Synth. Met.*, vol. 159, pp. 754-6, 2009.

[74] F. Nüesch, E. W. Forsythe, Q. T. Le, Y. Gao, and L. J. Rothberg, "Importance of indium tin oxide surface acido basicity for charge injection into organic materials based light emitting diodes," *J. Appl. Phys.* , vol. 87, p. 7973, 2000.

[75] F. Nüesch, K. Kamarás, and L. Zuppiroli, "Protonated metal-oxide electrodes for organic

light emitting diodes," *Chem. Phys. Lett.*, vol. 283, p. 194, 1998.

[76] F. Nüesch, L. J. Rothberg, E. W. Forsythe, Q. T. Le, and Y. Gao, "A photoelectron spectroscopy study on the indium tin oxide treatment by acids and bases," *Appl. Phys. Lett.*, vol. 74, p. 880, 1999.

[77] Q. T. Le, F. Nüesch, L. J. Rothberg, E. W. Forsythe, and Y. Gao, "Photoemission study of the interface between phenyl diamine and treated indium–tin–oxide," *Appl. Phys. Lett.*, vol. 75, p. 1357, 1999.

[78] F. Li, H. Tang, J. Shinar, O. Resto, and S. Z. Weisz, "Effects of aquaregia treatment of indium–tin–oxide substrates on the behavior of double layered organic light-emitting diodes," *Appl. Phys. Lett.*, vol. 70, p. 2741, 1997.

[79] A. B. Djurišić, T. W. Lau, C. Y. Kwong, W. Guo, Y. Bai, E. H. Li, and W. K. Chan, "Surface treatments of indium tin oxide substrates: comprehensive investigation of mechanical, chemical, thermal, and plasma treatments," *Proc. SPIE*, vol. 4464, p. 273, 2002.

[80] Schroder, K. D., *Semiconductor Material and Device Characterization*. New York: John Wiley & Sons, 1998.

[81] M. Pfeiffer, A. Beyer, T. Fritz, and K. Leo, "Controlled doping of phthalocyanine layers by cosublimation with acceptor molecules: a systematic Seebeck and conductivity study," *Appl. Phys. Lett.*, vol. 73, p. 3202, 1998.

[82] K. Kishimoto, and T. Koyanagi, "Preparation of sintered degenerate n-type PbTe with a

small grain size and its thermoelectric properties," *J. Appl. Phys.*, vol. 92, p. 2544, 2002.

[83] M. O. Hakim, "Carrier compensation and activation energy studies in pyrolytic In2O3 thin film," *J. Mater. Sci.*, vol. 25, p. 1294, 1990.

[84] S. Hwang and Y. Chen, "Synthesis and electrochemical and optical properties of novel poly(aryl ether)s with isolated carbazole and p-quaterphenyl chromophores," *Macromolecules*, vol. 34, p. 2981, 2001.

[85] H. D. Kwak, D. S. Choi, Y. K. Kim, and B. C. Sohn, "Study on the work function of various ITO substrates using electrochemical analysis," *Mol. Cryst. and Liq. Cryst.*, vol. 370, pp. 47-52, 2001.

[86] M. Ishii, T. Mori, H. Fujikawa, S. Tokito, and Y. Taga, "Improvement of organic electroluminescent device performance by in situ plasma treatment of indium–tin-oxide surface," *J. Lumin.*, vol. 87-89, pp. 1165-1167, 2000.

[87] K. Sugiyama, H. Ishii, Y. Ouchi, and K Seki, "Dependence of indium–tin–oxide work function on surface cleaning method as studied by ultraviolet and x-ray photoemission spectroscopies," *J. Appl. Phys.*, vol. 87, pp. 295-298, 2000.

[88] B. J. Ryan and K. M. Poduska, "Roughness effects on contact angle measurements," *Am. J. Phys.*, vol. 76, pp. 1074-1077, 2008.

[89] Z. Y. Zhong and Y. D. Jiang, "Surface treatments of indium-tin oxide substrates for polymer electroluminescent devices," *Phys. Stat. Sol. A*, vol. 203, pp. 3882-3892, 2006.

[90] W. S. Rasband. (1997-2006) ImageJ. [Online]. http://rsb.info.nih.gov/ij.

[91] M. Brugnara. (1997-2006) Contact angle: an ImageJ plugin. [Online]. http://rsb.info.nih.gov/ij/plugins/contact-angle.html.

[92] W. H. Kim, A. J. Mäkinen, N. Nikolov, R. Shashidhar, H. Kim, and Z. H. Kafafi, "Molecular organic light-emitting diodes using highly conducting polymers as anodes," *Appl. Phys. Lett.*, vol. 80, p. 3844, 2002.

[93] M. Gross, D. C. Müller, H. Nothofer, U. Scherf, D. Neher, C. Bräuchle, and K. Meerholz, "Improving the performance of doped π-conjugated polymers for use in organic light-emitting diodes," *Nature*, vol. 405, pp. 661-665, 2008.

[94] J. A. Lim, J. H. Cho, Y. D. Park, D. H. Kim, M. Hwang, and K. Cho, "Solvent effect of inkjet printed source/drain electrodes on electrial properties pf polymer thin-film transistors," *Appl. Phys. Lett.*, vol. 88, p. 082102, 2006.

[95] T. Kawase, R. H. Friend, T. Shimoda, M. Inbasekaran, W. Wu, and E. P. Woo H. Sirringhaus, "High-resolution inkjet printing of all-polymer transistor circuits," *Science*, vol. 290, p. 2123, 2000.

[96] E. Ahlswede, W. Mühleisen, M. W. b. M. Wahi, J. Hanisch, and M. Powalla, "Highly efficient organic solar cells with printable low-cost transparent contacts," *Appl. Phys. Lett.*, vol. 92, p. 143307, 2008.

[97] T. Aernouts, P. Vanlaeke, W. Geens, J. Poortmans, P. Heremans, S. Borghs, R. Mertens, R. Andriessen, and L. Leenders, "Printable anodes for flexible organic solar cell modules," *Thin Solid Films*, vol. 451-452, pp. 22-25, 2004.

[98] L. Groenendaal, F. Jonas, D. Freitag, H. Pielartzik, and J. R. Reynolds, "Poly(3,4-ethylenedioxythiophene) and its derivatives: past, present, and future," *Adv. Mater.*, vol. 12, p. 481, 2000.

[99] K. Kawano, N. Ito, T. Nishimori, and J. Sakai, "Open circuit voltage of stacked bulk heterojunction organic solar cells," *Appl. Phys. Lett.*, vol. 88, p. 073514, 2006.

[100] K. Fehse, K. Walzer, K. Leo, W. Lövenich, and A. Elschner, "Highly conductive polymer anodes as replacements for inorganic materials in high-efficiency organic light-emitting diodes," *Adv. Mater.*, vol. 19, p. 441, 2007.

[101] Y. Zhou, F. Zhang, K. Tvingstedt, S. Barrau, F. Li, W. Tian, and O. Inganäs, "Investigation on polymer anode design for flexible polymer solar cells," *Appl. Phys. Lett.*, vol. 92, p. 233308, 2008.

[102] Y. Lim, S. Lee, D. J. Herman, M. T. Lloyd, J. E. Anthony, and G. G. Malliaras, "Spray-deposited poly(3,4-ethylenedioxythiophene):poly(styrenesulfonate) top electrode for organic solar cells," *Appl. Phys. Lett.*, vol. 93, p. 193301, 2008.

[103] M. Kim, M. Kang, L. J. Guo, and J. Kim, "Choice of electrode geometry for accurate measurement of organic photovoltaic cell performance," *Appl. Phys. Lett.*, vol. 92, p. 133301, 2008.

[104] A. Moliton, and J. Nunzi, "How to model the behaviour of organic photovoltaic cells," *Polymer Int.*, vol. 55, pp. 583-600, 2006.

[105] J. M. Nunzi, "Organic photovoltaic materials and devices," *Comptes Rendus Physique*, vol.

3, pp. 523-542, 2002.

[106] T. Aernouts, W. Geens, J. Poortmans, P. Heremans, S. Borghs, and R. Mertens, "Extraction of bulk and contact components of the series resistance in organic bulk donor-acceptor-heterojunctions," *Thin Solid Films*, vol. 403, p. 297, 2002.

[107] Z. Knittl, *Optics of Thin Films*. London: Wiley, 1976.

[108] H. A. Macleod, *Thin Film Optical Filters, 3rd edition*. London: Taylor & Francis, 2001.

[109] L. A. A. Pettersson, L. S. Roman, and O. Inganäs, "Modeling photocurrent action spectra of photovoltaic devices based on organic thin films," *J. Appl. Phys.*, vol. 86, p. 487, 1999.

[110] N. K. Persson, A. Hanns, and O. Inganäs, "Optical optimization of polyfluorene-fullerene blend photodiodes," *J. Phys. Lett.*, vol. 97, p. 034503, 2005.

[111] G. Dennler, K. Forberich, M. C. Scharber, C. J. Brabec, I. Tomiš, K. Hingerl, and T. Fromherz, "Angle dependence of external and internal quantum efficiencies in bulk-heterojunction organic solar cells," *J. Appl. Phys.*, vol. 102, p. 054516, 2007.

[112] S. Barrau, F. Zhang, A. Herland, W. Mammo, M. R. Andersson, and O. Inganäs, "Integration of amyloid nanowires in organic solar cells," *Appl. Phys. Lett.*, vol. 93, p. 023307, 2008.

[113] H. Hoppe, N.S. Sariciftci, and D. Meissner, "Optical constants of conjugated polymer/fullerene based bulk-," *Mol. Cryst. Liq. Cryst. Sci. Technol., Sect. A.*, vol. 385, p. 113, 2002.

[114] E. D. Palik, *Handbook of Optical Constants of Solids*. Orlando: Academic Press, 1997.

[115] T. Cui, K. Varahramyan M. Zhu, "Experimental and theoretical investigation of MEH-ppv based Schottky diodes," *Microelectron Eng.*, vol. 75, pp. 269-274, 2004.

[116] J. K. Lee, N. E. Coates, S. Cho, N. S. Cho, D. Moses, G. C. Bazan, K. Lee, and A. J. Heeger, "Efficacy of TiOx optical spacer in bulk-heterojunction solar cells processed with 1,8-octanedithiol," *Appl. Phys. Lett.*, vol. 92, p. 243308, 2008.

[117] J. Chena, H. Weib and K. Ho, "Using modified poly(3,4-ethylene dioxythiophene): Poly(styrene sulfonate) film as a counter electrode in dye-sensitized solar cells," *Sol. Energy Mater. Sol. cells*, vol. 22, pp. 1472-1477, 2007.

[118] J. Y. Kim, J. H. Jung. D. E. Lee, and J. Joo, "Enhancement of electrical conductivity of poly(3,4-ethylenedioxythiophene)/poly(4-styrenesulfonate) by a change of solvents," *Synth. Met.*, vol. 126, p. 311, 2002.

[119] S. Alem, R. Bettignies, J. M. Nunzi, and M.l Cariou, "Efficient polymer-based interpenetrated network photovoltaic cells," *Appl. Phys. Lett.*, vol. 84, p. 2178, 2004.

[120] A. K. Pandey, J. M. Nunzi, B. Ratier, and A. Moliton, "Size effect on organic optoelectronics devices: Example of photovoltaic cell efficiency," *Physics Letter A*, vol. 372, pp. 1333-1336, 2008.

[121] H. Chen, M. K. F. Lo, G. Yang, H. G. Monbouquette, and Y. Yang, "Nanoparticle-assisted high photoconductive gain in composites of polymer and fullerene," *Nature nanotechnology*, vol. 3, p. 543, 2008.

[122] R. Jackson, B. Domercq, R. Jain, B. Kippelen, and S. Graham, "Stability of doped

transparent carbon nanotube electrodes," *Adv. Funct. Mater.*, vol. 18, p. 2548, 2008.

[123] S. M. Sze, and K. K. Ng, *Physics of Semiconductor Devices*. USA: Wiley-Interscienc, 1981.

[124] V. D. Mihailetchi, P. W. M. Blom, J. C. Hummelen, and M. T. Rispens, "Cathode dependence of the open-circuit voltage of polymer:fullerene bulk heterojunction solar cells," *J. Appl. Phys.*, vol. 94, p. 6849, 2003.

[125] M. Ishii, T. Mori, H. Fujikawa, S. Tokito, and Y. Taga, "Improvement of organic electroluminescent device performance by in situ plasma treatment of indium–tin-oxide surface," *J. Luminescene*, vol. 87-89, pp. 1165-67, 2000.

[126] M Izaki, and T Omi, "Transparent zinc oxide films prepared by electrochemical reaction," *Appl. Phys. Lett.*, vol. 68, p. 2439, 1996.

[127] V. Bhosle, J. T. Prater, F. Yang, D. Burk, S. R. Forrest, and J. Narayan, "Gallium-doped zinc oxide films as transparent electrodes for organic solar cell applications," *J. Appl. Phys.*, vol. 102, p. 023501, 2007.

[128] J. Gilot, I. Barbu, M. M. Wienk, and R. A. J. Janssen, "The use of ZnO as optical spacer in polymer solar cells: theoretical and experimental study," *Appl. Phys. Lett.*, vol. 91, p. 113520, 2007.

[129] M. S. White, D. C. Olson, S. E. Shaheen, N. Kopidakis, and D. S. Ginley, "Inverted bulk-heterojunction organic photovoltaic device using a solution-derived ZnO underlayer," *Appl. Phys. Lett.*, vol. 89, p. 143517, 2006.

[130] W. J. E. Beek, M. M. Wienk, R. A. J. Janssen, "Hybrid solar cells from regioregular polythiophene and ZnO nanoparticles," *Adv. Funct. Mater.*, vol. 16, pp. 1112-1116, 2006.

[131] W. J. E. Beek, M. M. Wienk, R. A. J. Janssen, "Efficient hybrid solar cells from zinc oxide nanoparticles and a conjugated polymer," *Adv. Mater.*, vol. 16, p. 1009, 2004.